Charge-Transfer Surface-Enhanced Raman Spectroscopy in Semiconductor Nanoparticles: Material ZnO

Bachelorarbeit 2

Zur Erlangung des akademischen Grades
„Bachelor of Science in Engineering“

Studiengang:
“Umwelt- Verfahrens- und Biotechnik”
Management Center Innsbruck

Begutachtender:
Mag. Alexander Dumfort

Verfasser:
Ing. Alexander Richter
0610351036

Datum: 29.05.2009

Sperrung der Bachelorarbeit

Ich habe die Sperrung meiner Bachelorarbeit beantragt, welche von der Studiengangsleitung genehmigt wurde.

Ort, Tag / Monat / Jahr _____

Eidesstattliche Erklärung

Ich erkläre hiermit an Eides statt, dass ich die vorliegende Bachelorarbeit selbständig angefertigt habe. Die aus fremden Quellen direkt oder indirekt übernommenen Gedanken sind als solche kenntlich gemacht.

Die Arbeit wurde bisher weder in gleicher noch in ähnlicher Form einer anderen Prüfungsbehörde vorgelegt und auch noch nicht veröffentlicht.

Ort, Tag / Monat / Jahr _____

With gratitude to my family, friends, and colleagues, who have made my life a joyful adventure.
To the memories of Florian Taxacher, Luz de los Angeles Gorme,
and Margarethe Kostenbaumer Richter.

Contents

Abstract

Surface-Enhanced Raman Spectroscopy belongs to the field of vibrational spectroscopy. With SERS it is possible to obtain fingerprint spectra of complex organic molecules at low concentration. Even single molecule detections have been successfully observed with SERS. For applications such as biosensors and investigations in forensic science, it is of utmost importance to develop new SERS materials that give strong spectra of organic molecules. To compare different samples with one another, the degree of charge transfer ($p_{CT}(\nu_i)$) in the obtained spectra was calculated.(1) An excitation-wavelength dependence study in the sample assemblies Ag/PATP, Ag/PATP/ZnO, and ZnO/PATP/Ag, and a size-dependence study of ZnO in Ag/PATP/ZnO on SERS signals of the organic molecule PATP are presented in this work. Since most sophisticated SERS spectra are generally obtained at resonance, the excitation-wavelength dependence study focused on finding a resonance in Ag/PATP, Ag/PATP/ZnO, and ZnO/PATP/Ag. It was found that the resonance of Ag/PATP occurs at a different excitation wavelength compared to the resonance of Ag/PATP/ZnO or ZnO/PATP/Ag. In addition, it was observed that Ag/PATP/ZnO as well as ZnO/PATP/Ag give better $p_{CT}(\nu_i)$ values and peak enhancements compared to the assembly Ag/PATP alone. The size-dependence study of ZnO focused on finding resonance by varying the ZnO nanoparticle size from 18.2 nm to 33.1 nm in the sample Ag/PATP/ZnO. It was found that resonance of $p_{CT}(\nu_i)$ occurs at a ZnO diameter of 27.7 nm in the observed diameter range. Furthermore, both studies provide novel information for understanding semiconductors in SERS.

Advisor at the City College of New York / USA: **Professor J. Lombardi**

Advisor at Management Center Innsbruck / Austria: **Mag. A. Dumfort**

Summary

This project focuses on the investigation of ZnO nanoparticles in SERS. Specifically, sandwich structures consisting of Ag nanoparticles/PATP (organic molecule)/ZnO nanoparticles will be investigated. SERS, a kind of vibrational spectroscopy, has already proved its potential as an accurate analyzing tool in the fields of forensic science, artwork analysis, and physical chemistry through its ability to detect minute concentrations of organic molecules or single molecules adsorbed on metal surfaces. The use of metal/organic molecule/semiconductor sandwich structures (Ag/PATP/ZnO) for organic molecule detection has potential for giving better fingerprint SERS spectra than metal/organic molecule complexes only. It was recently found that ZnO nanorods in the thin-film structures Ag/PATP/ZnO and ZnO/PATP/Ag alter the SERS spectrum significantly compared to the SERS spectrum obtained at Ag/PATP.(2) In addition, recent publications on ZnO indicate that the enhancements of the vibrational modes of organic molecules adsorbed on ZnO nanoparticles in SERS are ZnO size dependent. The SERS spectra of 4-MPy adsorbed on ZnO nanoparticles showed a measured resonance in the region of 27.7 nm.(3) In this work, experiments on the sample assemblies Ag/PATP, Ag/PATP/ZnO, and ZnO/PATP/Ag were conducted. For comparison of the different samples and spectra the degrees of charge transfer ($p_{CT}(\nu_i)$) were calculated. The samples were investigated by SERS. With an excitation wavelength that varied between 475.6 nm and 676.4 nm, different excitation-dependent $p_{CT}(\nu_i)$ values were obtained in each sample of Ag/PATP, Ag/PATP/ZnO, and ZnO/PATP/Ag. In addition, it was found that the excitation-dependent resonance for each sample occurred at a different excitation wavelength. With a size-dependence study with ZnO nanoparticle sizes from 18.2 nm to 33.1 nm, it was possible to scan through a resonance of the sample structures Ag/PATP/ZnO. ZnO nanoparticle that were 27.7 nm gave the highest $p_{CT}(\nu_i)$ values compared to the other investigated sizes. For analyzing organic molecules with SERS, the highest possible enhancements of peaks in SERS spectra are preferred. With the combination of wavelength-dependent resonance and size-dependent resonance of ZnO, the highest enhancement factors in SERS spectra can be obtained. Chapter 1 gives an overview of the project; Chapter 2 provides theoretical background information important for analyzing SERS spectra, and Chapter 3 gives an overview of research conducted on ZnO pertaining to SERS. This last chapter includes research on p-aminothiophenol (PATP), ZnO nanoparticles in SERS, and ZnO in the sandwich structure Ag/PATP/ZnO. Current research on calculations of the degree of charge transfer is explained in this chapter as well. The experiments conducted are summarized in Chapter 4. Results of the two main studies, the excitation-wavelength dependence study and the ZnO nanoparticle size-dependence study, are presented. The experimental section is followed by discussions and comparisons of the obtained results to those in published research work.

The findings of this bachelor research will be of utmost interest to those fields in which SERS is applied as an analyzing tool, as well as for physical chemistry research, since they provide new results on charge-transfer calculation of ZnO nanoparticles employed in SERS.

1. Introduction

ZnO is a semiconductor with several favorable properties including good transparency, conductivity, a large band gap, and strong room-temperature luminescence. In addition, synthesis and size control of ZnO nanoparticles are easily achievable. As a result of its properties, ZnO is already used in high-tech applications such as transparent electrodes in liquid crystal displays and thin-film transistors.(4) Since nanotechnology is a key field of the future and ZnO has superior useful properties, ZnO nanoparticles are worthy of focus and research. Future applications could include, for example, very sophisticated biosensors for the detection of organic molecules in low concentration using SERS.

1.1. Purpose

My thesis objective is to investigate the effect of ZnO nanoparticles on the degree of charge transfer ($p_{CT}(\nu_i)$) in SERS spectra. Current research work on SERS focuses on understanding the inherent mechanism responsible for SERS spectra, and on finding novel SERS materials capable of providing better SERS spectra of organic molecules. Semiconductors in SERS have gained interest in recent years(2)(3) and demand further research on their effect on SERS spectra. The purpose of this project is to investigate the effect of ZnO nanoparticles on the degree of charge transfer ($p_{CT}(\nu_i)$) in SERS spectra.

Research was conducted in an excitation-wavelength dependence study and a size-dependence study. In detail, $p_{CT}(\nu_i)$ values of the sample structures Ag/PATP without ZnO nanoparticles, Ag/PATP/ZnO, and ZnO/PATP/Ag, all at excitation wavelengths from 476.5 nm to 676.4 nm, are compared with one another, and the ZnO nanoparticle size-dependent $p_{CT}(\nu_i)$ values in the samples Ag/PATP/ZnO (18.2 to 33.1 nm) are investigated.

1.2. Investigated Material

The effect of ZnO nanoparticles on SERS spectra was investigated in three different sample structures: Ag/PATP, Ag/PATP/ZnO, and ZnO/PATP/Ag, as depicted in Figure 1.

- Ag nanoparticles are known as SERS active material and provide, beside Au and Cu the highest enhancement factors compared to normal Raman.
- P-aminothiolphenol (PATP) with the chemical sum formula C_6H_7NS, a well-known aromatic molecule with two different active groups, one relative positive charged amino group ($–NH_2$) and a relative electronegative charged thiol group (–SH) at para position.
- ZnO is a semiconductor with a direct band gap of 3.35 eV.

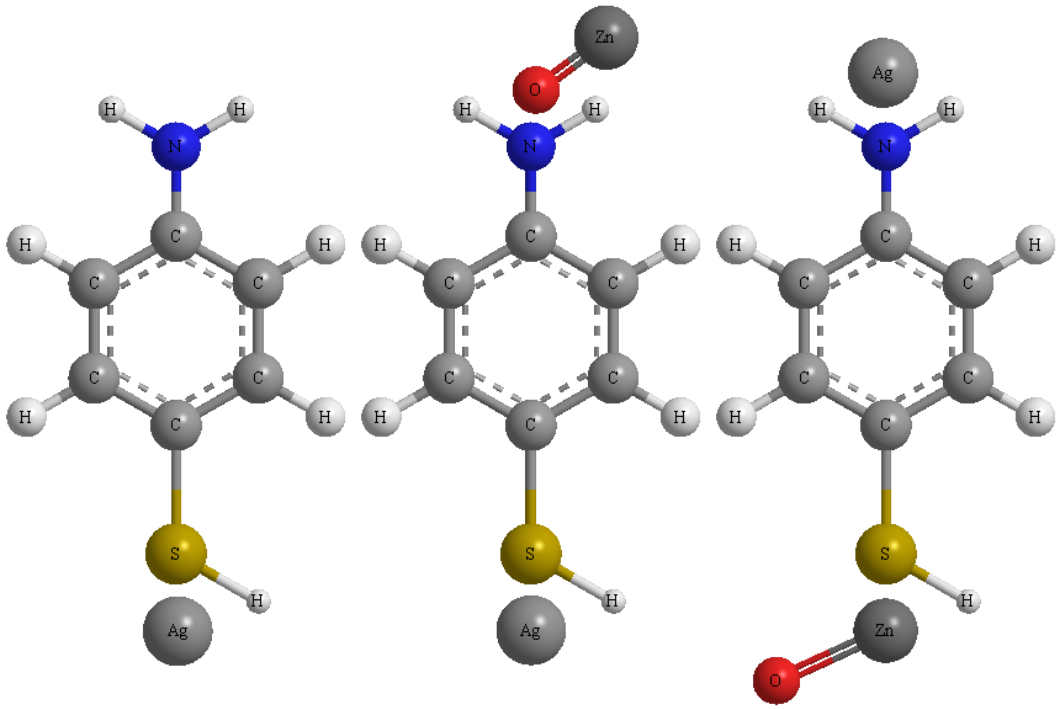

Figure 1: Sample structures from left to right Ag/PATP, Ag/PATP/ZnO and ZnO/PATP/Ag

Depending on the sample preparation procedure, the thiol group of PATP can either adsorb on the Ag nanoparticle surface as shown in the Ag-PATP and Ag-PATP-ZnO assemblies, or on the ZnO surface as in the ZnO-PATP-Ag assembly. The covalent bond of the thiol group to the surface of Ag or ZnO nanoparticles is strong compared to the bond of the amino group to a surface. In addition, the thiol group acts as a very strong H^+ donor. Although the amino group is an H^+ acceptor, it is not considered as active as the thiol group. Therefore, PATP connects with the thiol group on the surface of the first material that it comes in contact with. If PATP is adsorbed with the thiol group on the ZnO nanoparticle surface, sulfur forms a covalent bound with Zn^{2+}, and if PATP is adsorbed with the amino group on the ZnO nanoparticle surface, nitrogen forms a covalent bound with O^{2-} in the ZnO lattice. The obtained SERS spectra show the enhanced lines of PATP. Therefore, general SERS spectra patterns stay the same for all three samples depicted in Figure 1. However, different $p_{CT}(\nu_i)$ values can be obtained from the three sample assemblies Ag/PATP, Ag/PATP/ZnO, and ZnO/PATP/Ag. These $p_{CT}(\nu_i)$ values are investigated in this work. Since the samples are prepared by mixing two premixed components with a third, the sequences Ag/PATP/Ag and ZnO/PATP/ZnO are the result of distribution as well. However, it is assumed that the sample sequences Ag/PATP, Ag/PATP/ZnO, and ZnO/PATP/Ag rule the structure at each sample respectively.

2. Theory

2.1. Molecular Symmetry / Molecular Vibrations

In general, molecules with similar or the same molecular symmetry behave very much alike. The vibrational modes of the aromatic ring molecule benzene (C_6H_6) is well known and belongs to the D_{6h} point group. (5 S. 206) A point group summarizes standardized symmetry operators such as rotation axes and mirror planes. Molecules that belong to the same point group, or that have similar symmetry patterns, behave similarly with respect to molecular vibrations. The aromatic ring molecule PATP, which is the analyte in this bachelor thesis, has symmetry patterns similar to those of benzene (C_6H_6). Its thiol (–SH) and amino (NH_2) groups lower the point-group symmetry to C_{2v}, which is lower than that of the benzene molecule. However, since the main vibrational modes of the PATP molecule that can be observed in Raman spectroscopy or SERS resemble the vibrational modes of the benzene molecule, references to symmetry and vibrational modes in this chapter will be assigned to the benzene molecule.

Molecular vibrations are oscillations of atoms in the molecule. The number of vibrational modes in a molecule is directly linked to the amount of atoms in a molecule. Diatomic atoms have only one possible oscillation and therefore one vibrational mode. The PATP molecule has 39 vibrational modes (3*N-6 with N as the number of atoms). These vibrational modes can be assigned as either symmetric oscillations or asymmetric oscillations of the molecule. For investigation of the PATP molecule with SERS, the most important symmetric vibrational modes are assigned as a_1 modes (totally symmetric modes) and the most important asymmetric vibrational modes (non-totally symmetrical modes) are assigned as b_2 modes. Figure 2 shows a simplification of the vibrational modes of three atomic molecules each of H_2O (C_{2v} point group) and CO_2 that are assigned as symmetrical stretch, bending or deformation, and asymmetric stretch. The arrows in the images indicate the movements of the atoms. Since the atoms are oscillating, all atoms make the same movements in opposite direction as well. In general, at the symmetric stretch, all atoms come together at the same time. Then they turn direction and move away from each other at the same time. At the asymmetric stretch, two atoms come together at the same time while the third one moves away. Then the two others that are close to each other move apart while the one that was away comes closer to the atom in the middle. (6)

A simplified explanation of totally symmetric vibrations is as follows: All symmetry operators that are assigned to an arbitrary point group are tested. After rotating or mirroring the molecule according to the symmetry operator, at totally symmetric vibrational modes, each atom of the obtained molecule has the same oscillating direction (direction of the arrow) as the atom that was occupying the position before. Different from totally symmetric modes are the non-totally symmetric vibrational modes. After rotating or mirroring the molecule according to the symmetry operator, not every atom of the obtained molecule has the same oscillating direction (direction of the arrow) as the atom that was occupying the position before.

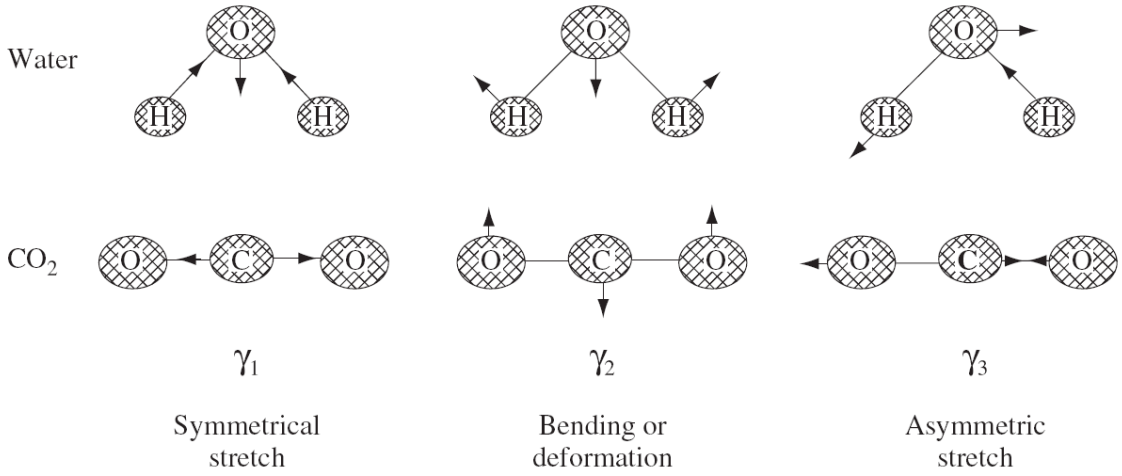

Figure 2: Spring and ball model: three modes of vibration for H_20 and CO_2 (6 p. 8)

The displacement diagram for the benzene molecule in Figure 3 shows a symmetric vibrational mode. The arrows in the benzene molecule in (a) indicate the simultaneous movement of the depicted atoms. In the depicted sample, all C-atoms of the benzene molecule expand or contract the aromatic ring simultaneously. The amplitudes of the oscillations of the atoms are depicted in (b). During the oscillations of the C-atoms, the H-atoms do not change their distance from the C-atoms.

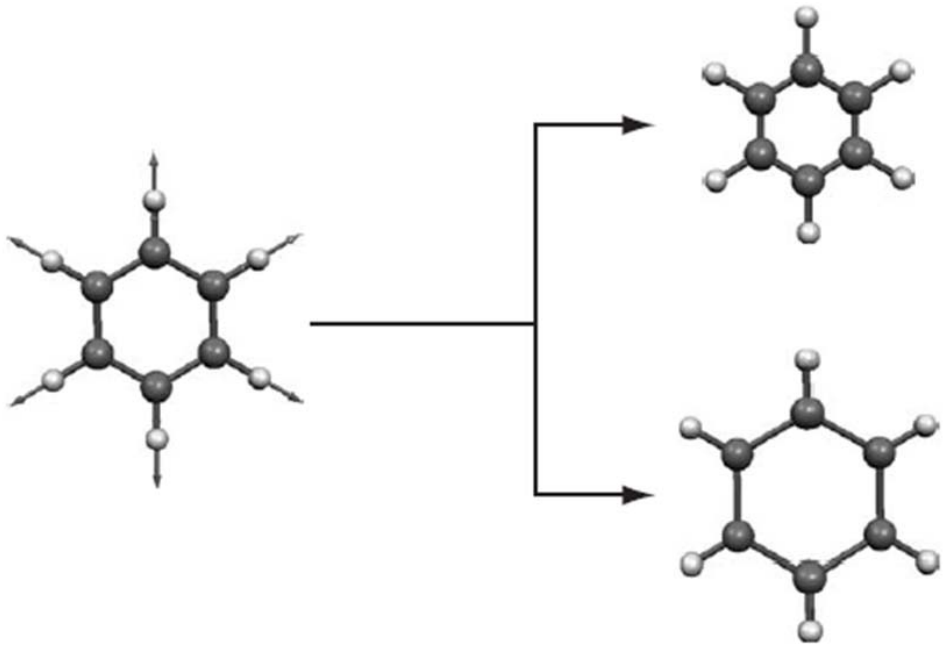

a) b)

Figure 3: Selected symmetric displacement diagram 1 for benzene (6 p. 12)

The displacement diagram for the benzene molecule in Figure 4 shows a different symmetric vibrational mode than the one depicted in Figure 3. The arrows in the benzene

molecule in (a) indicate the simultaneous movement of the H-atoms. The amplitudes of the oscillations of the atoms are depicted in (b). During the oscillations of the H-atoms, the distances of the C-atoms in the ring do not change.

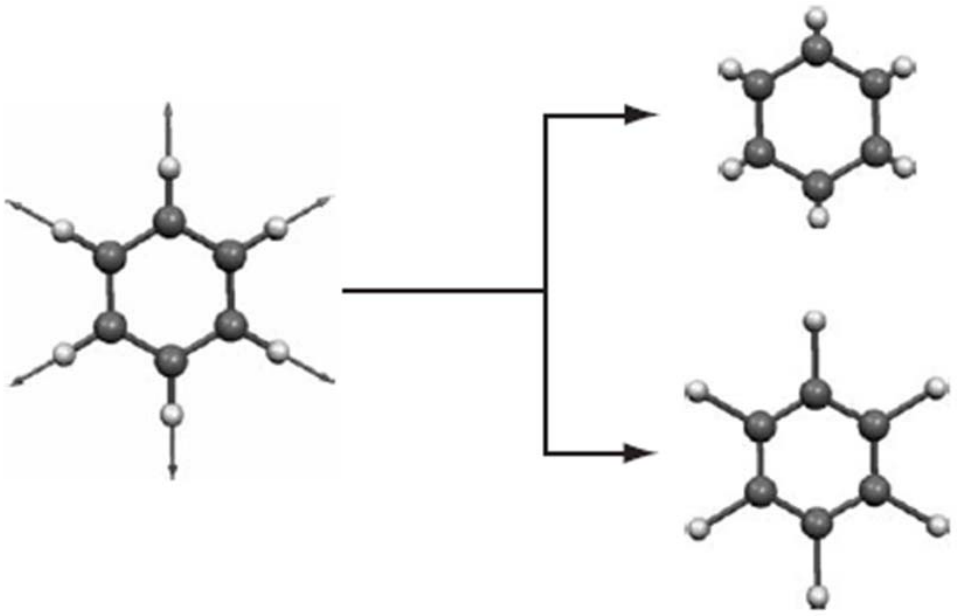

a) b)

Figure 4: Selected symmetric displacement diagram 2 for benzene(5 p. 12)

Asymmetric vibrational modes of the benzene molecule are for instance vibrational modes in which one H- or C-atom behaves differently from the other five atoms of its type in the molecule.

Summary:

- The number of vibrational modes in a molecule is dependent on the number of atoms;
- the symmetry of the PATP molecule is lower than the symmetry of the benzene molecule;
- the main vibrational modes of PATP resemble the main vibrational modes of benzene;
- a_1 modes in the PATP molecule are totally symmetric vibrational modes;
- b_2 modes in the PATP molecule are non-totally symmetric vibrational modes.

2.2. Optics

2.2.1. Spectrum of Light

The electromagnetic (EM) spectrum ranges from radio waves to gamma rays, as depicted in Figure 5. The energy of electromagnetic waves is directly coupled with its frequency and therefore with its wavelength (see Equation 3). The shorter the wavelength of an EM wave, the more intense the wave's energy. The spectrum shows the frequencies in Hz (1/s) on top, the labeling of the electromagnetic waves in the middle, and the wavelength in meters at the bottom. The visible light ranges from 400 nm in the violet-blue region to 700 nm in the red region(7), which covers only a small fraction of the EM spectrum. Electromagnetic waves with wavelengths below 400 nm belong to the ultraviolet spectrum, and EM waves with wavelengths greater than 700 nm belong to the infrared spectrum.

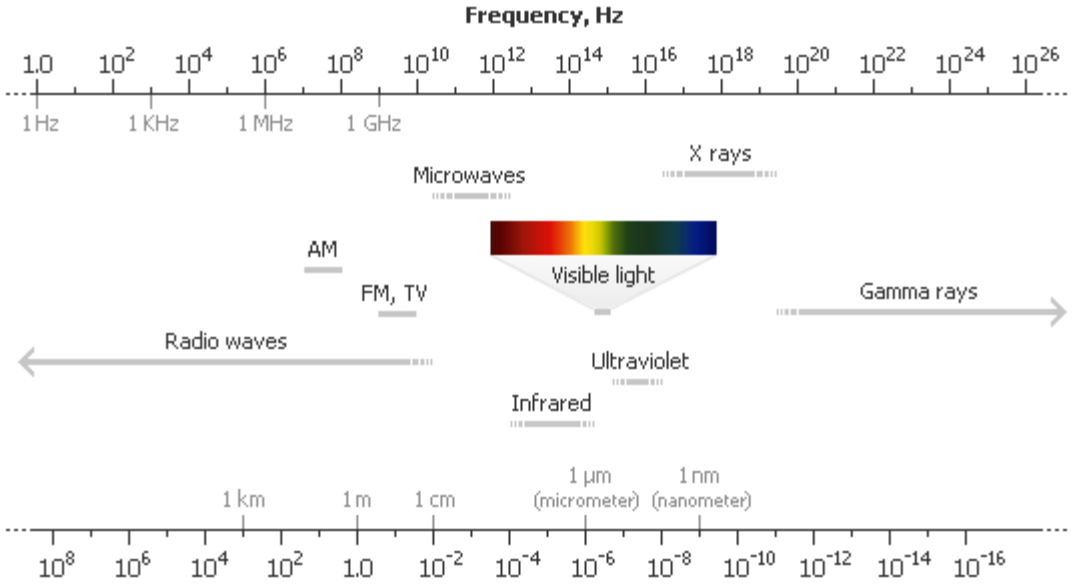

Figure 5: Electromagnetic spectrum(7)

Raman spectroscopy and SERS use excitation wavelengths that are usually in the visible spectrum of light. The scattered light that is collected at a detector can have no wavelength shift, wavelength shifts into the blue (shorter wavelengths than the incident light beam), or wavelength shifts into the red (longer wavelengths than the incident light beam). Wavelength shifts into the ultraviolet region or the infrared region are possible as well. The SERS investigations in this work deal only with wavelength shifts into the red.

2.2.2. Wave-Particle Duality of Electromagnetic Waves

Light shows properties that resemble the behavior of waves and particles. Therefore, two theories are used to describe light. Depending on the circumstances, light is described as either EM wave or photon.

- The wavelike character of light describes the phenomena of interference and diffraction of light (see Figure 6).

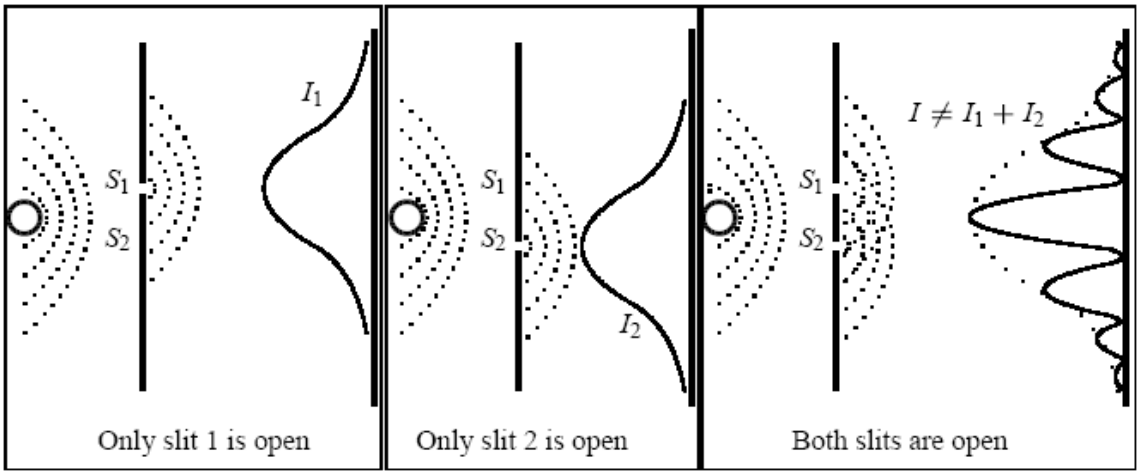

Figure 6: Slit experiments with electromagnetic waves showing the wave like character of light (8 p. 23)

The slit experiments depicted in Figure 6 describe the wavelike character of electromagnetic waves. The values I1 and I2 are the intensities recorded at a screen with one open slit. If both slits are opened, the recorded pattern on the screen resembles the interference patterns of waves, comparable to those of water waves. Therefore, $I \neq I1 + I2$, since at interference of waves the amplitudes must add and not the intensities. The total amplitude $\psi = \psi1 + \psi2$; hence the total intensity is:

Equation 1

$$I = |\psi1 + \psi2|\text{^}2$$

Note: The same slit experiment with particles would give $I = I1 + I2$. Therefore, only the wave theory of light can describe the resulting pattern on the screen. (8 p. 23)

- The particle-like character of light describes the interaction of light with matter. Photons, which are elementary particles of light, have energy and momentum. The photoelectric effect, which was discovered by Heinrich Hertz in 1887, is a prominent example of photons interacting with electrons of matter.

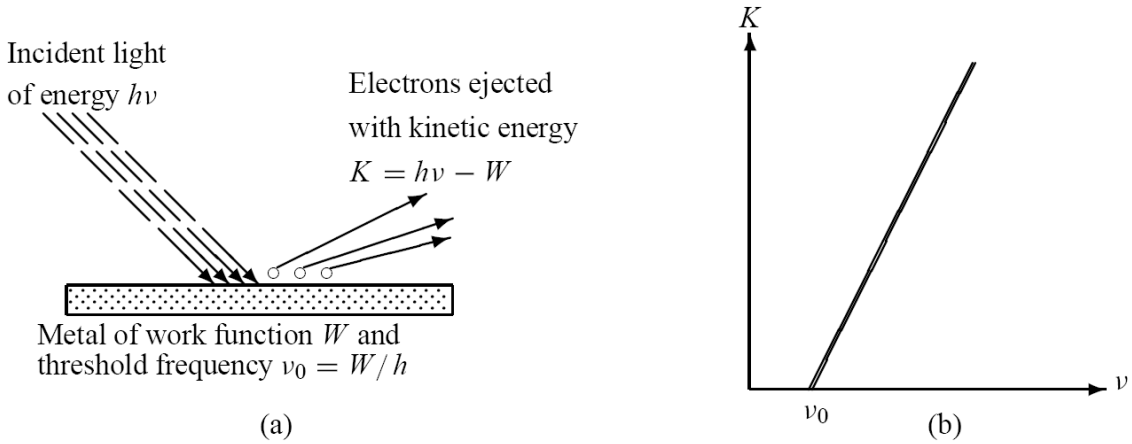

Figure 7: Photoelectric effect describing the particle-like character of light (8 p. 11)

Figure 7a depicts the interaction of incident light at a given energy $h * \nu$ with electrons of a metal. Electrons get emitted if the frequency of the incident radiation is bigger than the metal threshold frequency. The threshold frequency ν_0 is dependent on the properties of the metal. The workfunction W indicates the minimum energy needed to move an electron out of the solid to the surface of a material. *W* in electron volts and the threshold frequency ν_0 are coupled with the Planck constant *h*. Electrons get ejected with the kinetic energy $K = h * \nu - W = h * (\nu - \nu 0)$. Figure 7b shows the kinetic energy *K* of the electron leaving the metal as a function of frequency of the incident light ν. The graph shows the threshold frequency ν_0 on the x-axis.

Note: According to the description of light in the wave theory, incident light with frequencies below the threshold frequency ν_0 can excite electrons from the metal to its surface as well, since the needed energy can be reached through enhancement of intensity. However, experiments show that if the incident light frequency is below ν_0, no electrons are emitted, regardless of the applied intensity. Therefore, the photoelectric effect is described with the interaction of quantisized light particles (photons) with electrons. (8 p. 11)

According to Max Planck, the energy *E* of a photon is proportional to the frequency ν, which is coupled with Planck's constant, h.

Equation 2

$$E = h * \nu$$

The wave-particle character of light is coupled with the following equation:

Equation 3

$$\lambda = \frac{h}{p} = h * c \div E$$

Equation 4 (in vacuum)

$$\lambda = \frac{c}{\nu}$$

The wavelength λ is the Planck constant h divided by the momentum of the photon.
The wavelength λ is the velocity of the electromagnetic wave c divided by its frequency. (9 p. 3)

2.2.3. Polarization of Light

Electromagnetic waves have an electric and a magnetic field that propagate in the same direction with the same speed and frequency ν. These fields are perpendicular to each other. Furthermore, the amplitudes of the electric and magnetic fields are related by $E = c \times B$.

Figure 8 shows a plane electromagnetic wave. *E* and *B* are the amplitudes of the electric and magnetic fields respectively. The vector k_0 indicates the direction of propagation.

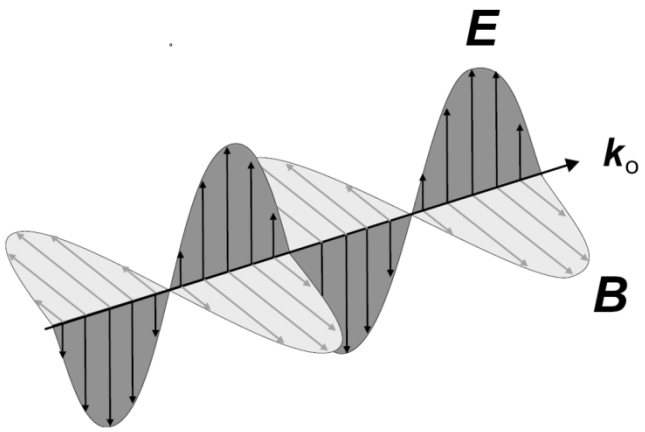

Figure 8: Electromagnetic wave (10 p. 145)

The alignment of the electric fields of light is referred to as polarization of light. Since scattering of light may change the polarization of light, it is important to control the polarization of an incident beam in spectroscopy to conclude at the analyzer on the polarization shift of the light. In Raman spectroscopy only non-totally symmetric vibrations of a molecule induce a polarization shift of the incident excitation beam, while totally symmetric vibrations do not change the polarization.

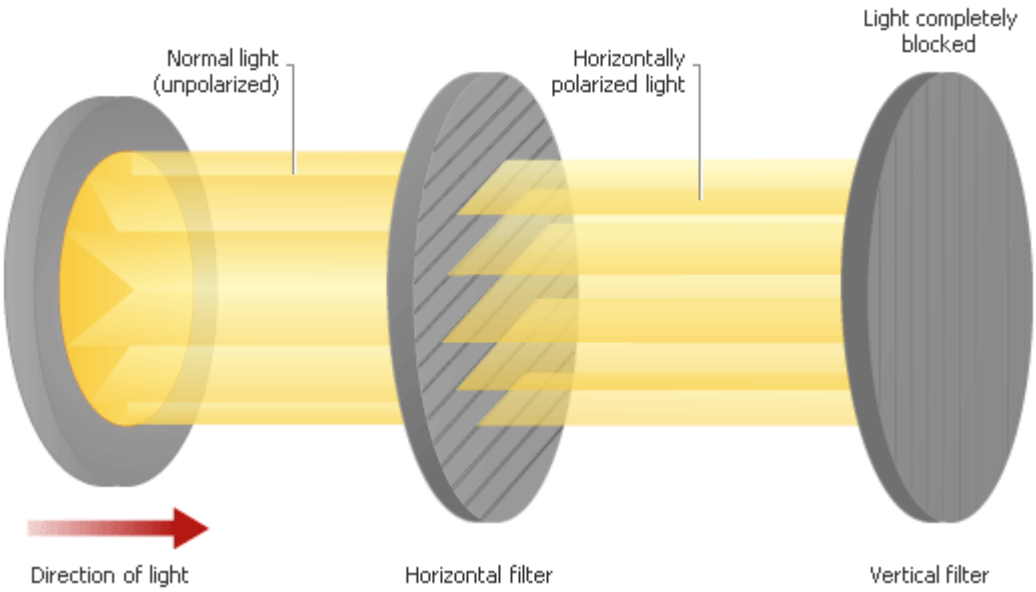

Figure 9: Polarization of light(11)

As depicted in Figure 9, normal light is unpolarized. Therefore, the planes of the electric field cover all angles between the horizontal and vertical axes. The intensity of the electromagnetic field in the absorption axis of the filter is completely absorbed. A horizontal filter is used to block out all vertically aligned electric fields. Only horizontal polarized light is allowed to pass. A vertical filter allows only vertical polarized light to pass. To measure the polarization change of the incident light induced by a sample, an additional photon detector is placed after the vertical filter, while the sample is placed between the horizontal and vertical filters.(12 p. 658)

2.2.4. Scattering of Light

Since the EM waves interact with the charged particles of molecules in a solid, liquid or gas, scattering of light occurs. Nearly all objects scatter light. In nature, alpine glow and sunsets are impressive examples. The scattering of light is proportional to the frequency of the incident EM wave to the power of four.

Electrons and protons influenced by an electric field form dipoles. Since the molecules need energy to form dipoles, photons are absorbed. An induced dipole is prone to oscillate with the frequency of the electric field of the excitation light and therefore starts oscillating. (13 S. 2) In addition, the induced dipole molecule interacts with neighboring molecules. Therefore, the polarization of matter is not only dependent on the light source. Since a dipole emits light at its oscillating frequency, scattering of light in all direction occurs. In general, the frequency of the scattered light has a wavelength different from the excitation EM wave. The fact that every material scatters light differently is used in spectroscopy.

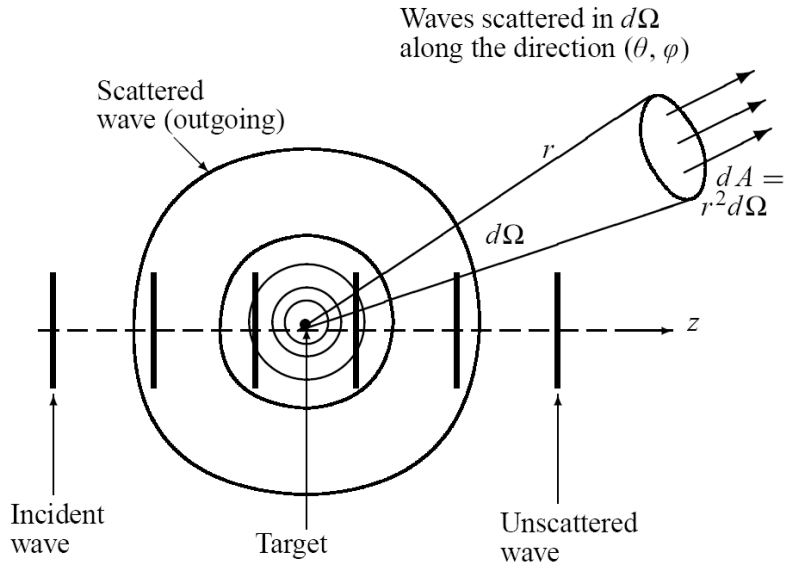

Figure 10: Light scattering (8 p. 623)

The scattering of light is illustrated in Figure 10. It shows an incident EM wave that hits a target sample. At the target sample, scattering of light occurs and propagates in all directions. Since the scattered light propagates in all directions, the intensity of it is dependent on the distance to the observer. However not all of the incident light scatters. Depending on the sample, most of the incident light can leave the sample unscattered and therefore propagate in z-direction only.

Summary:

- The scattering of light is proportional to the frequency of the incident EM wave to the fourth power;
- scattering of light is dependent on the material;
- the effect of scattering of light is used in spectroscopy.

2.3. Laser Technology

"Laser" is an acronym for **l**ight **a**mplification by the **s**timulated **e**mission of **r**adiation. Lasers offer a narrow frequency distribution of light with amplified intensity and a highly directional beam. High-accuracy lasers are employed in the medical sector, for example, for several kinds of surgery, and in research, mainly in the field of materials science.

A laser consists of three basic elements: the pump for energy supply, the laser medium for controlled emission of light, and the resonator for amplification of the laser beam. To generate stimulated emission with a specific wavelength, population inversion between two energy levels of a laser medium is needed. Since the wavelength of the output beam is dependent on the laser medium used, lasers are often named after it, for example a "helium-neon" or "argon-ion" laser. Figure 11 shows a schematic laser. An external pump serves as the energy source exciting the laser medium. The mirrors within the laser send the emitted laser light of the laser medium back and forth for amplification before the laser leaves the resonator at the partially transmitting mirror.

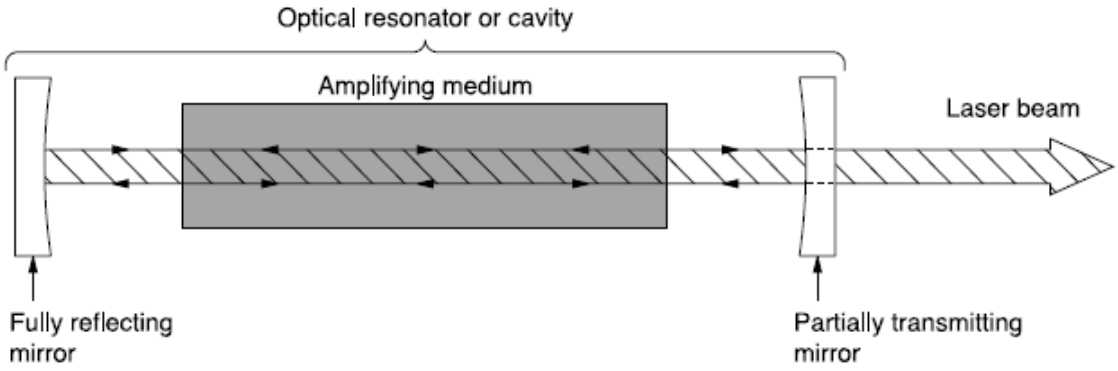

Figure 11: Main components of lasers (14 p. 2)

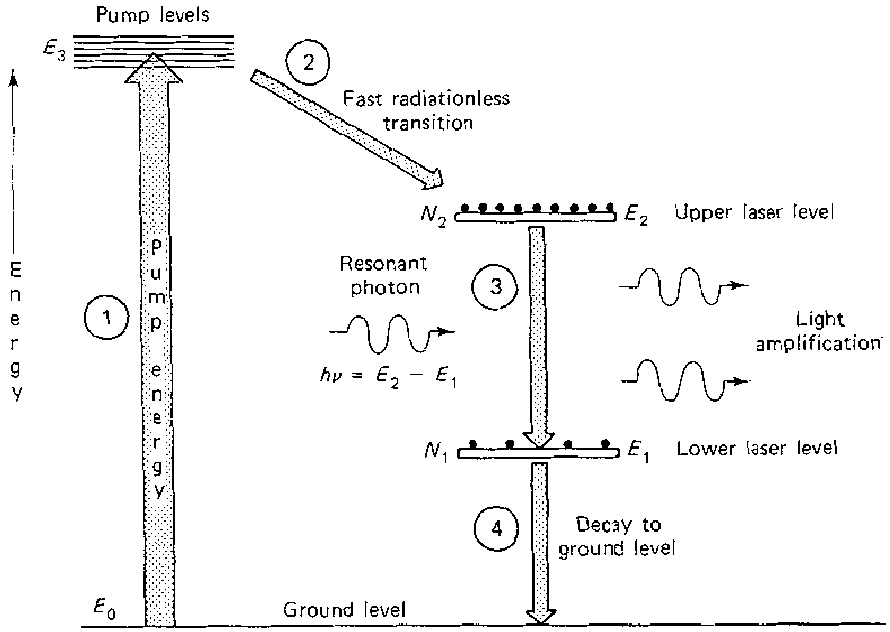

Figure 12: General four-level laser (9 p. 435)

Population inversion is accomplished if more electrons are in the excited state than in the relaxed state of a molecule. Figure 12 shows a four-level laser schematically. In the first step, electrons are excited from the ground state by an external pump. This step is followed by a fast, radiationless transition to the level E2, which is the upper laser level enhancing the amount of electrons N2. Population inversion between the states E2 and E1 is reached if N2 is greater than N1. Electrons from E2 relax down to the lower laser level E1. Photons matching the energy-level difference between E2 and E1 are emitted and amplified. As a result, the laser produces monochromatic light that can be used either coherent or pulsed. Finally, in the fourth step the electrons decay back to the ground state and close the cycle.

2.4. Spectroscopy

2.4.1. Principle of Spectroscopy

Spectroscopy is the study of phenomena in which electromagnetic waves interact with matter. Different material properties of samples result in different spectra with intensities on the y-axis versus wavelengths on the x-axis. The unique spectra can be used to identify materials, discern physical attributes, or analyze for instance molecular vibrational modes. In addition, particles like electrons behave as waves under certain conditions, and therefore such particles are employed in spectroscopy as well.(15)

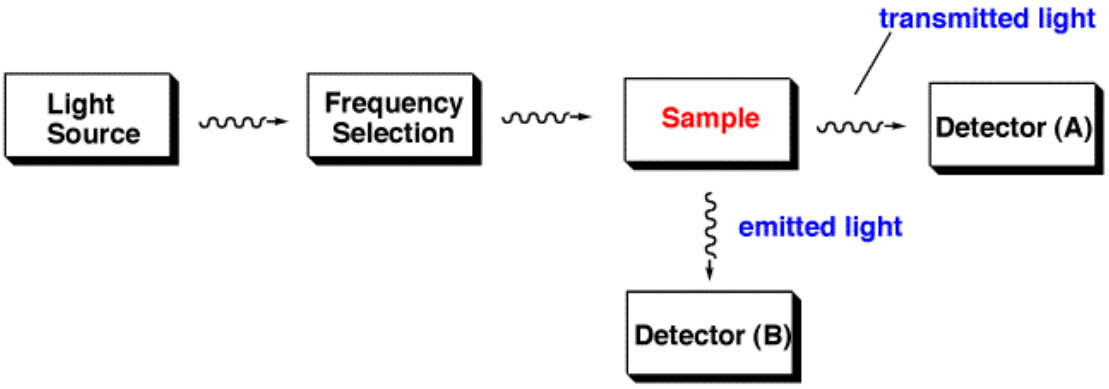

Figure 13: Block diagram of a spectrometer(15)

A spectrometer consists of an excitation source, a wavelength selector, a sample, and a detector. Figure 13 shows the basic block diagram of a spectrometer. Frequency selection is accomplished by a frequency-selective filter. Transmitted light is detected in the line of the incident beam, resulting in transmission and absorption spectra. Emitted light from the sample is detected perpendicular to the incident beam, resulting in fluorescence spectra. At detector (B) only emitted light from the sample but no transmitted light through the sample is recorded.

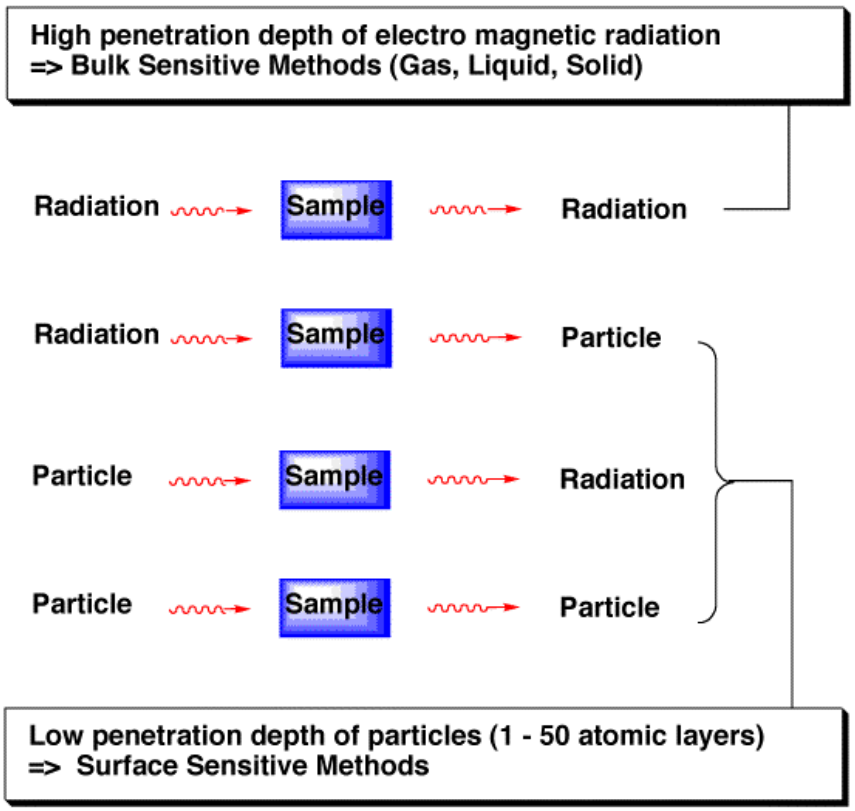

Figure 14: Different principles of spectroscopy(15)

Figure 14 shows different incident sources that are applied on a sample. Through interaction of the incident radiation or a particle beam with the sample, the output beam is altered. For instance, if incident radiation with a definite frequency and intensity is applied to a sample and interacts with the material, radiation will be reflected and absorbed by the sample and emitted from the sample. As a result, the output beams have different properties such as different frequencies and intensities. The output beams are recorded in a proper detector. Next, a spectrum is generated from which it is possible to determine an unknown sample through comparison to a reference probe, or to draw conclusions about sample properties of a known specimen.

2.4.2. Interaction of Photons with Molecules

Electromagnetic radiation provides energy that can be absorbed and emitted by a sample. The energy bits of light are called photons. Photons with different energy have various effects on atoms and molecules which will be described in this chapter.

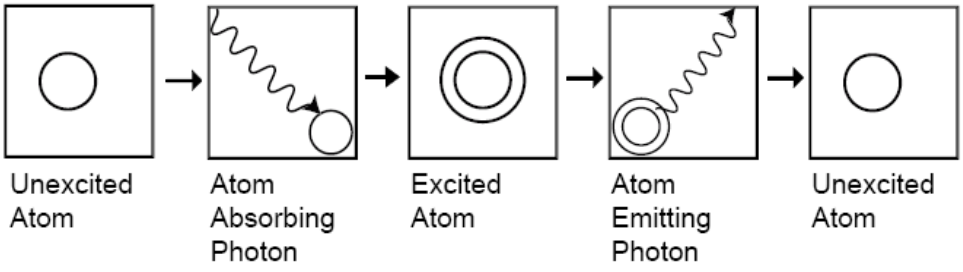

Figure 15: Spectroscopy on the atomic basis(16)

While photons are absorbed for excitation of electrons in an atom, photons are emitted for relaxation. Figure 15 shows the simple cycle of an atom from an unexcited to an excited state and then back to the starting unexcited state.

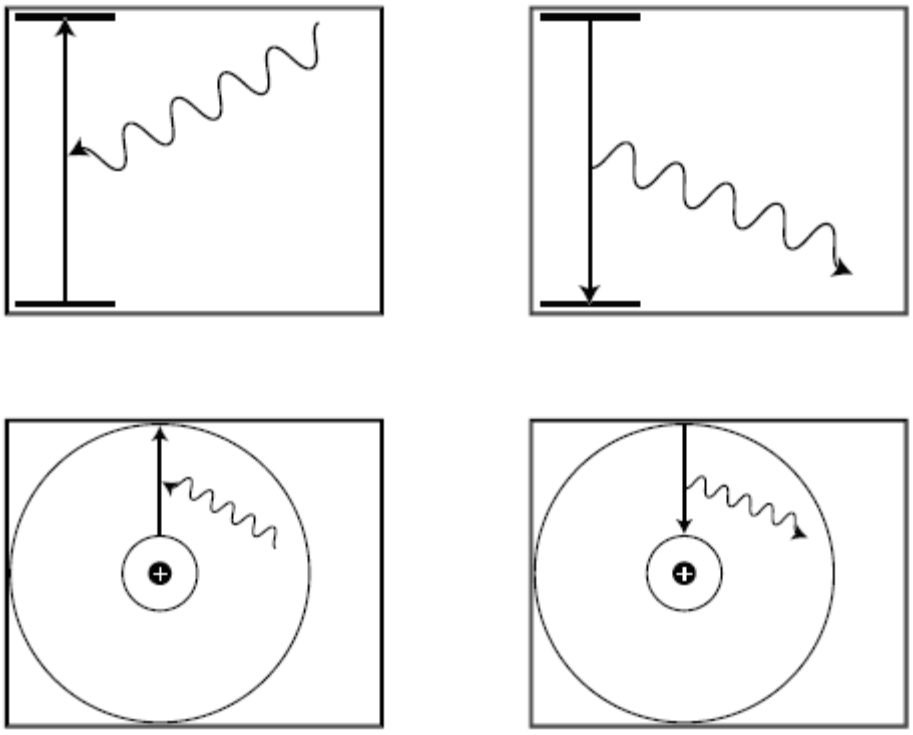

Figure 16: Effect of absorbing and emitting photons on the energy of an electron(16)

Figure 16 shows the effect of absorbing and emitting photons on the energy of an electron. The two images on top illustrate electronic energy states. The bottom energy state is the relaxed one and the upper one is the excited state of an electron. The two images on the bottom show orbits of an atom. To lift an electron up to a higher electronic energy state or

atomic orbit, energy is needed. Photons provide energy to excite an electron. Energy is absorbed by the atom and an electron is excited to a higher electronic energy state. When the electron falls from an excited state to the ground state, energy is emitted by the atom. In addition to electronic energy states, molecules have vibrational, rotational, and translational energy states.

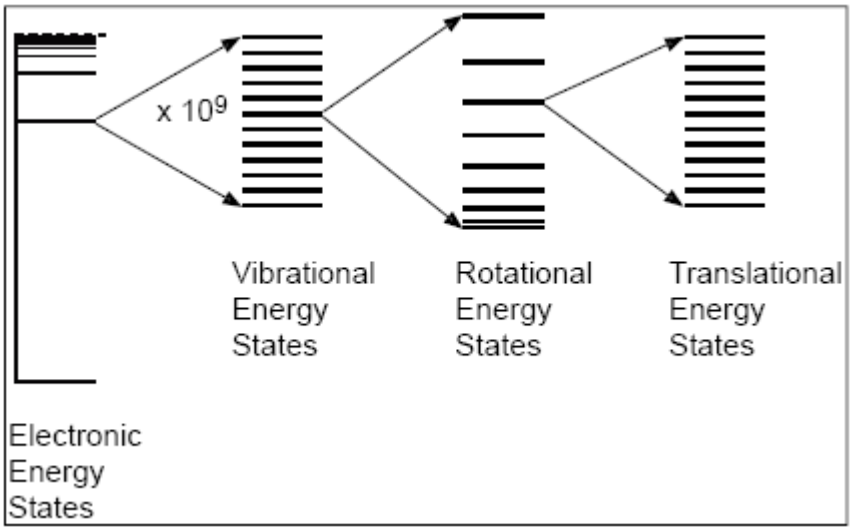

Figure 17: Molecular energy levels(16)

The effect of photons on molecular vibrations is energy dependent, as pictured in Figure 17. Compared to the energy difference between electronic energy states, vibrational energy states have less energy difference by a factor of 10^9. Excitations between rotational or translational energy states need even less energy absorption. Therefore, it is more likely that if electrons experience electronic energy-state changes, overlaps with vibrational, rotational, and translational energy-state changes will occur. Note: Solids have only electronic and vibrational energy states. Only molecules in gas or liquid phase have additional rotational and translational energy states.

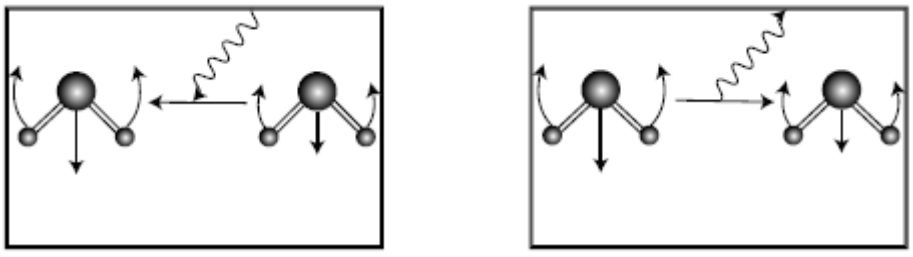

Figure 18: Effect of infrared photons on the vibrational energy of a molecule(16)

Infrared photons constitute light with wavelengths in the infrared region and therefore provide even less energy than photons from visible light. As shown in Figure 18, absorbing infrared photons can increase the vibrational energy of a molecule. Analogous to the absorption, a vibrating molecule can emit infrared photons and decrease its energy.

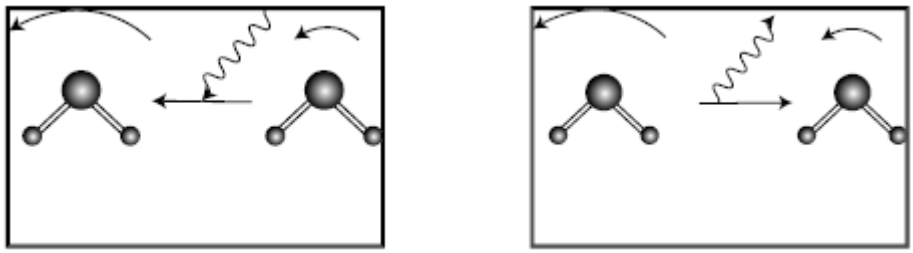

Figure 19: Effect of microwave photons on the rotational energy of a molecule(16)

Microwave photons constitute light with wavelengths lower than those of infrared light and provide therefore less energy than photons from infrared light. As shown in Figure 19, absorbing microwave photons can increase the rotational energy of molecules. Analogous to the absorption, a rotating molecule can emit microwave photons and decrease its energy.

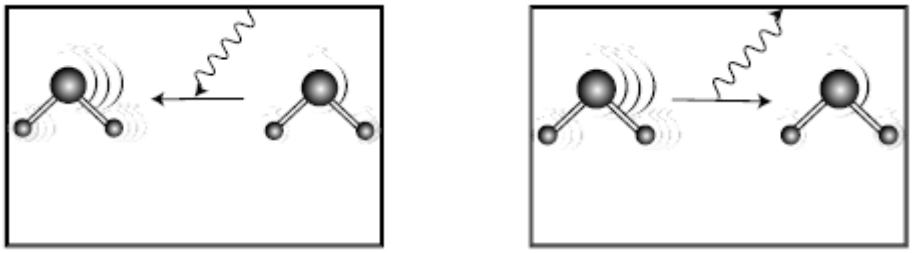

Figure 20: Effect of photons on the translational energy of a molecule(16)

In general, absorbing a photon can increase the translational energy of a molecule, as pictured in Figure 20. Analogous to the absorption, molecules that decrease their translational energy emit microwave photons and decrease their energy.

2.4.3. Classification of Spectroscopic Methods with Electromagnetic Incident Beams

The whole bandwidth from X-rays to γ-rays of the electromagnetic spectrum is used for different spectroscopy applications.

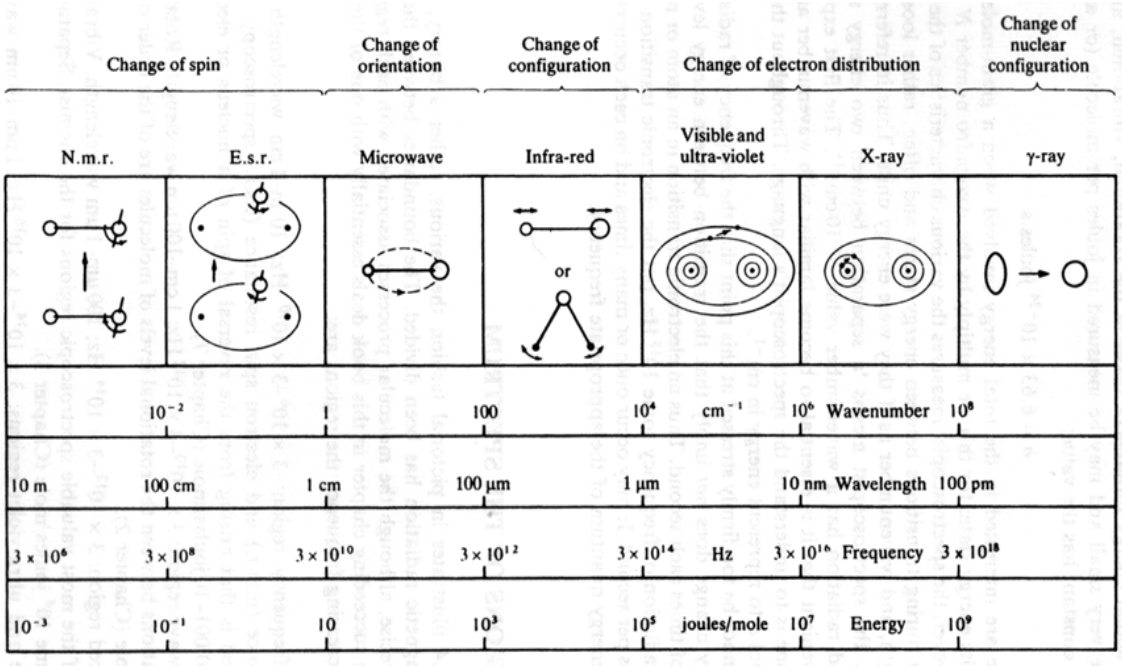

Figure 21: The regions of the electromagnetic spectrum(15)

Figure 21 shows the electromagnetic spectrum in wavenumber units, wavelength, frequency, and energy. The excitation energy increases from left to right. The images illustrate the effect of the interaction of light with matter from different regions of the electromagnetic spectrum. The effect is stated on top of Figure 21; however, transitions from one effect to the next are continuous.

2.4.4. Spectrum

A spectrum shows measured intensity, for instance emission or transmission, as a function of wavelengths. Spectra give information on the band structure of the excited atom or molecule complex. Since wavelengths and energies are coupled with $E = h * \nu$, and $\lambda = h * c \div E$ (see Equation 2 and Equation 3), the wavelengths in the spectrum give information on the energy of the emitted photons and thus on the energy difference of electronic, vibrational, and rotational states.

Line, band, and continuous spectra make up the three main types of spectrum. Heated objects emit continuous spectra covering several wavelengths of the visible light. Light bulbs are

sources of continuous spectra. Excited atoms in gas phase emit line spectra. Such spectra contain only certain frequencies or wavelengths matching the energy difference between given electronic states. This effect is used in laser technology to produce monochromatic light. Each element of the periodic system has a unique and distinguishable line spectrum.

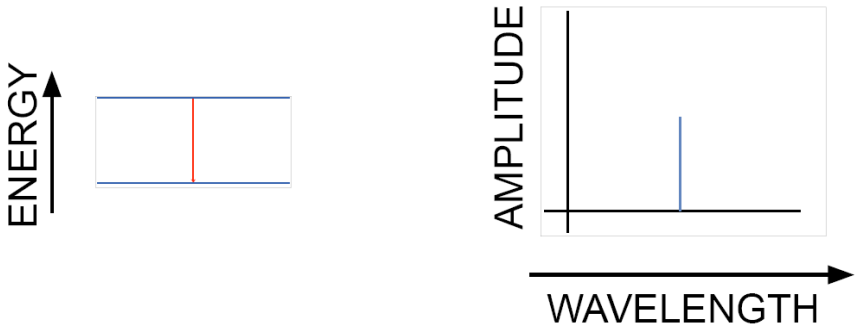

Figure 22: Electronic energy state change of an electron of an atom on the left and line spectrum on the right(16)

The energy needed to excite an electron from a relaxed electronic ground state to the next excited state is determined by the electronic states of an atom. Only full transitions of electrons from one electronic state to the next are possible, induced by absorption and emission of photons matching the electronic level difference. Figure 22 shows the relaxation of an electron from its excited state to the ground level on the left. Photons matching the energy difference between the electronic energy states are emitted and recorded with a spectrometer. The resulting emission spectrum with intensity or amplitude on the y-axis as a function of wavelength is a line spectrum, which is pictured on the right in Figure 22.

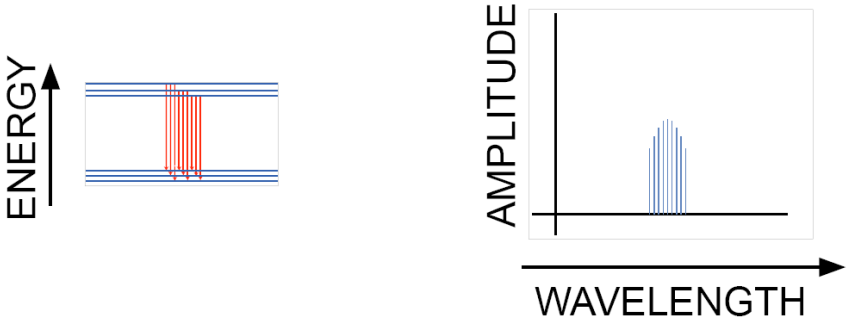

Figure 23: Electronic-vibrational energy state change of electrons of a molecule on the left and spectrum on the right(16)

The relaxation of several excited electrons of a molecule in electronic-vibrational energy state changes are depicted in Figure 23 on the left. A more complex emission spectrum is recorded and pictured on the right.

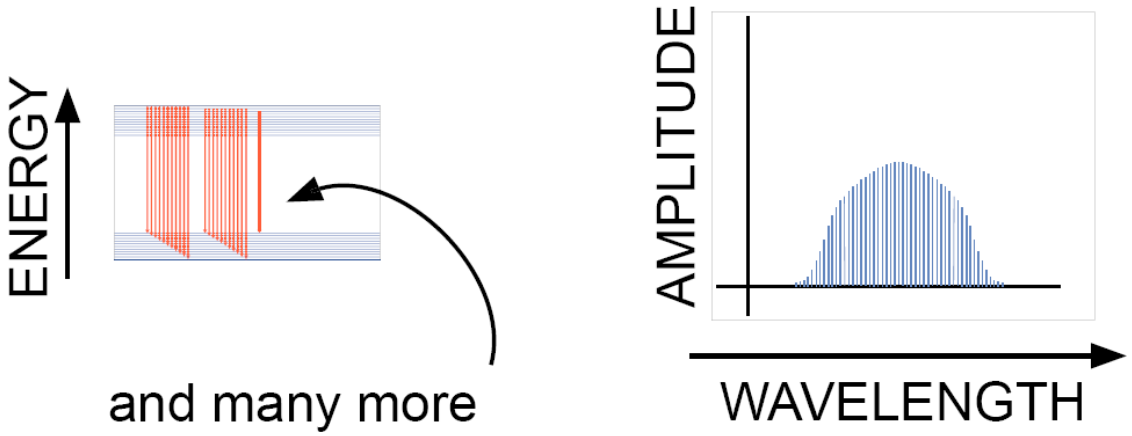

Figure 24: Electronic-vibrational-rotational energy state change of electrons of a molecule on the left, band spectrum on the right(16)

The relaxation of several excited electrons of a molecule in electronic-vibrational-rotational energy state changes is depicted in Figure 24 on the left. The recorded emission spectrum is called band spectrum and is pictured on the right respectively. It is possible to determine the electronic-vibrational-rotational energy states of a molecule from its band spectrum.

2.5. Raman Spectroscopy / Surface-Enhanced Raman Spectroscopy

Raman spectroscopy and surface-enhanced Raman spectroscopy (SERS) belong to the field of vibrational spectroscopy. Therefore, vibrational changes of the molecules of the sample will be investigated. This chapter gives information on how Raman spectroscopy and SERS work.

2.5.1. History of Raman Spectroscopy

Raman spectroscopy is a useful technique for various chemical analyses. A prominent example is the investigation of vibrational modes in molecules. In Calcutta on February 28, 1928, Professor C. V. Raman was the first to observe the scattering of light at different wavelengths not present in the incident light source when a monochromatic incident light beam was applied on a sample. The incident light beam provides less energy than required to excite electrons from one electronic level to the next. Hence, no fluorescence occurs. However, the sample can still absorb photons, changing its vibrations since the scattering of light is founded in an energy exchange between the incident photon and the investigated molecules. Therefore, the vibrational modes of molecules are seen as peak shifts from the excitation wavelength in the Raman spectra. Since every material has unique Raman spectroscopy spectral patterns, Raman spectroscopy was employed soon after its discovery to gain physical and chemical information from different materials on the molecular level. For his discovery, known as “the Raman effect,” Professor Raman was awarded the Noble prize in physics in 1930. Since then, research using Raman spectroscopy has expanded to probing molecular structures.(17 p. 3ff)

Limited sensitivity, especially for investigations of organic molecules, led to derivations of Raman spectroscopy. Some of them, such as surface-enhanced Raman spectroscopy (SERS), which was initially employed in 1974 and is observed in solid/solution, solid/gas, and solid/solid interfaces(18 p. 263), are capable of single-molecule analysis. (6 p. 113ff) Unlike Raman spectroscopy, which investigates an analyte without contaminations, SERS employs an additional metal to enhance the Raman signal of certain lines for investigating an analyte. Silver but also gold is commonly used as basis material. Enhancement factors of the normal Raman signal to 10^6 and recently up to 10^{14} in single molecule detection have been observed. (6 p. 112) In particular, investigations of complex organic molecules are favorably done with SERS, since this technique delivers sophisticated fingerprint spectra that are not obtained with normal Raman spectrum.

2.5.2. Principle of Raman Scattering

In Raman spectroscopy, a single component or material is investigated. Raman scattering occurs when electrons of a molecule are excited by a low-energy incident beam to a virtual excited state below the next-highest electronic state and fall back to another vibrational sate different from the incident one. Transitions to several vibrational states are common. Hence, the photons emitted by relaxation of the electrons have different energies and therefore different wavelengths compared to those of incident excitation beam.

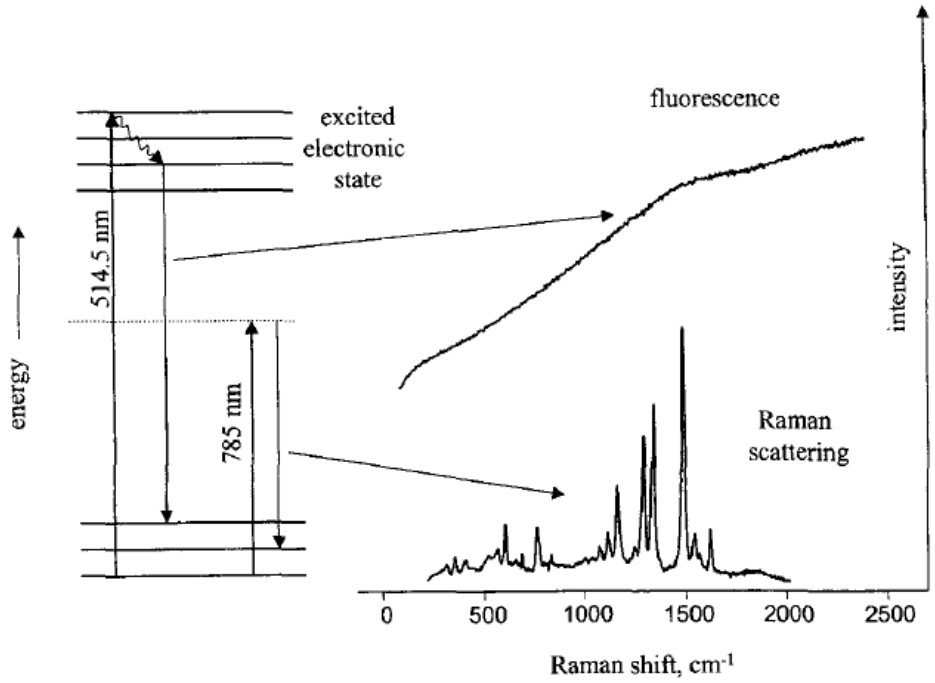

Figure 25: Comparison fluorescence and Raman scattering (19 p. 4)

A fluorescent sample is investigated with a 514.5-nm incident laser beam providing enough energy for exciting electrons into a higher electronic state, and in a second run with a low-energy 785-nm incident laser beam exciting electrons to a virtual state as depicted in Figure 25. The energies and intensities are not in scale. The fluorescence intensity is several orders higher than the Raman scattering signal and gives broad fluorescence peaks, and the energy difference of electronic states can be derived from the peak position. Although the Raman scattering signal is several orders weaker compared to the fluorescence signal, it provides more information on detailed vibrational modes of the investigated molecule. The vibrational modes are seen as individual peaks in the Raman spectrum. The resulting fluorescence and Raman spectrum are shown respectively on the right of Figure 25. At 514.5 nm excitation wavelength, fluorescence governs the spectrum and covers the weak signals from transitions between vibrational states. However, excitation with 785 nm wavelength results in a Raman spectrum giving information on changes in vibrational states. The graph shows Raman scattering intensity as a function of Raman shift in cm^{-1}. A Raman shift of 0 cm^{-1} indicates that there is no change or

wavelength shift and therefore the detected light has the same wavelengths as the incident beam. Each peak indicates a Raman shift and therefore an energy shift of the scattered photons compared to the photons of the incident beam. Light shifted to the right from zero has a lower energy than the incident laser beam. The lines are also called Stokes lines. If the scattered photons gain energy compared to the incident beam, because the excited electrons relax to a lower vibrational state compared to the incident one, blue shifts occurs, which are left from zero Raman shift in cm^{-1} in Raman spectra. These lines are called anti-Stokes lines. Stokes and anti-Stokes lines vary in intensities, but are symmetrically positioned about the Rayleigh peak at Raman shift. (6 p. 5ff)

Depending on the molecular symmetry, molecules scatter light differently from one another. This can be observed in Raman spectra as different wavenumber shifts in cm^{-1} from the incident excitation wavelength. Commonly observed single vibrations and group frequencies in Raman spectra are shown in Figure 26. The axis on the left gives the wavenumber shift in cm^{-1} from the excitation source. Each bar indicates a molecule-symmetry group or single vibration. The thickness of the bars indicates the intensity of the observed signals.

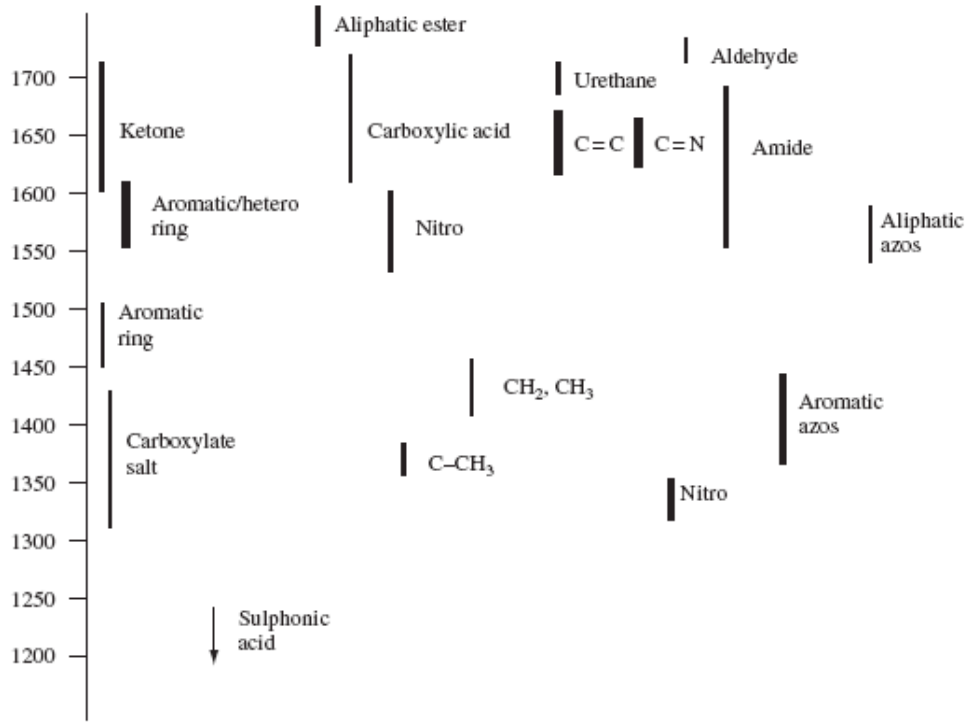

Figure 26: Single vibration, molecule-symmetry group, and an indication of possible intensities of peaks commonly identified in Raman scattering between wavenumber 1200 and 1700 (6 p. 17)

As depicted in Figure 27, after excitation of electrons with $E = h*\nu_0$ (see Equation 2) to an excited state, scattering of light occurs at different frequencies. Incident light with higher frequencies is more likely scattered than light with lower frequencies. Hence, an incident light

beam with a shorter wavelength is more likely to be scattered compared to one with a longer wavelength. This is because the efficiency of scattering is proportional to the frequency to the fourth power of the incident light (see Chapter 2.2.4).

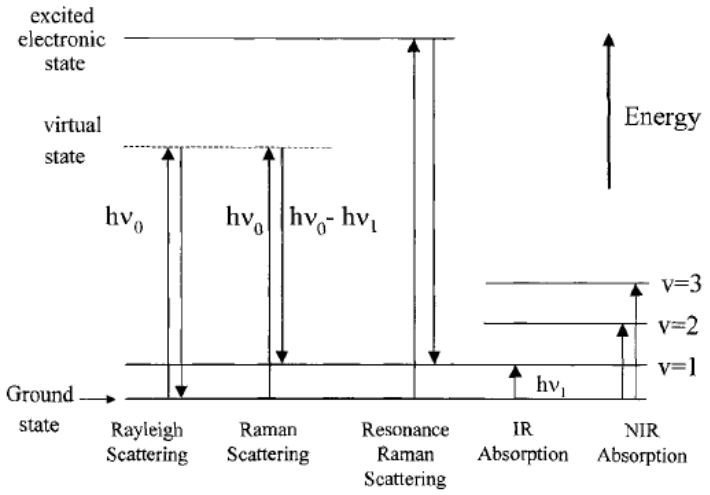

Figure 27: Electronic transitions of several types of vibrational spectroscopy (19 p. 2)

Figure 27 shows a molecular ground state, the vibrational states *v = 1 to v = 3* (also referred to as quantum states), a virtual state, and the next-highest excited electronic state, with increasing energy. The oscillating electric field of light, with lower energy than the energy difference between the ground and excited electronic states, induces short-lived virtual states that are not true quantum states of the molecule. However, the virtual states can be seen as distortion of the electron cloud of the molecule.

If the absorbed photons have the same energy as the emitted photons, Rayleigh scattering occurs. At Rayleigh scattering, no Raman shift is observed in the Raman spectrum. There are also no vibrational changes in the molecule. At Raman scattering, the excited electrons fall back to a vibrational state different from the ground state. The energy difference $E = h*v_1$ is seen in the Raman spectrum as peak with a Raman shift in cm^{-1} from zero. Resonance Raman (RR) scattering is a special form of Raman spectroscopy. Infrared (IR) and near infrared (NIR) absorption spectroscopy are also used for investigations of molecular vibrations.

2.5.3. Principle of Surface-Enhanced Raman Spectroscopy

Surface-enhanced Raman scattering occurs when a molecule is in the vicinity of a metal and excited with a low-energy incident beam. Since excitation energies of incident beams are lower than the energy gap between the highest occupied molecular orbital (HOMO) and the lowest unoccupied molecular orbital (LUMO), no fluorescence occurs. SERS spectra have a fingerprint character for every metal/molecule system. Applications of the SERS fingerprint spectra include

forensic investigations and drug testing. In addition, SERS sensors are employed as biosensors and used for quality control in the pharmaceutical industry. SERS is also a favorable technique for “identification and characterization of organic pigments and dyes used in works of art and cultural heritage material,” enabling the dating and investigation of authenticity of artwork. (20) Finally, SERS is a powerful tool in physical and chemical research on molecular vibrational modes. SERS has already proved its potential for detecting of “extremely minute quantities target molecules [down to single molecule detection]”.(21 p. 1)

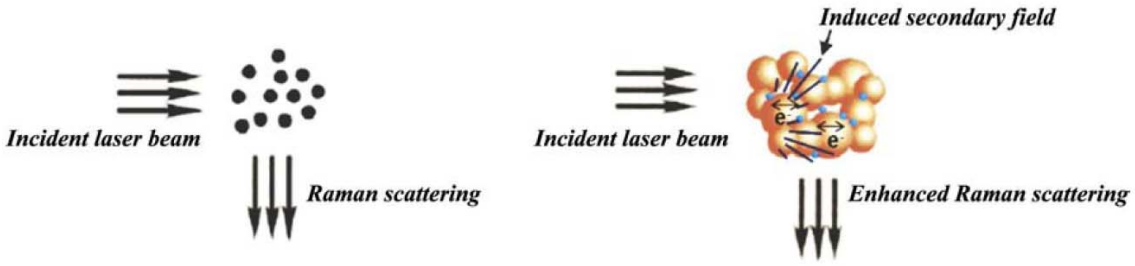

Figure 28: Comparison of normal Raman scattering on the left and surface-enhanced Raman scattering on the right (20 p. 5)

Figure 28 illustrates the difference between a sample providing Raman scattering on the left and another sample providing surface-enhanced Raman scattering on the right. The main difference is that Raman scattering is induced by an incident laser beam that is applied on a pure material, whereas in SERS an incident laser beam is applied on molecules adsorbed on SERS active metal particles. The interaction in the metal/molecule system leads to enhanced spectra lines compared to the lines in the normal Raman spectra. In a SERS metal/molecule system, the adsorbed molecule is the analyte.

In SERS, a monochromatic excitation beam is applied on a metal-analyte sample for excitation of electrons to a virtual state. The analyte is adsorbed on a metal. This is done either by mixing a colloidal metal solution with the analyte or depositing thin films of the metal and the analyte on each other. SERS investigations are commonly executed using solid samples, but samples in solution can also be investigated. The metal/molecule complex leads to spectra different from the Raman spectra. Certain lines in the spectra are strongly enhanced and new lines occur, while others are reduced compared to the normal Raman spectrum. In addition, in SERS the adsorption of the molecules on the metal surface alters the symmetry of the analyte, and therefore peak shifts in the SERS spectra occur. Enhancement factors up to 10^{14} occur at so-called hot spots where an excitation laser hits an absorbed molecule perfectly located between two metal nanoparticles. The excitation energy of the incident beam is lower than the energy difference between the HOMO and LUMO of the adsorbed molecule. Thus no electrons in the molecule are excited directly to a higher electronic state.

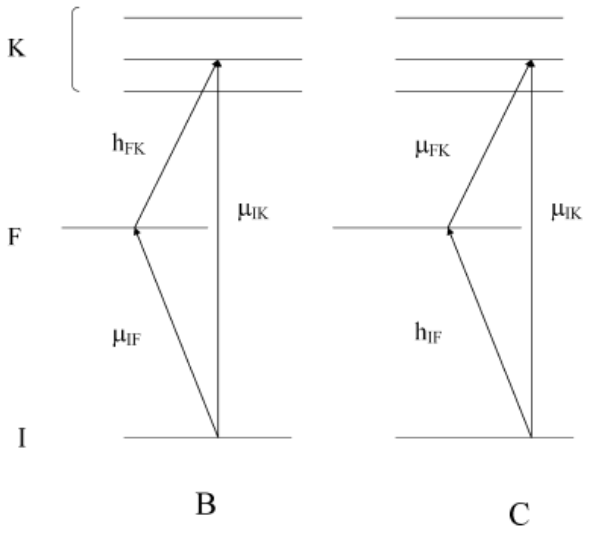

Figure 29: Energy-level diagram of the metal/molecule system(21)

However, the excitation of electrons to a charge-transfer state as depicted in Figure 29 is possible. The image schematically shows a metal/molecule system and electronic transitions. State *I* is the electronic ground state of the adsorbed molecule, *K* represents an excited state of the molecule, and *F* is a charge-transfer state. State F indicates the Fermi level of a metal that is preferably Ag, Au, or Cu. Its position has significant consequences on the electron transitions between the metal and the molecule. Depending on the excitation wavelengths and the metal/molecule system, different charge-transfer transitions are possible. Charge-transfer transitions are electron transitions between the molecule and the valence band of the metal. The charge-transfer transition moments μ_{IF}, h_{Fk} and a molecular transition moment μ_{IK} are shown in Figure 29B. In C, the transition moments are h_{IF}, $\mu_{Fk,}$ and the molecular transition moment μ_{IK} respectively. Both charge transfer from the molecule to the metal and charge transfer from the metal to the molecule are possible; however, only one direction is allowed for each specific metal/molecule system at a given excitation wavelength and temperature. The coupling parameter between the transition moments μ_{IK} and μ_{IF} in case B is h_{Fk}. The coupling parameter between the transition moments μ_{IK} and μ_{Fk} in case C is h_{IF}. The coupling terms and the transition moments are used for the calculation of the polarization of the analyte, which is not part of this work (see Chapter 3.1).

Differences between normal Raman and SERS:	
Normal Raman :	SERS:
- the analyte is investigated directly	- the analyte is adsorbed on a metal or semiconductor
- no charge-transfer state	- new charge-transfer level “F” due to the employed metal or semiconductor
- the main contributor to Raman signals are incident photons that excite electrons in the analyte	- main contributors are surface plasmons (from a metal), charge-transfer transitions (between a metal or semiconductor and a molecule), and molecular resonances
- Raman spectra are governed by totally symmetric a_1 modes of the molecule	- SERS spectra are governed by non-totally symmetric b_2 modes of the analyte
- the orientation of the analyte is random with respect to the incident light beam	- the orientation of the analyte is governed by how the analyte is adsorbed on the metal or semiconductor surface (21)

Table 1: Differences between normal Raman and SERS

2.5.4. Mechanisms in SERS

Three mechanisms contribute to the enhancement of the SERS signal. Each of them is seen in the intensity-versus-wavelength spectrum as a strongly enhanced peak (see Figure 31) with the peak center at a certain excitation wavelength. The three main contributors to the SERS signal are electromagnetic enhancement, molecular transition of electrons, and charge-transfer enhancement.

- Electromagnetic enhancement occurs due to an incident electromagnetic wave that excites electrons from the valence band of the metal to an excited state. Electrons in such an excited state are called surface plasmons.
- Molecular transitions of electrons are electronic transitions between allowed energy states in the molecule, for instance electronic transitions from a filled π-orbital (HOMO) to an unfilled π^*-orbital (LUMO).
- Charge-transfer enhancement is obtained from electronic transitions from the molecule to the metal or from the metal to the molecule in the metal/molecule system. These transitions are called charge-transfer transitions.

Depending on the metal/molecule system and the excitation wavelengths, each of the contributors to the Raman signal enhancement can reach resonance. At each resonance, the vibrational modes in the SERS spectrum show the greatest enhancements. In general, SERS signals of an analyte are enhanced by a factor of 10^6 compared to the normal Raman signal. At certain molecules (for example crystal violet), overlaps of all three resonances can result in enhancement factors up to 10^{14} (obtained in single molecule detection).(1)

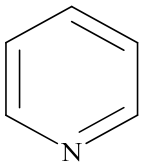

Figure 30: Pyridine C_5H_5N

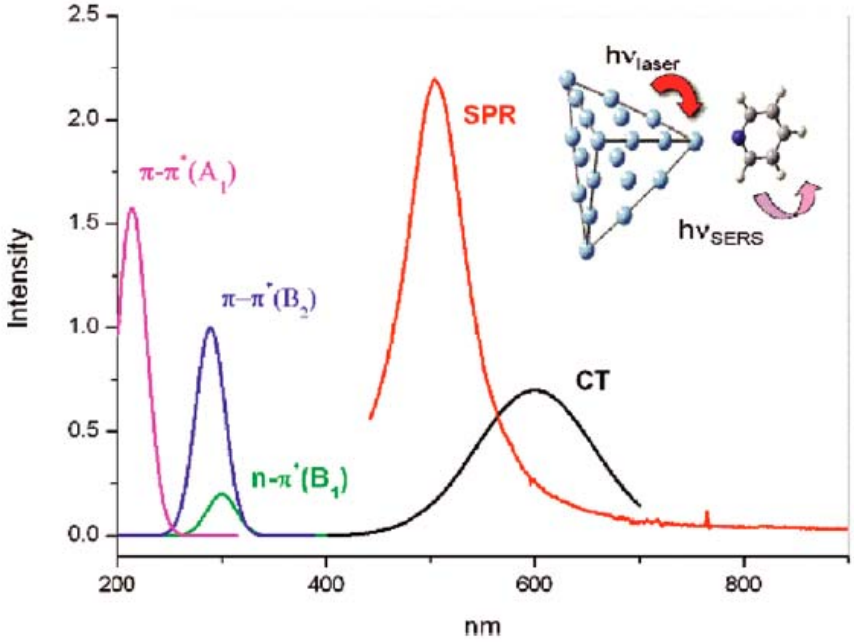

Figure 31: Resonances in a pyridine-Ag nanoparticle system(21)

Surface-plasmon resonance (SPR), charge-transfer resonance (CT), and molecular transition of pyridine (aromatic heterocyclic organic molecule, see Figure 30) adsorbed on Ag nanoparticles are depicted in Figure 31. The intensity of each resonance is shown as a function of excitation wavelengths of the incident laser beam. Each resonance occurs at a certain frequency with peak width and oscillator strength. As mentioned previously, overlaps of resonances are possible, and might result in even stronger enhancements of SERS signals at the resonance excitation wavelength. There are three different molecular transitions of the pyridine molecule. The molecular transitions A1, B1, and B2 are irreducible representations. The first molecular π-π^* transition is assigned as totally symmetric stretch A1; the other two molecular transitions are assigned as non-totally symmetric stretches B1 and B2. It can be observed that the oscillator strengths of the molecular transitions are A1>B2>B1. This indicates for the recorded SERS spectra of an Ag/pyridine system that the normal modes behave $a_1>b_2>b_1$ respectively. This is also true for adsorbed molecules with the same or sufficient symmetry compared to pyridine.(21 p. 6) Depending on the position in the graph intensity versus wavelength, several enhancements may come into account at different excitation wavelengths. In addition, all three enhancement contributors are joined together as shown in Figure 29.

2.5.5. SERS Spectra Dependence

Since in SERS molecules are adsorbed on the metal surface, how the molecule is bound to the metal surface influences the overall enhancement factor significantly. For SERS it is important that low surface coverage of the adsorbed molecules on the metal is accomplished.

A surface coverage–dependence study showed coverage as low as 0.07 of a monolayer results in resonance enhancement of the peaks in the spectrum. Multilayer coverage reduces the enhancement factor significantly distinguish the SERS enhancement.(21 p. 2)

The orientation of the adsorbed molecule on the nanoparticle surface influences the enhancement factor in SERS spectra significantly. Surface plasmons induce an electric field perpendicular to the metal surface. Hence, molecules adsorbed perpendicular to the metal surface get differently polarized compared to molecules that lie flat on the metal surface.

The Fermi level of the metal and the position of the HOMO and LUMO level of the adsorbed molecule govern the charge-transfer direction. A charge transfer from a metal to the adsorbed molecule is achieved in molecules with a low-lying unfilled π-orbital compared to the Fermi level of the metal. Such a metal-to-molecule transfer occurs for instance in an Ag/pyridine system. An example of a molecule-to-metal charge transfer due to a more highly situated π-orbital of the molecule is the Ag/NH_3 or Ag/piperidine system. In addition, maximal CT enhancement occurs at transitions from or to the Fermi level of the SERS active metal used.

The nanoparticle size and shape of the metal govern the available surface area and therefore influence the SERS spectra.

The oscillator strengths and signal damping, which govern the observed intensities and peak widths in the SERS spectra. For calculations, the damping factors are considered in the denominator of Equation 9. The SERS enhancement factor is proportional to the inverse fourth of the damping parameter at each resonance (ε_2, γ_{FK}, γ_{IK}).

To conclude correctly about each contribution, it is crucial to record spectra at different wavelengths, since SPR, CT, and molecule-to-metal resonances have different peak widths, oscillator strengths, and positions in the spectra to.

Sample requirements for SERS:

To receive high enhancement factors in SERS compared to the normal Raman signal, it is essential for a metal to meet certain requirements.

- The employed metal must lead to an enhanced Raman signal and therefore be SERS active;
- effective surface adsorption of an analyte to the metal employed in SERS is crucial;
- the metals used should not oxidate, since it might alter the spectra.

Silver, gold, and copper are established metals used in SERS.

Challenges in SERS:

- A multilayer of adsorbate on the metal can distinguish the SERS signal;
- the adsorption process of molecules to nanoparticle surfaces is not completely understood;
- laser absorption might result in degeneration or transformation of organic adsorbates through sample heating;
- the degree of charge transfer ($p_{CT}(\nu_i)$) in the SERS spectra is power dependent on the incident laser beam;
- targeting on the hot spots in single molecule detection is difficult;
- surface homogeneity on the sample may be difficult to be controlled;
- the number of possible vibrational modes increases with the atomic number of the atom (3N-6 or 3N-5), making complete investigations of all vibrational modes of even small molecules difficult;
- the positions of baseline anchor points at SERS spectra analysis for background subtraction alter peaks properties;
- hidden overlaps of resonances and vibrational modes are difficult to investigate;
- even minute highly active SERS material contaminations like sulfur in a sample make investigation of the analyte nearly impossible since the contaminator governs the spectrum. (6 p. 116ff)

Advantages of SERS:

- A fingerprint character of the spectrum from complex organic molecules is possible to obtain;
- SERS gives specific molecular information of complex organic molecules; (6 p. 122 ff)
- SERS allows qualitative analysis of compounds;
- high enhancements of peaks compared to normal Raman eases qualitative analysis;
- most organic molecules like dyes used in art preserve SERS activity even after centuries; since even a small sample cannot be removed from artworks, SERS is used for investigating;
- SERS has the ability to detect molecules that occur in minute concentration;
- SERS can detect single molecules;
- SERS has the ability to detect complex organic molecules since no fluorescence overlaps signals obtained from vibrational levels;
- the SERS technique can be used for biosensors;
- sample preparation is relatively easy, since no special equipment is required;
- investigation of band structures and vibrational modes of molecules is possible.

2.5.6. Noise Signals in Raman Signals

During the recording of spectra, so called “noise signals” distort the information of the graph. An output signal must be at least three times stronger than the occurring noise signal to make identifications in the spectrum possible. Noise signals are unwanted spikes or background overlays that are mainly caused by

- the detector (electronic noise)
- the amplifier (electronic noise)
- the sample (due to thermal motion or induced degradation of molecules through the incident beam)
- the excitation source, flicker noise (intensity instability of the incident beam) (19 p. 56).

Technological advances in detectors have led to spectra with high signal-to-noise ratios (SNR) up to 280. The following example illuminates how technological progress in detector equipment has enhanced the signal-to-noise ratio significantly.

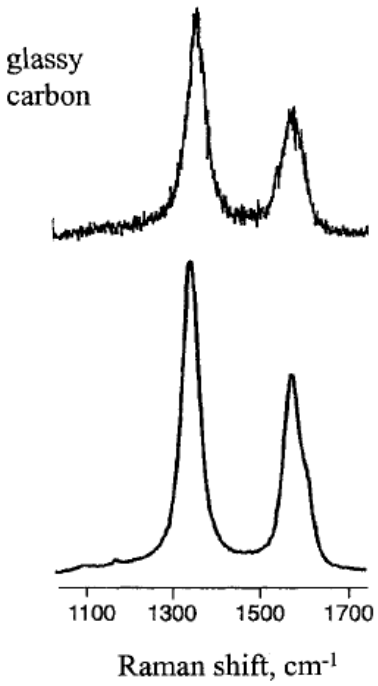

Figure 32: Raman spectra of solid glassy carbon (19 p. 63)

Both Raman spectra of solid glassy carbon in Figure 32 were recorded at 50 mW with an 514.5 nm excitation wavelength. The spectrum at the top was recorded with a "Spex 1403 double monochromator with photon counting PMT," which was a state-of-the-art spectrometer in 1985. A scanning time of 20 min was required to obtain a SNR of 28.

The second spectrum was obtained with a "Chromex 250 spectrograph, black thinned silicon CCD," which is a multichannel CCD spectrometer from 1996. A scanning time of 5 sec was required and an SNR of 280 was obtained. (19 p. 49)

SNR for the peak intensity is calculated with the following equation:

Equation 5

$$SNR = \frac{average\ peak\ height, S}{standard\ deviation\ of\ the\ peak\ height, \sigma_y}$$

To obtain an accurate value of SNR, several SNR measurements have to be averaged.

Note to the experimental section in Chapter 4:

In the wavelength-dependence study investigated in this work, a Spex 1401 double monochromator with photon counting was used.

In the size-dependence study investigated in this work, a CCD spectrometer was used.

2.5.7. Instrumentation

The general instrumentation for Raman spectroscopy can be split into four basic components: an excitation laser, an optical sampling system, a wavelength separator, and a detector. In addition to the main components, proper software, several filters, and optical lenses are employed. Depending on the excitation wavelengths, two fundamental designs for Raman spectroscopy and SERS are available. The dispersive multichannel Raman spectrometer is used for wavelengths in the visible and UV regions, while the Fourier-transform (FT) interferometer Raman system is used for excitation wavelengths higher than 1047 nm and therefore in the near-infrared (NIR) region. Since scattering of light distributes in all directions, arrangements in 180° scattering and 90° scattering modes are found in modern Raman systems. The 180° and 90° scattering arrangements are depicted in Figure 33.

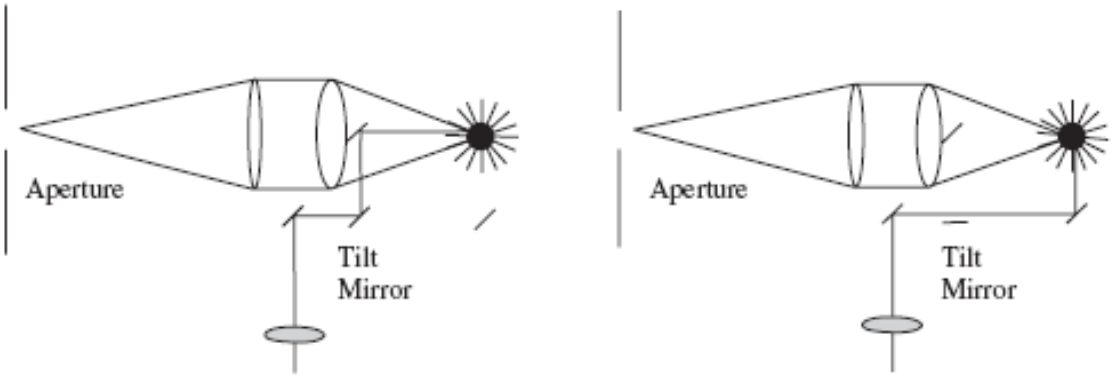

Figure 33: Arrangement for 180° scattering on the left and 90° scattering on the right (6 p. 25)

In the arrangement for 180° scattering, a special mirror/filter is placed beyond the tilt mirrors, leading the laser beam to the sample and allowing only scattered light with frequencies different from the incident laser beam to pass through the aperture of the spectrometer. Therefore, Rayleigh scattered light or reflected light from the sample is led back into the laser. In the 90° scattering arrangement, scattered light perpendicular to the incident beam is collected as depicted in Figure 33 on the right. In the 90° scattering arrangement no special mirror/filter is needed before the aperture of the spectrometer, since the path of Rayleigh scattered light or reflected light does not point toward the aperture. The 180° system is preferred used because of sampling convenience.

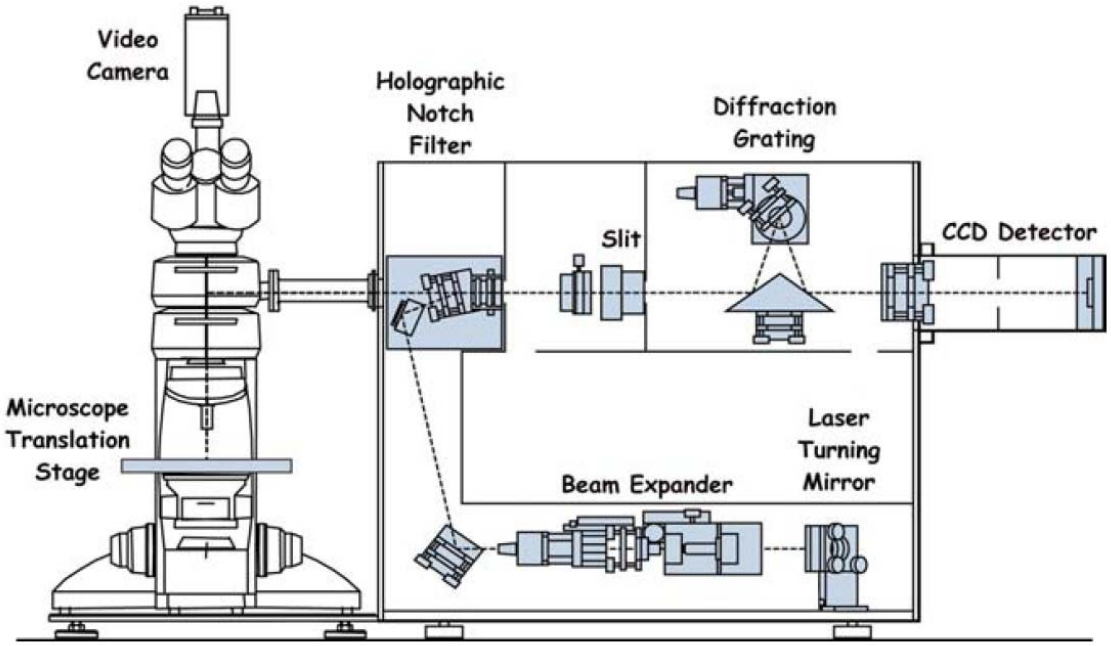

Figure 34: Schematic dispersive Raman spectrometer (22 p. 3)

A dispersive Raman system is depicted in Figure 34. It is called a dispersive Raman system since a grating device is used for diffraction of light. The instrument consists of a moveable sample stage, a video camera, a laser section with optics, diffraction grating, and a CCD detector. The system is in 180° scattering arrangement. The excitation laser beam is sent to the microscope and focused on the sample. Scattered light is collected by the same lens at the microscope and sent to the holographic notch filter. There scattered light with Raman shift to the incident beam are allowed pass to the spectrometer. Diffraction grating is used to split the scattered light beam into its spectrum before it enters the CCD detector. (23 p. 45ff chap. 3)

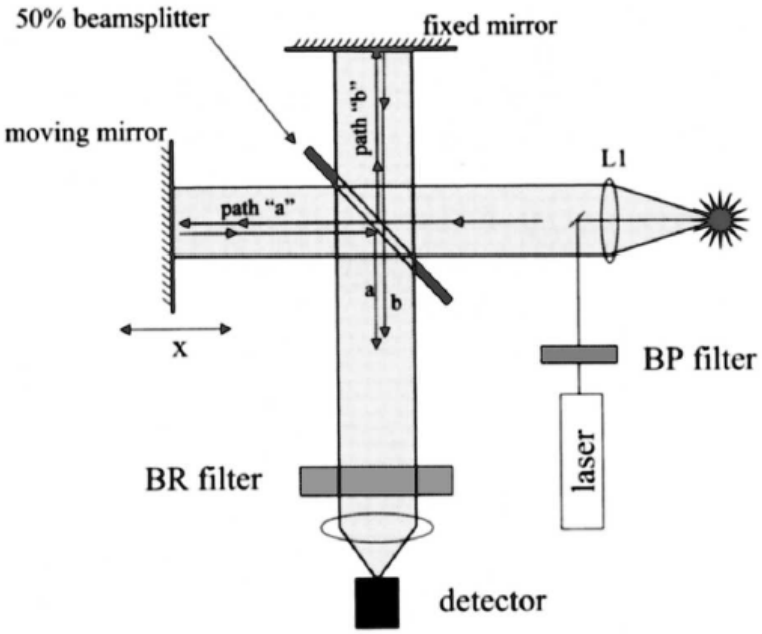

Figure 35: Schematic FT-Raman spectrometer (19 p. 226)

A schematic nondispersive Raman system with a Fourier-transform interferometer is depicted in Figure 35. The system runs in a 180° scattering arrangement as depicted in Figure 33. The scattered light from the sample is split into two beams at the 50% beamsplitter. One beam takes path “a” to a moving mirror that moves with constant speed back and forth at a certain frequency dependent on the path length “x” in Equation 6. The other beam takes path “b” to a fixed mirror. After reflection from the mirrors, the beams are united and sent into the detector. Because of the moving mirror, the two beams experience constructive and destructive interference.

Constructive interference and therefore the highest signal at the detector are reached if the following condition is fulfilled:

Equation 6

$$2 * x = m * \lambda$$

m is an integer and *x* is the path length of the mirror.

The mirror travel path and the resolution are interconnected in the following way: the longer the mirror travels, the more periods of scattered light are observed, and the higher the resolution in the resulting spectrum. In addition, to receive definite spectra more multiple runs on the sample have to be preformed and averaged.

Generalizations pertaining to laser wavelengths:	
Shorter Wavelength	Longer Wavelength
Excitation wavelength λ from 200 to 800 nm Large cross section (1/ λ^{-4} dependent) Dispersive spectrometer Higher background Higher SNR Lower detector noise	Excitation wavelength λ higher than 1047 nm Smaller cross section (1/ λ^{-4} dependent) Nondispersive spectrometer (FT) Lower background Lower SNR Requires higher laser power in mW

Table 2: Influence of excitation wavelength on SERS spectra

Generalizations pertaining to spectrometer:	
Dispersive Raman / CCD detector advantages	FT-Raman advantages
Sensitive Higher SNR Lower laser power No or hardly any moving parts	High cm-1 accuracy Better fluorescence avoidance (low background especially for organic samples) Collects signal from all wavelengths simultaneously Resolution is constant across the entire spectrum
Dispersive Raman / CCD detector disadvantages	FT-Raman disadvantages
Trade-off between spectral coverage and resolution Resolution varies across the spectrum (since the grating is linear to wavelengths but not to wavenumbers) More fluorescence (since more electronic transitions occur in the UV and visible region than in the IR region)	Lower SNR Higher laser power in mW is required (since Raman scattering is proportional to λ^{-4}) Self-absorption of the Raman light generated by a NIR laser might occur Moving part (mirror) in an FT-Raman system (19 p. 76ff) (23 p. 11ff chap. 2)

Table 3: Advantages and disadvantages of dispersive and FT Raman systems

2.5.8. Spectroscopy Units

Spectra with intensity on the y-axis and wavelength on the x-axis have the x-axis often labeled with different units. Most commonly used in SERS is the Raman shift $\Delta\omega_{Raman}$ in cm^{-1} from the incident laser beam. The absolute wavenumber in cm^{-1} of a specific wavelength in nm can be calculated as follows.

Equation 7

$$\omega = \frac{1}{\lambda} * 10^7 [\frac{nm}{cm}]$$

The Raman wavenumber shift $\Delta\omega_{Raman}$ in cm^{-1} from a specific wavenumber, commonly from the laser wavelength λ_L, is calculated as follows. (6 p. 3)

Equation 8

$$\Delta\omega_{Raman} = \frac{1}{\lambda_L - \lambda_{Raman}} * 10^7 [\frac{nm}{cm}]$$

Since the Raman shift is calculated as the inverse subtraction of two wavelengths in nm, Raman shift changes do not behave linearly to wavelength changes in nm.

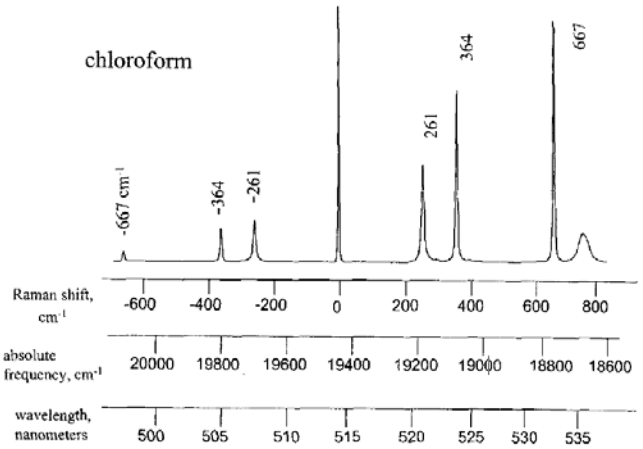

Figure 36: Raman spectra with Stokes and anti-Stokes lines and different spectroscopy units on the x-axis (19 p. 2)

The Raman spectrum in Figure 36 shows Stokes and anti-Stokes lines from a chloroform sample at excitation wavelength 514.5 nm which is set 0 cm^{-1}. The x-axis is given in wavelength in nm, the absolute frequency or wavenumber in cm^{-1} and the Raman shift from the excitation beam in cm^{-1}. Nearly all SERS spectra use the Raman shift in cm^{-1} as x-axis labeling.

3. Research

3.1. Calculations in SERS Spectra

Calculation of polarizability of an analyte:

For calculations, all three mechanisms are summarized by John R. Lombardi and Ronald L. Birke in “A Unified Approach to Surface-Enhanced Raman Spectroscopy”(1 p. 5) in the following equation:

Equation 9

$$R_{IFK}(\omega) = \frac{\mu_{KI}\mu_{FK}h_{IF}\langle i|Q_k|f\rangle}{((\varepsilon_1(\omega)+2\varepsilon_0)^2+{\varepsilon_2}^2)({\omega_{FK}}^2-\omega^2+{\gamma_{FK}}^2)({\omega_{IK}}^2-\omega^2+{\gamma_{IK}}^2)}$$

The first term in the denominator governs the enhancement in the SERS spectra contributed by SPR, the second term the contribution by CT, and the third term the contribution of the molecular resonance. The surface-enhanced Raman intensity is proportional to $|R_{IFK}(\omega)|^2$. (Calculations on each contributor or on the polarizability of an analyte are not performed in this work.)(21 p. 3)

Calculation on the degree of charge transfer ($p_{CT}(\nu_i)$):

$p_{CT}(k)$ is the degree of charge transfer

k is an index used for individual lines in the SERS spectra

Equation 10

$$p_{CT^{(k)}} = \frac{\mathrm{I^k(CT)} - \mathrm{I^k(SPR)}}{\mathrm{I^k(CT)} + \mathrm{I^0(SPR)}}$$

- $I^k(CT)$ is a line where CT adds contribution to the SERS intensity.
- To calculate $p_{CT}(k)$, two reference lines without charge transfer (CT) are needed.
    - First, the intensity of the line “k” without charge-transfer contribution $I^k(SPR)$ is needed. This can be obtained in electrochemical measurements at the same excitation wavelength, where CT was observed in the spectrum, by varying the applied potential. In this setup the SPR contribution stays constant and can be determined

- Second, a totally symmetric line (a_1 mode) is needed. Since totally symmetric lines are only enhanced by SPR, the line is called: I^0(SPR).
  Note: For totally symmetric a_1 lines, I^k(SPR) = I^0(SPR), and for non-totally symmetric b_2 lines, I^k(SPR) = 0 or very close to 0.

Value of $p_{CT}(\nu_i)$	Meaning
0	- there is no CT, the spectrum is governed by SPR
1/2	- SPR and CT govern the spectrum equally
1	- the spectra is governed by CT

Table 4: Meaning of $p_{CT}(\nu_i)$ values

For $p_{CT}(\nu_i)$ value calculations it is important to record SERS spectra at a minimum of two different excitation wavelengths. This must be done in order to find b_2 lines that are affected only by CT and a_1 lines that are affected only by SPR. Figure 37 shows SERS spectra of PATP on Ag recorded at 514.5 nm and 1064 nm. All b_2 lines are marked and a_1 lines are unmarked. At 1064 nm, CT hardly occurs since the excitation wavelength is far from charge-transfer resonance. Therefore, all b_2 lines must be distinguished or reduced significantly. The lines ruling the Ag/PATP spectra at 1064 nm are assigned as a_1 lines. A strong a_1 line like the one at 1078 cm^{-1} can be used as I^0(SPR). Given the fact that $p_{CT}(\nu_i)$ of a b_2 line is calculated, I^k(SPR) = 0. This leads to the following equation, which is commonly used for $p_{CT}(\nu_i)$ calculations of b_2 lines.

Equation 11

$$p_{CT^{(k)}} = \frac{b_2/a_1}{b_2/a_1 + a_1/a_1} = \frac{R}{R+1} \text{ with } R = \frac{a_1}{b_2}$$

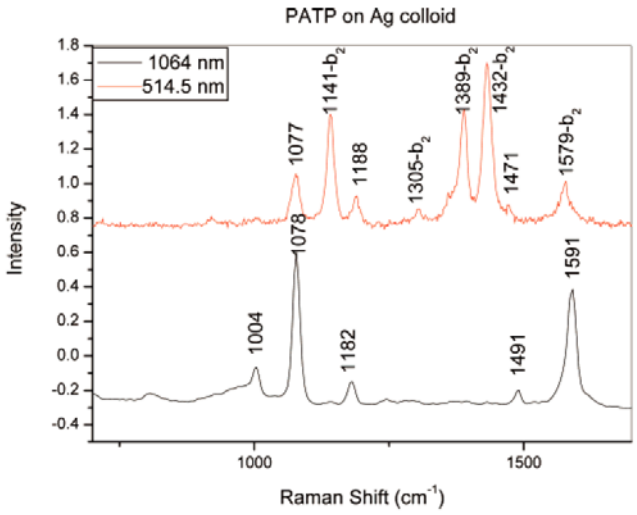

Figure 37: SERS of PATP on Ag colloids at 514.5 nm and 1064 nm(1 p. 7)

a_1 peak intensity of a totally symmetric mode

b_2 peak intensity of a non-totally symmetric mode

3.2. P-aminothiophenol (PATP) in SERS

P-aminothiophenol, or PATP (C_6H_7NS), is a well-known aromatic molecule with two different active groups, one amino group ($–NH_2$) and a thiol group (–SH), at para position. Therefore, it can act as an H^+ acceptor at the amino group and as an H^+ donor at the thiol group. Its molecular weight is 125.19 g/mol. The highest occupied molecular orbital (HOMO) of PATP is at –3.03 eV, and the lowest unoccupied molecular orbital (LUMO) is at –7.16 eV below the vacuum level. PATP is a plane molecule that is able to adsorb to the surfaces of two different materials with its thiol and amino group. Figure 38 shows the PATP molecule in 3D on the left and in the Lewis structure on the right.

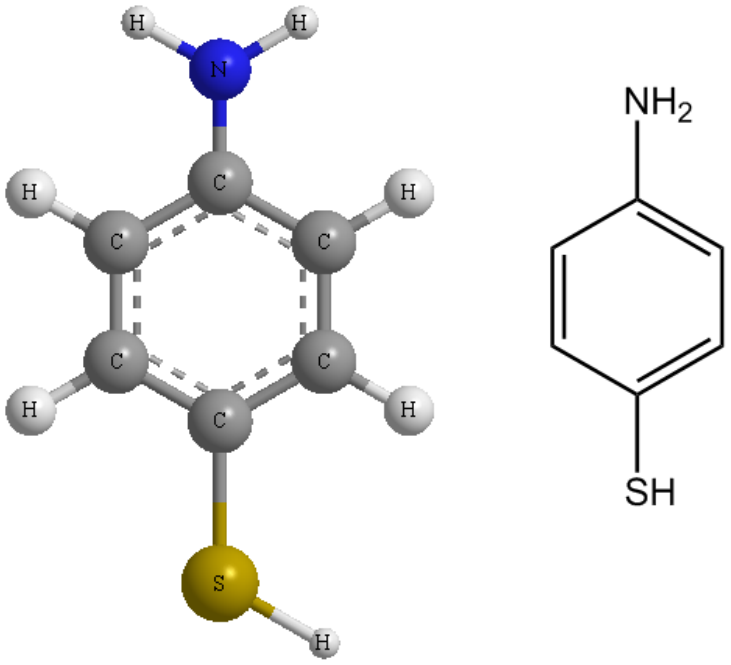

Figure 38: PATP molecule 3-dimensional on the left and Lewis structure on the right

A normal Raman spectrum from PATP alone is compared with the SERS signal obtained from the structure Ag/PATP. In the latter structure, PATP is adsorbed with the thiol group to the Ag surface. For comparison, a PATP Raman spectrum and a PATP SERS spectrum are shown in Figure 39. The graph shows intensities in arbitrary units versus wave-number shift in cm^{-1}. The intensities are not plotted to scale. The SERS spectrum of PATP deposited on an eight-nm-thick Ag film is shown in (a), while the normal Raman spectrum of PATP in solid state is shown in (b). Both spectra were recorded at 514.5 nm excitation wavelength at 50 mW. The figure shows that peaks are at slightly different positions in the normal Raman spectrum compared with the ones in the SERS spectrum. In addition, several peaks gain or lose intensity in the SERS signal and new peaks occur that have not been observed in the normal Raman spectrum. Moreover, the normal Raman spectrum shows peaks

that are no longer observed in the SERS spectrum. In general, the prime peaks in the SERS spectrum show enhancements that are not reached in the normal Raman spectrum.

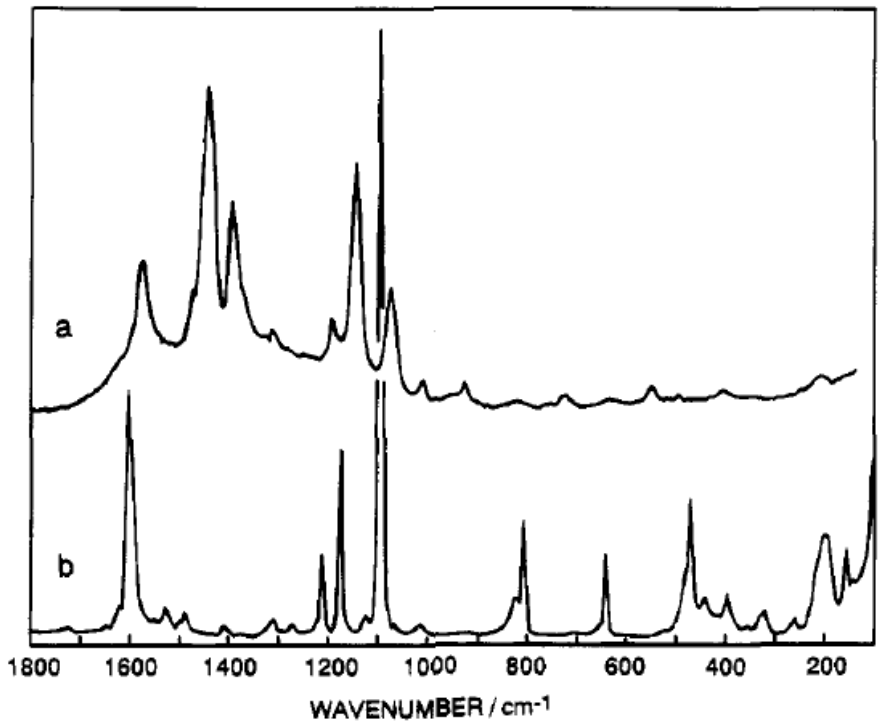

Figure 39: (a) SERS spectrum of PATP adsorbed on an 8-nm-thick silver film, (b) normal Raman spectrum of PATP in the solid state (24 p. 2)

Table 5 gives an overview of the strongest lines and therefore vibrational modes in the Raman and SERS spectrum of PATP. The numbers in the first two columns indicate the wavenumber shifts in cm^{-1} that are followed by the notes vs, s, m, and s, giving the strength of enhancement compared to the other peaks observed in each spectrum respectively.

Bulk Raman [cm^{-1}]	On silver surface SERS [cm^{-1}]	Assignment
1595 s	-	ν_{CC}, 8_a (a_1)
1572 c	1573 m	ν_{CC}, 8_b (b_2)
1445 c	1440 vs	$\nu_{CC} + \delta_{CH}$, 19_b (b_2)
-	1391 s	$\delta_{CH} + \nu_{CC}$, 3_b (b_2)
1206 m	1190 w	-
1173 m	-	δ_{CH}, 9a (a_1)
-	1142 vs	δ_{CH}, 9_b (b_2)
1089 vs	1077 m	ν_{CS}, 7_a (a_1)
799 m	-	$\nu_{CH} + \nu_{CS} + \nu_{CC}$, 1 ($a_1$)
634 m	-	γ_{CCC}, 12 (a_1)
463 m	-	γ_{CCC}, 6 (a_1)
196 m	-	$\pi_{CN} + \pi_{CS} + \tau_{CC}$, 10_b (b_1)

Table 5: Peak assignment of the PATP molecule to the vibrational modes in the Raman and in the SERS spectra

vs: very strong; s: strong; m: medium; c: bands are only observed in the ultraviolet resonance Raman spectrum at 309.1 nm

a_1 modes are totally symmetric vibrations
b_2 modes are non-totally symmetric vibrations
ν: stretch
δ: bend
π: wagging
τ: torsion

The strongest vibrations in the Raman spectrum of PATP are of a_1 symmetry. The modes are 1595 ν_8a a_1, 1173 ν_9a a_1, 1089 ν_7a a_1, 799 ν_1 a_1, 634 ν_{12} a_1, and 463 ν_6a a_1.

The SERS spectrum is dominated by four b_2 and one a_1 vibrational modes. The modes are 1573 ν_8b b_2, 1440 ν_{19}b b_2, 1391 ν3 b_2, 1142 ν_9b b_2, and 1077 ν_7a a_1. All four b_2 modes correspond with the main modes in the benzene ring vibration.

The electronic energy levels and vibronic couplings of PATP adsorbed on Ag in SERS are depicted in Figure 40. The Fermi level of Ag is indicated at the starting point for M_{mK} transition, I is the HOMO of the PATP molecule, and K is the LUMO of the PATP molecule. The excitation frequency needed to excite electrons from the Fermi level of Ag to the LUMO level of the PATP molecule is indicated with ω. The charge-transfer transition M_{mK} can borrow additional intensity from the allowed transition M_{IK}. The vibronic coupling term h_{IM} closes the charge-transfer process.

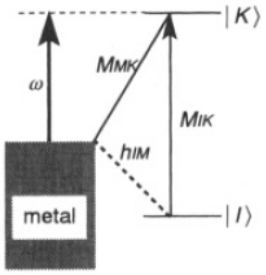

Figure 40: Charge-transfer process: SERS of PATP adsorbed on Ag (24 p. 6)

Summary:

- Different lines are enhanced in the normal Raman and in the SERS spectrum of PATP.
- While in the normal Raman spectrum of PATP six a_1 vibrational modes govern the spectrum, four b_2 and one a_1 mode govern the SERS spectrum.
- The enhanced modes ν_8b b_2, ν_{19}b b_2, ν_3 b_2, and ν_9b b_2 in the SERS spectrum resemble the main ring vibrational modes of benzene.
- PATP is charge-transfer active.
- Since PATP peaks are assigned in SERS (see Table 5), $p_{CT}(\nu_i)$ calculations are possible

3.3. ZnO Nanoparticle Size-Dependence Study with 4-MPy

A size-dependence study of ZnO nanoparticles with 4-marcaptopyridine (4-MPy, see Figure 41) adsorbed on the semiconductor surface is shown in Figure 42. The intensities in arbitrary units (A.U.) as a function of Raman shift in cm^{-1} of six different samples with ZnO nanoparticles sizes 18.2 nm, 23.8 nm, 25.2 nm, 27.7 nm, and 30.6 nm are depicted. Each spectrum was recorded at 1 mW with 514.5 nm excitation wavelength. For comparison, all six spectra are staggered in the same diagram. The diagram indicates that 4-MPy adsorbed on ZnO nanoparticles 18.2 nm in size hardly enhances the SERS active modes of 4-MPy. The same is true for the sizes 23.8 nm and 25.2 nm; however, increasing intensities over all lines are shown toward 27.7-nm ZnO nanoparticles. At 27.7 nm, the highest intensities for all SERS active 4-MPymodes, compared to the other depicted samples, are observed. Since the image shows lower intensities toward 30.6 nm, a size-dependence enhancement resonance of SERS active 4-MPy modes is observed between ZnO nanoparticle sizes of 27.7 nm and 30.6 nm.

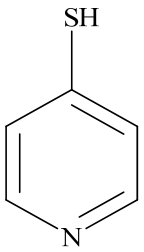

Figure 41: 4-mercaptopyridine (C_5H_5NS)

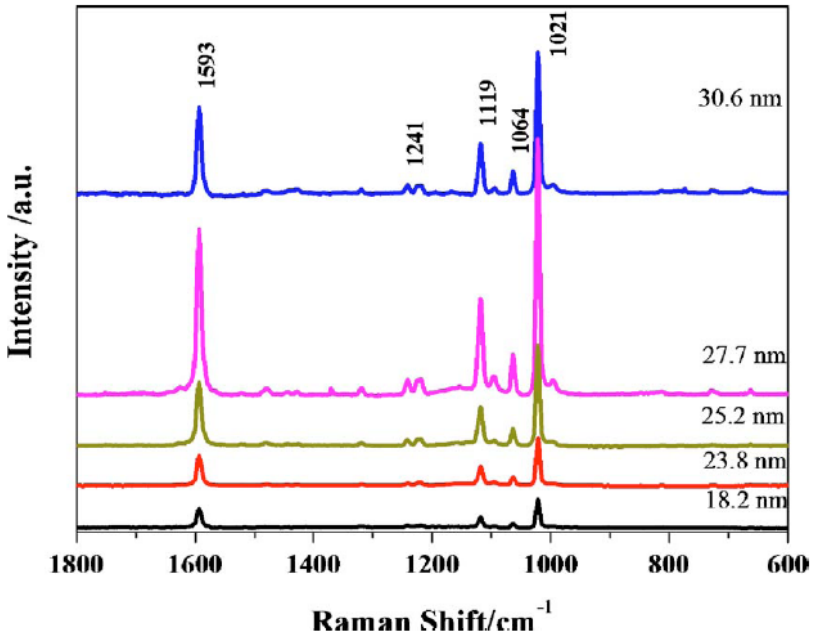

Figure 42: SERS spectra of 4-MPy adsorbed on ZnO nanoparticles with different sizes(3)

For detailed investigation of the relative enhancement of obtained Raman modes of 4-MPy adsorbed on different ZnO sizes, the line 1021cm^{-1} is investigated separately. Each sample is compared with the others. Figure 42 shows the excitation profile of the 1021cm^{-1} Raman mode of 4-MPy adsorbed on ZnO nanoparticles as a function of particle size. The relative enhancement is plotted on the y-axis. ZnO nanoparticles with sizes 18.2 nm, 23.8 nm, 25.2 nm, 27.7 nm, and 30.6 nm show different relative enhancements of the 1021cm^{-1} Raman mode of 4-MPy. ZnO nanoparticles sized 27.7 nm show the highest enhancement. A Gaussian fit to the data has a width of 4.4 nm and has its peak at 28.4 nm. The size-scanned resonance is interpreted as a charge-transfer resonance between the ZnO nanoparticles and the adsorbed 4-MPy molecule by Professor Bing Zhao's research group.(3)

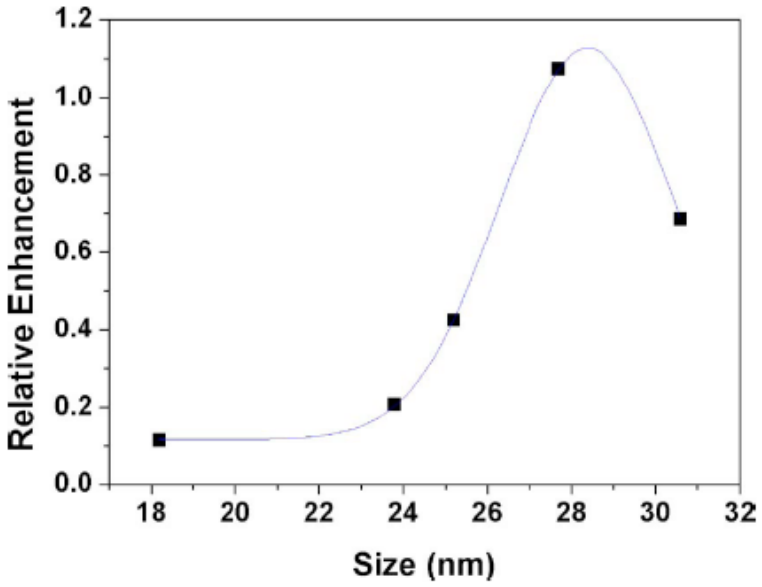

Figure 43: Raman relative intensity of the 1021cm^{-1} mode of 4-MPy adsorbed on ZnO nanoparticles as a function of particle size(3)

Summary:

- No $p_{CT}(\nu_i)$ values were calculated and compared, but relative enhancement of SERS active modes were compared
- The relative enhancement of SERS active modes of organic molecules like 4-MPy adsorbed on ZnO nanoparticles is ZnO size dependent.
- A ZnO nanoparticle size-dependent resonance of 4-MPy adsorbed on ZnO was measured at 27.7 nm. Resonance is expected to occur at 28.4 nm (calculated).
- The observed resonance at 27.7 nm is well above the excitation Bohr radius of ZnO.

3.4. ZnO Nanoparticles in Sandwich Structures

Surface plasmons enhance SERS active modes of the adsorbed molecule due to interaction of electromagnetic waves with the electrons in the valence bands in the metal used in the sample. The surface plasmons then induce vibration in the adjacent molecule. Hence, the effect itself is called electromagnetic (EM) effect, which occurs in metals only. The excited electrons can then be transferred to an adjacent free molecular level dependent on the excitation wavelength. This SERS enhancement contribution is called charge transfer. Electronic transitions from a filled adjacent molecular level to a metal or semiconductor band are also possible.

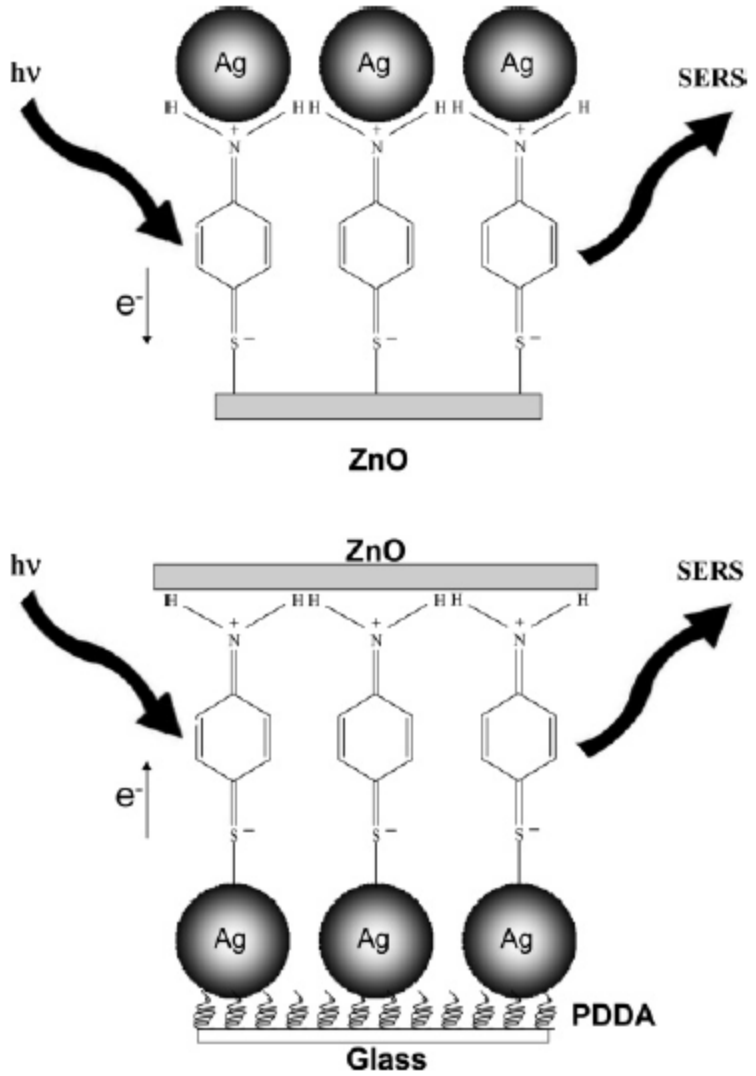

Figure 44: Sandwich structure of ZnO nanorods/PATP/Ag and Ag/PATP/ZnO nanorods(2 p. 5)

A thin film sandwich structure of ZnO nanorods, PATP, and Ag is shown in Figure 44. The thiol (–SH) group of PATP connects assumable to the first adjacent metal or semiconductor surface. In the first structure ZnO came in contact with PATP first, and in the second structure Ag came in contact with PATP first. The amino ($–NH_2$) group bonds to material added last.

Therefore, the PATP molecule adsorbs differently on the Ag nanoparticle and ZnO nanorod surfaces in the sandwich depicted in Figure 44. The first system shows PATP deposited on a ZnO thin film consisting of ZnO nanorods and Ag nanoparticles added at the end of the sample preparation. The second structure shows PATP deposited on an Ag nanoparticle film and ZnO nanorods added at the end of the sample preparation. The electromagnetic wave for excitation of electrons is illustrated as $h \times \nu$, and the scattered light from the sample is illustrated as SERS.

An SEM image of ZnO nanorods is depicted in Figure 45. The hexagonal ZnO nanorods have a diameter between 0.5 and 2 µm.

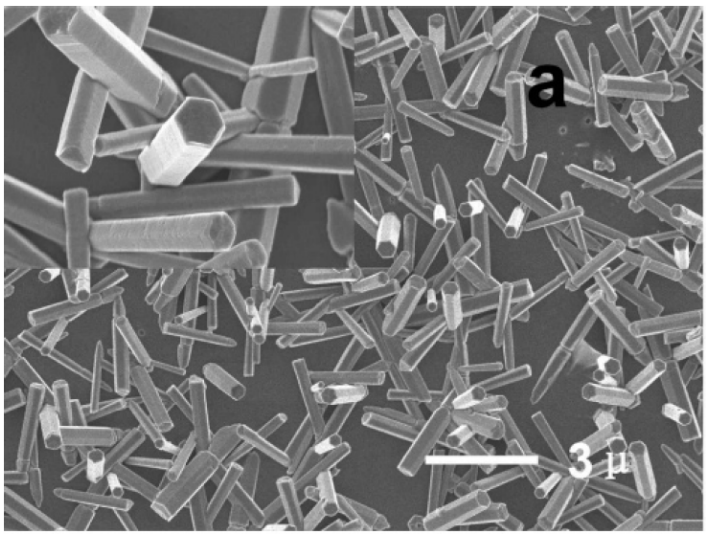

Figure 45: SEM images of ZnO nanorods

The charge-transfer electronic transition from the silver nanoparticles through the PATP molecule to the ZnO nanorods at 514.5 nm (2.4eV) excitation wavelength is shown in Figure 46.

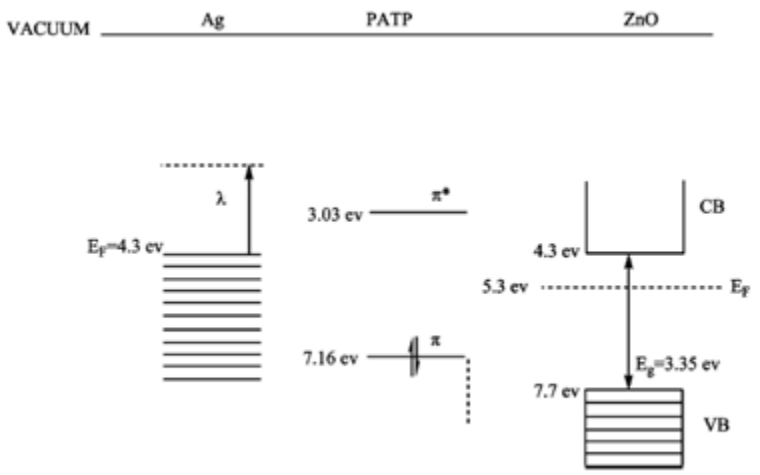

Figure 46: Energy-level diagram of the ZnO/PATP/Ag assembly measured from the vacuum level (modified)(2 p. 5)

The energy level diagram in Figure 46 shows the energy levels for Ag, PATP, and ZnO measured from the vacuum level. The monochromatic excitation beam at 514.5 nm excites electrons from the valence band of Ag by 2.4 eV to a higher level than that of the LUMO level (π*-orbital) of the PATP molecule. Next, charge transfer from Ag to the unfilled π*-orbital of the PATP molecule occurs, lowering the Fermi level of Ag. The electrons can relax further from the π*-orbital of the PATP molecule to the conduction band of the ZnO nanorods at 4.3 eV below the vacuum level. This transition increases the Fermi level at ZnO. The charge-transfer transition occurs until the Fermi levels at Ag and ZnO are at equilibrium, meaning that the rate of charge transfer in either direction is equal. At this point the SERS signal is stabilized. Figure 48 and Figure 47 show SERS spectra of PATP adsorbed in several different systems. All spectra show intensities in arbitrary units versus Raman shift in cm^{-1}. The spectra are not plotted to scale on the y-axis. Slight peak shifts from the original vibrational modes of the PATP molecules occur throughout all SERS spectra, since the molecular symmetry of the PATP molecules is lowered by the adsorption of PATP to the metal or semiconductor surface.

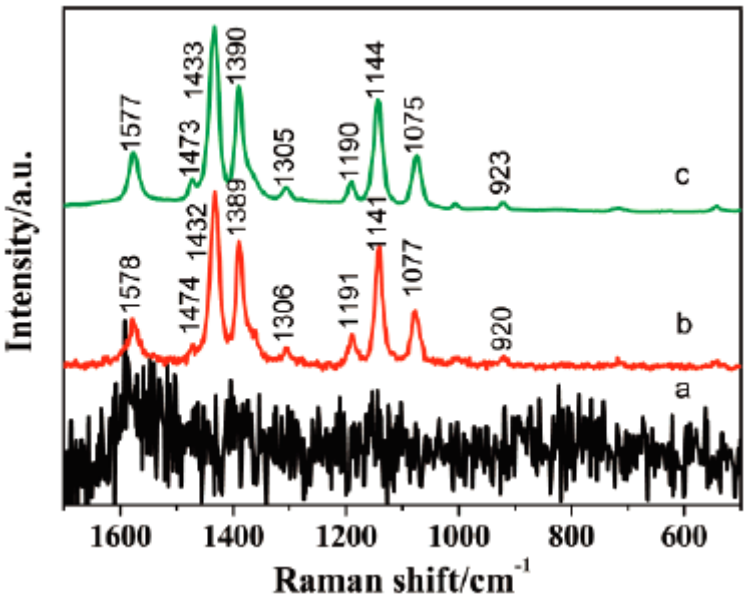

Figure 47: SERS spectra at 514.5 nm of (a) PATP adsorbed on ZnO nanorods, (b) PATP adsorbed on Ag nanoparticles, and (c) PATP adsorbed in the ZnO/PATP/Ag assembly(2 p. 3)

In Figure 47 the intensity in arbitrary units of SERS active modes of the PATP molecules in different structures is depicted as a function of Raman shift in cm^{-1}. The spectra were recorded at an excitation wavelength of 514.5 nm with 0.4 mW power. Spectrum (a) shows the SERS signal of PATP adsorbed on the surface of the ZnO nanoparticle, spectrum (b) shows PATP adsorbed on the surface of the Ag nanoparticles, and spectrum (c) shows PATP adsorbed in the ZnO/PATP/Ag assembly. Figure 47(a) indicates that almost no SERS activity occurs in the ZnO/PATP assembly, since semiconductors do not have surface plasmons. However, strongly enhanced SERS active PATP lines can be observed in the Ag/PATP assembly in Figure 47(b), and in the ZnO/PATP/Ag assembly depicted in (c). The peak centers in the structure ZnO/PATP/Ag are 1 to 3 cm^{-1} shifted from the peak positions marked in the Ag/PATP assembly; however, the spectra are governed by the same peaks. Therefore, no changes of the vibrational modes of PATP are observed.

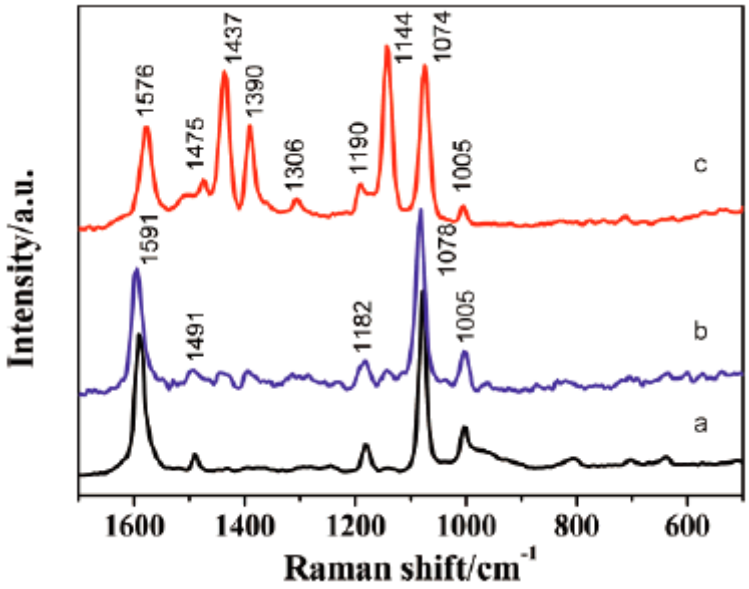

Figure 48: SERS spectra at 1064 nm of (a) PATP adsorbed on Ag nanoparticles, (b) PATP adsorbed in the Ag/PATP/ZnO assembly, and (c) PATP adsorbed in the ZnO/PATP/Ag assembly(2 p. 3)

In Figure 48 the intensity in arbitrary units of SERS active modes of the PATP molecules in different structures is depicted as a function of Raman shift in cm^{-1}. The spectra were recorded at an excitation wavelength of 1064 nm with 250 mW power. Spectrum (a) shows the SERS signal of PATP adsorbed on the surface of the Ag nanoparticle surface only, spectrum (b) shows PATP adsorbed in the Ag/PATP/ZnO assembly, and spectrum (c) shows PATP adsorbed in the ZnO/PATP/Ag structure. In spectrum (c), the b_2 modes at 1144, 1390, 1437, and 1576 are strongly enhanced due to charge transfer. Figure 48(a) indicates that only the totally symmetric lines of the PATP molecule at 1078 and 1591 are enhanced in the Ag/PATP assembly. The same is true for the assembly Ag/PATP/ZnO in (b). This is because in the assemblies Ag/PATP and Ag/PATP/ZnO either no or hardly any charge transfer occurs.

At 1064 nm excitation wavelength the b_2 modes are enhanced if in addition to surface plasmons, charge transfer occurs. In the three stated samples, this occurs only in the assembly ZnO/PATP/Ag. The a_1 lines are enhanced due to surface plasmons, as observed in the assemblies Ag/PATP and Ag/PATP/ZnO, which still show strong enhancement of a_1 lines according to Table 5. As depicted in Figure 44, the Ag nanoparticles can easily donate electrons in the ZnO/PATP/Ag assembly since the relatively electropositive part (NH_2) of the PATP molecule are attached to Ag nanoparticles. Also the S^- atom can easily forward electrons to Zn^{2+} in this structure. However, in the Ag/PATP/ZnO structure, it is more difficult for Ag nanoparticles to donate electrons to the LUMO of PATP, since PATP is attached with the S^- atom to the Ag surface. In addition, the relatively positive-charged amino (NH_2) group serves as a block against forwarding electrons to the O^{2-} in the ZnO nanoparticle.(2 p. 5)

Summary:

- Charge-transfer transitions are possible if the incoming photons in electron volts provide enough energy to excited electrons from a ground state to an adjacent unoccupied electronic or vibrational level at a metal, semiconductor, or molecule.
- At certain sample assemblies, charge-transfer transitions of electrons can be blocked by the relatively electropositive part ($–NH_2$) of the PATP molecule or the relatively electronegative thiol group (–SH) to transfer electrons through the molecule.
- SERS spectra of sandwich structures such as ZnO/PATP/Ag and Ag/PATP show strong enhancement of the SERS active modes of PATP molecules at the 514.5 nm excitation wavelength.
- Charge-transfer transitions enhance the non-totally symmetric b_2 modes at 1064 nm as seen in Figure 48(c) in the assembly ZnO/PATP/Ag. This was not observed in the sample structure Ag/PATP.
- PATP adsorbed only on ZnO nanorods gives low SNR ratios and therefore hardly analyzable SERS spectra.
- At 1064 nm surface plasmons enhance only totally symmetric modes, as seen in Figure 48(a) and (b) in the assemblies Ag/PATP and Ag/PATP/ZnO.

4. Experimental Section

Two studies were performed, the wavelength-dependence study and the size-dependence study of ZnO. In the wavelength-dependence study, the degree of $p_{CT}(\nu_9 b)$ (at 1142cm^{-1}) in the structures Ag/PATP/ZnO(27.7nm) and (27.7nm)ZnO/PATP/Ag were compared with the degree of $p_{CT}(\nu_9 b)$ obtained from the structure Ag/PATP at excitation wavelengths ranging from 476.5 nm to 676.4 nm. In the ZnO size-dependence study, six ZnO nanoparticle sizes were investigated on $p_{CT}(\nu_9 b)$ values in the structure Ag/PATP/ZnO (size varies). In addition, a multiple-run study at the same sample position showed the influence of applied laser time on the $p_{CT}(\nu_i)$ values.

4.1. Sample Preparation

Silver colloids were prepared according to the literature protocol.(25) Specifically, 90 mg of $AgNO_3$ was dissolved in 500 ml of distilled H_2O. Then it was heated to boiling temperature. At boiling temperature, 10 ml of 1% sodium citrate was added dropwise. The solution was kept boiling for about 1 h. After 1 h, the Ag colloid was brownish. The concentration of the Ag solution was 7 * 10^{-4} mol/l. Transmission electron microscopy (TEM) investigations show Ag spheres (80%) and rods (20%) as depicted in Figure 49. The mean diameter of the Ag spheres was 30 nm, while the average length of the rods was about 60 nm. Therefore, the approximate particle size by spheres is 35 nm. According to the Ag concentration of 7 * 10^{-4} mol/l, the silver particle density in solution was 3.2 * 10^{14} particles/l. The silver solution was prepared by Dr. J. Yang at the Department of Chemistry at the City College of New York (CCNY).

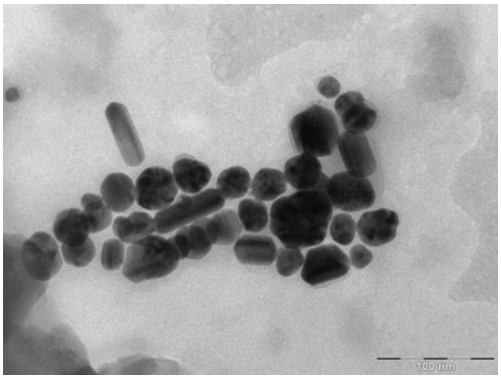

Figure 49: TEM image of Ag solution showing Ag spheres and nanorods (recorded by Dr. J. Yang at CCNY)

The ZnO nanoparticles were obtained from the State Key Laboratory of Supramolecular Structure and Materials, Jilin University, Changchun, People's Republic of China (Professor Bing Zhao). To obtain samples of various sized ZnO nanoparticles, the following

sample preparation was conducted.(26) To produce $Zn(OH)_2$, 40.0 ml of 0.5 mol/l NaOH solution was added dropwise to 100 ml of 0.1 mol/l $Zn(Ac)_2$ solution under vigorous stirring. Then, NH_4HCO_3 powder was added to the $Zn(OH)_2$ precipitate and stirred for 30 min. A zinc-carbonate hydroxide colloid was obtained. Next, the colloid was filtered with a G3 filter under reduced pressure and dried at 80 °C. As a result, the precursor of a small crystallite $Zn_5(CO_3)_2(OH)_6$ was formed. In the next step, the precursor was calcined at 350, 450, 550, 650, 750, and 850 °C for 2 h to obtain five sets of samples. These were washed and rinsed with deionized water and anhydrous alcohol and filtered with a G4 filter under reduced pressure three or four times. Finally, the products were dried at 70 °C. The ZnO nanoparticle sizes were estimated using the Scherrer formula. (27) ZnO nanoparticle sizes of 18.2 nm (350 °C), 23.8 nm (450 °C), 25.2 nm (550 °C), 27.7 nm (650 °C), 30.6 nm (750 °C), and 33.1 nm (850 °C) were obtained.

P-aminothiphenol (PATP) was obtained from Sigma-Aldrich Inc. Maryland / USA.
PAPT with a concentration of $1x10^{-2}$ mol/l in methanol solution was used for sample preparation.

Ag/PATP sample preparation. 2ml Ag solution ($7 * 10^{-4}$ mol/l) was mixed with 1 ml PATP ($1 x 10^{-2}$ mol/l), sonicated for 10 min and put aside for 24 h. The following day, the sample was rinsed with methanol and water. The sonication time at each rinsing run was 10 min. After rinsing the Ag/PATP sample, the solution was dried on a silicon wafer piece.

Ag/PATP/ZnO sample preparation. 2 ml Ag solution ($7 * 10^{-4}$ mol/l) and 1 ml PATP ($1 * 10^{-2}$ mol/L) were mixed and sonicated for 10 min, and put aside for 24 h. The following day the sample was rinsed with methanol and water. The sonication time at each rinsing run was 10 min. Then 2 mg ZnO nanoparticles were added. After the Ag/PATP/ZnO sample was sonicated for an additional 10 min, the excess water was removed and the sample dried on a silicon wafer piece (see Figure 50).

ZnO/PATP/Ag sample preparation. 2 mg ZnO nanoparticles and 1 ml PATP ($1 * 10^{-2}$ mol/L) were mixed and sonicated for 10 min, and put aside for 24 h. The following day, the sample was rinsed with methanol and water. The sonication time at each rinsing run was 10 min. Then 2 ml Ag solution ($7 * 10^{-4}$ mol/l) was added. After the Ag/PATP/ZnO sample was sonicated for an additional 10 min, the excess water was removed and the sample dried on a silicon wafer piece.

The three obtained sample structures are depicted in Figure 1 (see Chapter 1.2).

Figure 50: 1.5 ml centrifugal tube and Ag/PATP/ZnO on silicon wafer

Table 6 summarizes criteria that affect the SERS spectra and data analysis. Therefore, for the experiments all criteria were held constant.

Criterion	Comment
Sample preparation	- Position and connection of PATP to Ag and ZnO nanoparticles is not 100% clear or verified - Adsorption of PATP on metal or semiconductor lowers the symmetry of PATP and hence leads to peak shifts in the SERS spectra
Sonication time / Rinsing	- Higher sonication time can remove PATP adsorbed onto the metal surface - Sonication can lead to reorientation of the PATP molecule in the Ag/PATP/ZnO and ZnO/PATP/Ag samples - Sonication can break down the nanoparticles used into smaller sizes and hence change the size distribution
Laser power	- Higher laser power induces peak shifts in SERS spectra - Laser power has a strong effect on $p_{CT}(\nu_i)$, makes comparison between $p_{CT}(\nu_i)$ values recorded at different laser powers without a correction factor hardly possible - Laser power above approximately 15 mW can destroy the sample
Successive recordings at the same sample position with lowest possible laser power (Ag/PATP/ZnO)	- $p_{CT}(\nu_9 b)$ is hardly effected by multiple recordings at the same sample position (+/–5%) - $p_{CT}(\nu_3)$ and $p_{CT}(\nu_{19} b)$ are strongly affected by multiple recordings at the same sample position (change of more than 100%)
Laser power	- Increase in laser power can shift peak positions - Increase in laser power might alter $p_{CT}(\nu_i)$ values
Scanning time	- High scanning times can alter $p_{CT}(\nu_i)$ values
Laser/spectrometer system	- Difference in $p_{CT}(\nu_i)$) values observable

Table 6: Summary of criteria that affect the SERS spectra and data analysis

4.2. Excitation-Wavelength Dependence Study in Ag/PATP, Ag/PATP/ZnO, and ZnO/PATP/Ag

Ag/PATP, Ag/PATP/ZnO, and ZnO/PATP/Ag were investigated at the excitation wavelengths of 476.5 nm, 488.0 nm, 496.5 nm, and 514.5 nm, obtained from an Ar-ion laser, and at the excitation wavelength of 676.4 nm, obtained from a Kr-ion laser. Both lasers used are Spectra Physics Beam Lok 2020 lasers. To enable comparisons of the obtained $p_{CT}(\nu_9 b)$ values, all settings, including the laser power, were held constant. All spectra were recorded at 10 mW at each excitation wavelength. The recorded range was from 900 to 1700 cm^{-1} Raman shift with a resolution of 6 cm^{-1}. For a spectrometer, a Spex Model 1401 double monochromator with photon count with a recording pace of 50 cm^{-1}/min was used. The wavelength-dependent color code was held constant for all three samples. Violet spectra pertain to the excitation wavelength 476.5 nm, dark blue to 488.0 nm, turquoise to 496.5 nm, green to 514.5 nm, and red to 676.4 nm. The degree of charge transfer ($p_{CT}(\nu_i)$) of the main vibrational modes 1573 ν8b b2, 1440 ν19b b2, 1391 ν_3 b_2, and 1142 ν_9b b2 with respect to 1077 ν_7a a_1 was calculated. A baseline correction was conducted for $p_{CT}(\nu_i)$ value calculations at each spectra as depicted in Figure 54. Through Gaussian fitting, the area below the main vibrational modes was obtained. The $p_{CT}(\nu_i)$ values were calculated as shown in the section calculation.(1) Finally, the $p_{CT}(\nu_i)$ values of each sample were plotted versus excitation wavelength and compared with one another.

Figure 51 shows the wavelength-dependence study of the Ag/PATP sample as a function of Raman shift in cm^{-1}. The sample was investigated at 476.5 nm, 488.0 nm, 496.0 nm, and 514.5 nm excitation wavelengths. Figure 52 shows the wavelength-dependence study of the Ag/PATP/ZnO(27.7nm) sample as a function of Raman shift in cm^{-1}, and Figure 53 shows the wavelength-dependence study of the (27.7nm)ZnO/PATP/Ag sample. The samples Ag/PATP/ZnO(27.7nm) and (27.7nm)ZnO/PATP/Ag were investigated with the additional excitation wavelength 676.4 nm. The obtained spectra from all three samples show the same patterns. No significant peak shifts were observed among the spectra obtained at different excitation wavelengths for each sample. Peak shifts of the main modes 1573 $\nu_8 b_2$, 1440 ν_{19}b b_2, 1391 ν_3 b_2, 1142 ν_9b b_2, and 1077 ν_7a a_1 to the assigned peak position in literature protocol (24) were observed; however, the peak shifts are in the expected range of +/–6 wavenumbers. Ratios of non-totally symmetric b_2 modes to totally symmetric a_1 modes are strongly affected by the excitation wavelength. This ratio has a direct effect on the calculated $p_{CT}(\nu_i)$ values.

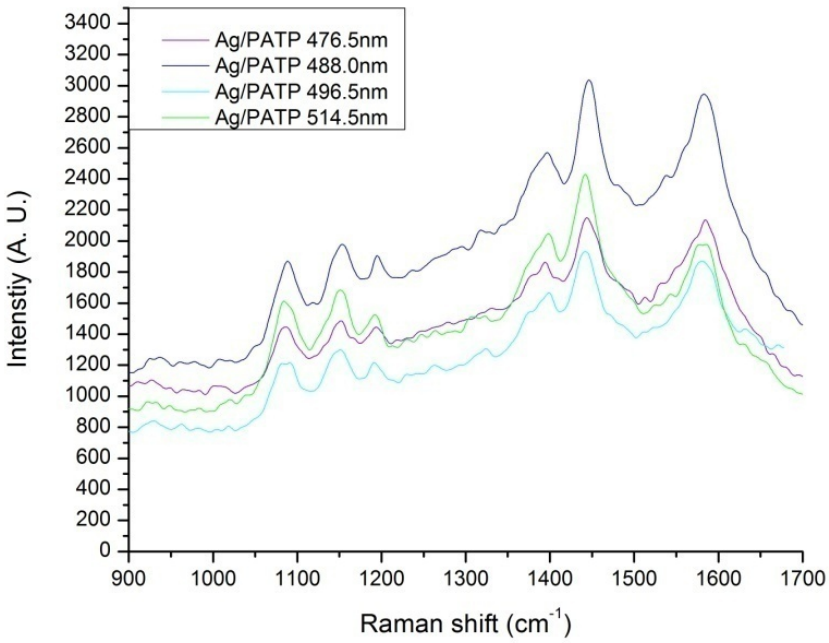

Figure 51: Ag/PATP wavelength-dependence study between 476.5 nm and 514.5 nm

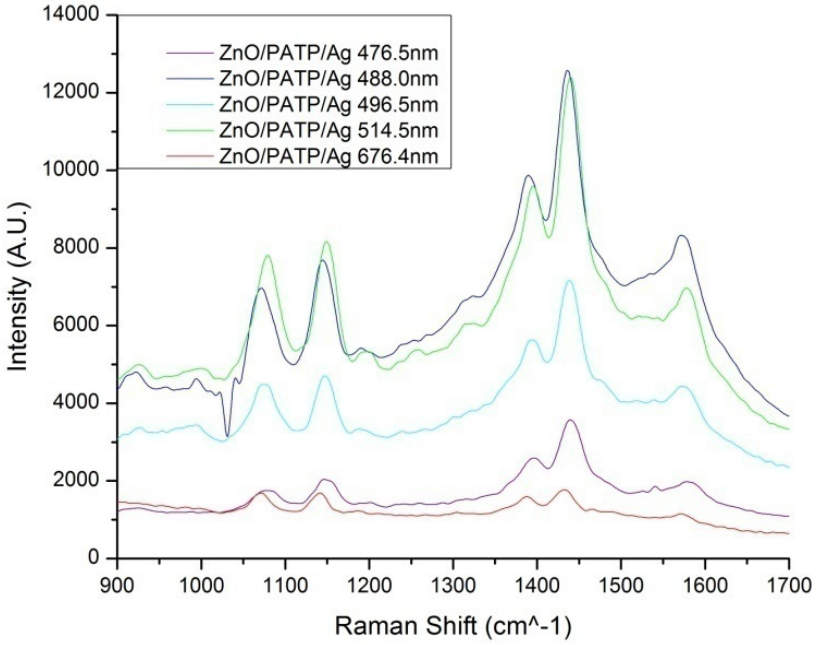

Figure 52: ZnO/PATP/Ag wavelength-dependence study between 476.5 nm and 676.4 nm

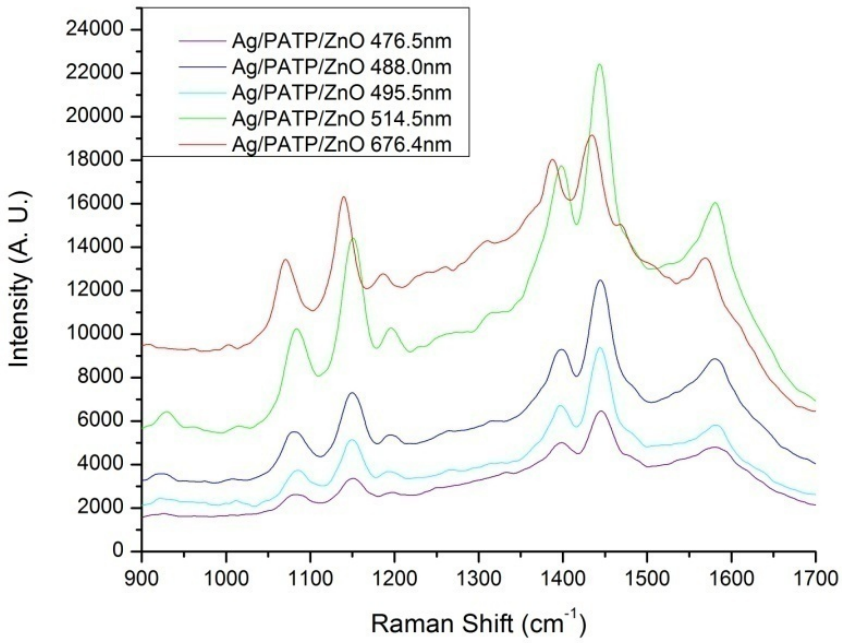

Figure 53: Ag/PATP/ZnO wavelength-dependence study between 476.5 nm and 676.4 nm

The area below the investigated modes of baseline-corrected spectra was used for degree of $p_{CT}(\nu_i)$ calculations. Baseline correction was performed in OriginlLab8.0 according to Figure 54, which shows an example of a baseline-corrected spectrum. The spectrum obtained at 514.5 nm excitation wavelength of the sample ZnO/PATP/Ag is shown. For comparison, the baseline anchor points were set constant in x-direction at each spectrum for all three investigated samples pertaining to each excitation wavelength. At each excitation wavelength, the baseline was adapted slightly to the occurring background patterns. Baseline-corrected spectra show the same pattern for all three investigated samples, but the peak intensities, as well as the b_2/a_1 mode ratios and therefore the $p_{CT}(\nu_i)$ values, vary significantly. In addition, Figure 54 shows one a_1 mode and four b_2 modes labeled. All calculations refer to these five modes.

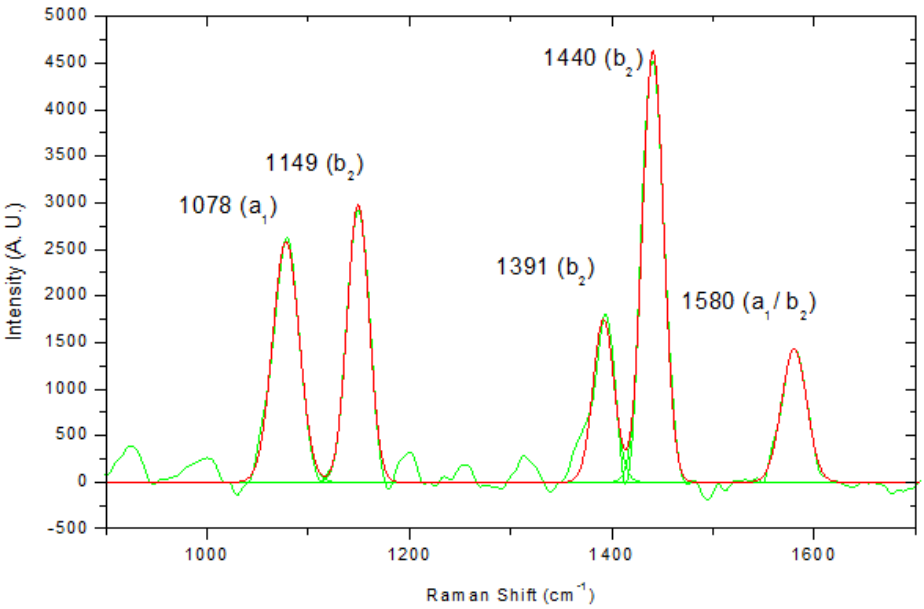

Figure 54: Baseline-corrected spectrum of the sample ZnO/PATP/Ag recorded at 514.5 nm

Peak shifts compared to the assigned peaks of PATP in literature protocol are observed (Table 5); however, all four strong b_2 modes correspond to the main modes in the benzene ring. At the samples Ag/PATP/ZnO(27.7nm) and Ag/PATP, peak shifts up to 5 cm^{-1} are observed. The spectra of the sample (27.7nm)ZnO/PATP/Ag show peaks at different positions at each excitation wavelength. In addition the spectra show peak shifts to the assigned peaks of PATP in literature protocol. Table 7, Table 8, and Table 9 summarize results obtained from baseline-corrected spectra of the samples Ag/PATP, Ag/PATP/ZnO(27.7nm), and (27.7nm)ZnO/PATP/Ag at wavelengths 476.5 nm, 488 nm, 496.5 nm, 514.5 nm, and 676.4 nm. A Gaussian fit to each vibrational mode of baseline-corrected spectra was performed. The area below the Gaussian curve, as well as at the peak center, was calculated. The ratio of the area $b_{(i)}/a_1$ at each wavelength and the $p_{CT}(\nu_i)$ values are given in the last two columns.

Wave-length [nm]	PATP Mode	Area (below peak) [A. U.]	Peak center [cm^{-1}]	Ratio [R] = $b_{(i)}/a_1$	$p_{CT}(\nu_i)$ = [R / (R+1)]
476.5	ν_7a	8003	1084	1.00	-
476.5	ν_9b	4466	1149	0.56	0.36
476.5	ν_3	5280	1387	0.66	0.40
476.5	ν_{19}b	10603	1445	1.32	0.57
476.5	ν_8b	32240	1580	4.03	0.80
488.0	ν_7a	11402	1086	1.00	-
488.0	ν_9b	7539	1151	0.66	0.40
488.0	ν_3	9519	1388	0.83	0.46
488.0	ν_{19}b	17112	1446	1.50	0.60
488.0	ν_8b	42726	1581	3.75	0.79
496.5	ν_7a	8605	1084	1.00	-
496.5	ν_9b	6186	1148	0.72	0.42
496.5	ν_3	6104	1388	0.71	0.42
496.5	ν_{19}b	10882	1442	1.26	0.56
496.5	ν_8b	21452	1579	2.49	0.71
514.5	ν_7a	13262	1085	1.00	-
514.5	ν_9b	8767	1149	0.66	0.40
514.5	ν_3	8956	1387	0.68	0.40
514.5	ν_{19}b	15779	1442	1.19	0.54
514.5	ν_8b	27067	1580	2.04	0.67

Table 7: $p_{CT}(\nu i)$ values in the sample Ag/PATP at four different excitation wavelengths

Wave-length [nm]	PATP Mode	Area (below peak) [A. U.]	Peak center [cm^{-1}]	Ratio [R] = $b_{(i)}/a_1$	$p_{CT}(\nu_i)$ = [R / (R+1)]
476.5	ν_7a	17886	1082	1.00	-
476.5	ν_9b	29290	1150	1.64	0.62
476.5	ν_3	20439	1395	1.14	0.53
476.5	ν_{19}b	53273	1446	2.98	0.75
476.5	ν_8b	61364	1576	3.43	0.77
488.0	ν_7a	49735	1080	1.00	-
488.0	ν_9b	78537	1149	1.58	0.61
488.0	ν_3	46999	1395	0.94	0.49
488.0	ν_{19}b	119049	1445	2.39	0.71
488.0	ν_8b	118213	1577	2.38	0.70
496.5	ν_7a	31674	1083	1.00	-
496.5	ν_9b	54626	1149	1.72	0.63
496.5	ν_3	35299	1394	1.11	0.53
496.5	ν_{19}b	94382	1444	2.98	0.75
496.5	ν_8b	71866	1578	2.27	0.69
514.5	ν_7a	80098	1083	1.00	-
514.5	ν_9b	155015	1150	1.94	0.66
514.5	ν_3	99795	1394	1.25	0.55
514.5	ν_{19}b	200131	1444	2.50	0.71
514.5	ν_8b	198410	1578	2.48	0.71
676.4	ν_7a	17886	1082	1.00	-
676.4	ν_9b	29290	1150	1.64	0.62
676.4	ν_3	20439	1395	1.14	0.53
676.4	ν_{19}b	53273	1446	2.98	0.75
676.4	ν_8b	61364	1576	3.43	0.77

Table 8: $p_{CT}(\nu_i)$ values in the sample Ag/PATP/ZnO(27.7nm) at five different excitation wavelengths

Wave-length [nm]	PATP Mode	Area (below peak) [A. U.]	Peak center [cm^{-1}]	Ratio [R] = $b_{(i)}/a_1$	$p_{CT}(\nu_i)$ = [R / (R+1)]
476.5	ν_7a	14076	1077	1.00	-
476.5	ν_9b	18219	1149	1.29	0.56
476.5	ν_3	11629	1391	0.83	0.45
476.5	ν_{19}b	38460	1441	2.73	0.73
476.5	ν_8b	13141	1583	0.93	0.48
488.0	ν_7a	67265	1072	1.00	-
488.0	ν_9b	74487	1145	1.11	0.53
488.0	ν_3	44431	1387	0.66	0.40
488.0	ν_{19}b	114205	1437	1.70	0.63
488.0	ν_8b	48000	1578	0.71	0.42
496.5	ν_7a	40301	1075	1.00	-
496.5	ν_9b	39138	1148	0.97	0.49
496.5	ν_3	22428	1390	0.56	0.36
496.5	ν_{19}b	61958	1439	1.54	0.61
496.5	ν_8b	23959	1578	0.59	0.37
514.5	ν_7a	84344	1078	1.00	-
514.5	ν_9b	80109	1149	0.95	0.49
514.5	ν_3	45204	1392	0.54	0.35
514.5	ν_{19}b	121125	1441	1.44	0.59
514.5	ν_8b	44381	1580	0.53	0.34
676.4	ν_7a	14036	1070	1.00	-
676.4	ν_9b	11324	1140	0.81	0.45
676.4	ν_3	6764	1385	0.48	0.33
676.4	ν_{19}b	11993	1433	0.85	0.46
676.4	ν_8b	3818	1574	0.27	0.21

Table 9: $p_{CT}(\nu_i)$ values in the sample (27.7nm)ZnO/PATP/Ag at five different excitation wavelengths

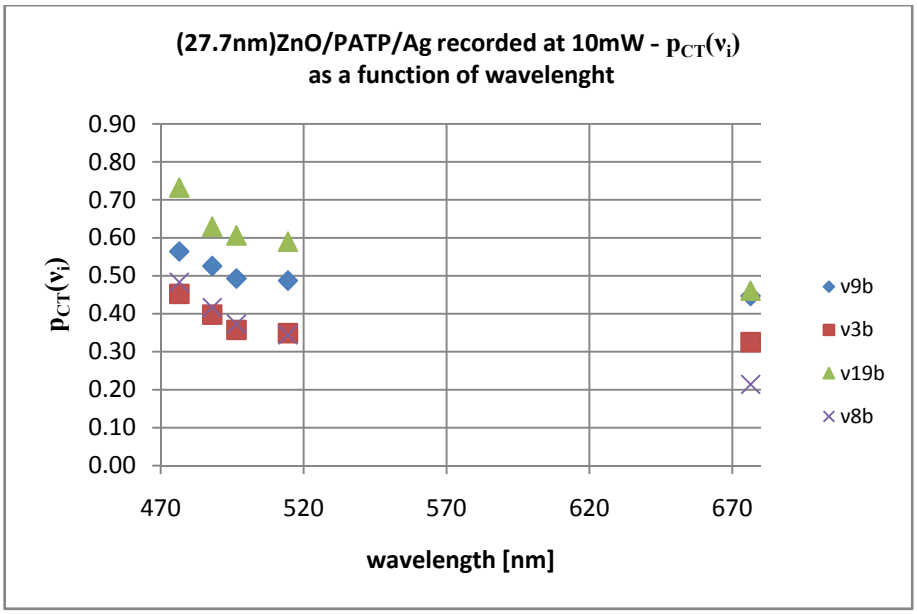

Figure 55: Wavelength-dependence study, peak ratios $b_{(i)}/a_{1,1}$ as a function of wavelength of (27.7nm)ZnO/PATP/Ag

Figure 55 shows the excitation-wavelength dependence study of (27.7nm)ZnO/PATP/Ag. The degrees of charge transfer at 1142 cm^{-1} $p_{CT}(\nu_9b)$, 1391 cm^{-1} $p_{CT}(\nu_3)$, 1440 cm^{-1} $p_{CT}(\nu_{19}b)$, and $p_{CT}(\nu_8b)$ are plotted versus excitation wavelength. At 676.4 nm, the lowest $p_{CT}(\nu_i)$ values are obtained. Toward 476.5 nm, all $p_{CT}(\nu_i)$ values increase, indicating that an excitation-dependent resonance is most likely to occur below 476.4 nm wavelength. Although all four lines show the same pattern, for comparison with the Ag/PATP and Ag/PATP/ZnO, only the $p_{CT}(\nu_9b)$ values are considered. The $p_{CT}(\nu_3)$ values are discussed, but the accuracy of these values is not as high as the accuracy of $p_{CT}(\nu_9b)$ values. The $p_{CT}(\nu_8b)$ values are strongly baseline dependent, which makes comparison studies of this value at different excitation wavelengths hardly possible. This is because calculations of $p_{CT}(\nu_i)$ values are strongly dependent on where the anchor points of the baseline are set. In addition, a multiple-run study on the same sample spot discussed in the ZnO size-dependence study shows that the values $p_{CT}(\nu_3)$, $p_{CT}(\nu_{19}b)$, and $p_{CT}(\nu_8b)$ are strongly dependent on the laser scanning time. For the $p_{CT}(\nu_9b)$ values, the influence of the performed baseline correction as well as the influence of the laser scanning time are the smallest out of all $p_{CT}(\nu_i)$ values. The $p_{CT}(\nu_9b)$ values of all three sample structures are summarized in Table 10.

Wavelength [nm]	Ag/PATP	Ag/PATP/ZnO	ZnO/PATP/Ag
476.5	0.36	0.62	0.56
488.0	0.40	0.61	0.53
496.5	0.42	0.63	0.49
514.5	0.40	0.66	0.49
676.4	-	0.62	0.45

Table 10: $p_{CT}(\nu_9b)$ values of the samples Ag/PATP, Ag/PATP/ZnO(27.7nm), and (27.7nm)ZnO/PATP/Ag at excitation wavelengths from 476.5 nm to 676.4 nm

4.3. ZnO Size-Dependence Study in Ag/PATP/ZnO

Ag/PATP/ZnO assemblies with ZnO sizes 18.2 nm, 23.8 nm, 25.2 nm, 27.7 nm, 30.6 nm, and 33.1 nm were investigated on the degree of charge transfer ($p_{CT}(\nu_9 b)$) to find a size-dependent resonance region. The spectra of all six samples were recorded at the wavelengths 488 nm, 633 nm, 785 nm, and 1064 nm. The laser settings are summarized in Table 11. The reported range of interest in cm^{-1} is from 900 to 1700.

For the laser line 1064 nm, an FT-IR microspectrometer and a 40x objective was used. In the dispersive Raman systems a 100x objective was used. All spectra of the size-dependence study were recorded at the lowest possible laser power at each excitation wavelength. Since compared with the wavelength-dependence study different laser systems and setups were used, and spectra were recorded with different laser powers, the obtained $p_{CT}(\nu_9 b)$ values from the size-dependence study are not directly comparable with the $p_{CT}(\nu_9 b)$ values obtained in the wavelength-dependence study. For comparisons of $p_{CT}(\nu_i)$ values, only the $p_{CT}(\nu_9 b)$ values are considered. The $p_{CT}(\nu_3)$ values are discussed, but the accuracy of these values is not as high as the accuracy of $p_{CT}(\nu_9 b)$ values. The $p_{CT}(\nu_8 b)$ values are strongly baseline-correction dependent, which makes comparison studies of this value at different excitation wavelengths or ZnO particles sizes hardly possible.

Excitation wavelength [nm]	Laser	Power [mW]	Resolution [cm^{-1}]	Recorded range [cm^{-1}]	Aperture	Detector	Scanning Time [s] or runs	Raman type	Comment
488	Bruker: Senterra Raman-micros.	0.25	3-5	50-1880	50x 1000µm	CCD	30	dispers.	1200 rulings/mm holographic grating
633	Bruker: Senterra Raman-micros.	0.20	3-5	400-1800	50x 1000µm	CCD	30	dispers.	1200rulings/ mm holographic grating
785	Bruker: Senterra Raman-micros.	1.00	3-5	420-1780	50x 1000µm	CCD	30	dispers.	1200rulings/ mm holographic grating
1064	Bruker: Ram II FT-Raman-Vertex70, Nd: YAG	5.00	3-5	200-2000	5mm	liquid N2-cooled Ge-detector	64 runs	FT	Beamspl. CaF_2, scanning velocity 5KHz

Table 11: Laser settings at the ZnO size-dependence study in the sample structure Ag/PATP/ZnO

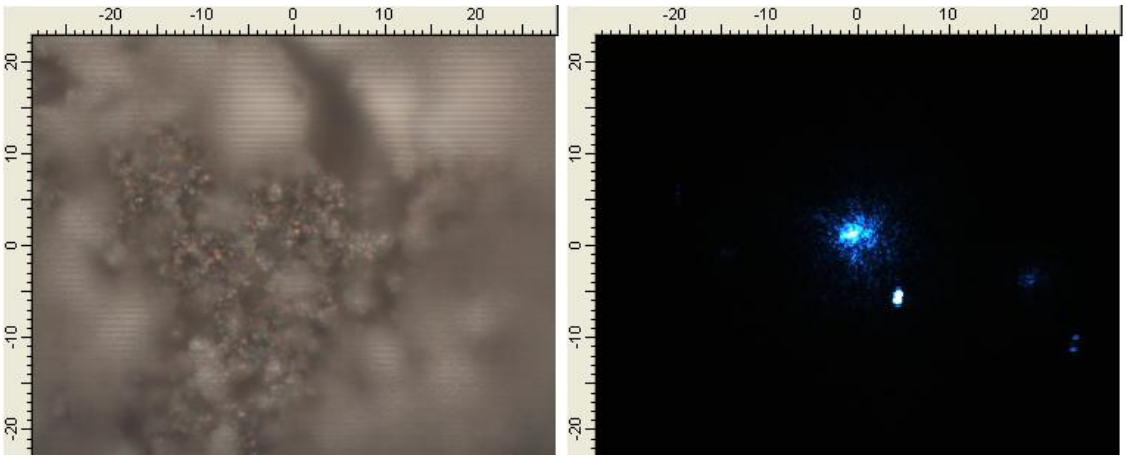

a) b)

Figure 56: Ag/PATP/ZnO(27.7nm) sample spot a) 100x magnification with a confocal microscope; b) scattered light at 488 nm excitation wavelength

The Bruker Senterra Ramanmicroscope and the Bruker Ram II FT-Raman-Vertex 70 systems allow users to focus exactly on a chosen spot on the sample. A confocal microscope allows minimizing the layer depth for investigation. A 100x magnification of an Ag/PATP/ZnO(27.7nm) sample and the pattern of the scattered light during the application of a 488 nm excitation wavelength are depicted in Figure 56. The blurred region in Figure 56(a) indicates areas outside the layer depth of the confocal microscope. Figure 56(b) shows the pattern of scattered light obtained in a 180° arrangement. By choosing proper sample spots for spectra recording it was possible to increase the quality of SERS spectra and to minimize error bars.

A multiple-run study was performed at the same sample position to investigate the stability of $p_{CT}(\nu_i)$ values. Three successive recorded spectra at the same spot on the Ag/PATP/ZnO(33.1nm) sample are shown in Figure 57. The spectra were recorded at 785 nm excitation wavelength at 1.0 mW with an accumulation time of 30 sec. Therefore, the laser was applied for 30 sec on the sample after the first run, 60 sec after the second run, and 90 sec after the third run. While $p_{CT}(\nu_9 b)$ was stable over three runs (+/–3%), $p_{CT}(\nu_3)$ experienced more than a 700% increase and $p_{CT}(\nu_{19} b)$ experienced more than a 200% increase. The high percentages are obtained because both modes $\nu_3\, b_2$ and $\nu_{19} b\, b_2$ were hardly developed after the first run (see Table 12), but developed to real peaks during the second and third runs. The $p_{CT}(\nu_8 b)$ values show instability as well. The study shows that the length of time a laser is applied on a sample effects the enhancement of certain b_2 modes in SERS significantly. Since $p_{CT}(\nu_9 b)$ values are the most stable ones, these values are used for comparisons between different samples.

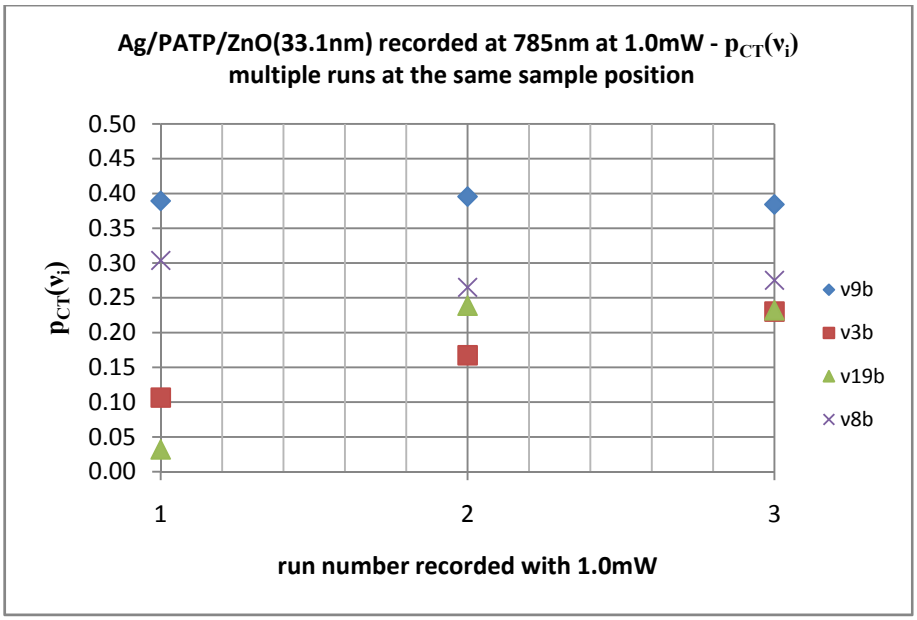

Figure 57: Ag/PATP/ZnO(33.1nm) multiple-run study at 785 nm with 1mW at the same spot; $p_{CT}(\nu_i)$ values as a function of runs

run	ν_9b	ν_3	ν_{19}b	ν_8b
1	0.39	0.11	0.03	0.30
2	0.40	0.17	0.24	0.27
3	0.38	0.23	0.23	0.28

Table 12: $p_{CT}(\nu_i)$ values of the multiple-run study depicted in Figure 57

The ZnO size-dependence study in the sample Ag/PATP/ZnO was performed to find a size-dependent resonance. In addition, the six samples Ag/PATP/ZnO with ZnO sizes 18.2 nm, 23.8 nm, 25.2 nm, 27.7 nm, 30.6 nm, and 33.1 nm were investigated at four different excitation wavelengths to show how the degree of CT is influenced by different excitation wavelengths. The color code in all reported spectra for each ZnO size is black for 18.2 nm, red for 23.8 nm, green for 25.2 nm, dark blue for 27.7 nm, violet for 30.6 nm, and brown for 33.1 nm. It was decided to record all spectra at the lowest possible laser power at each excitation wavelength. By doing this, the sample distortion was minimized, as was SERS spectra distortion due to laser heat. To enable comparisons of the obtained $p_{CT}(\nu_9 b)$ values at each excitation wavelength, all settings including the laser power were held constant. However, since it was decided to record the spectra at minimum power at each line, the power was adapted from one excitation wavelength to the next. Therefore, this has to be taken into account if direct comparisons of ($p_{CT}(\nu_i)$) values among different excitation-wavelengths are conducted.

The degree of charge transfer ($p_{CT}(\nu_i)$) of the main vibrational modes 1573 $\nu_8 b\, b_2$, 1440 $\nu_{19} b\, b_2$, 1391 $\nu_3\, b_2$, and 1142 $\nu_9 b\, b_2$, with respect to 1077 $\nu_7 a\, a_1$ was calculated. For $p_{CT}(\nu_i)$ value calculations, a baseline correction was conducted at each spectrum as depicted in Figure 54. Through Gaussian fitting the area below the main vibrational modes was obtained. The $p_{CT}(\nu_i)$ values were calculated as shown in Chapter 3.1. Finally, the $p_{CT}(\nu_i)$ values of each sample were

plotted versus ZnO nanoparticle size at each excitation wavelength and compared with one another.

Figure 58 shows the size-dependence study of the six Ag/PATP/ZnO samples as a function of Raman shift in cm^{-1} at 488 nm, Figure 59 at 633 nm, Figure 60 at 785, and Figure 61 at 1064 excitation wavelength. Each shown spectrum is in its original form as recorded. In Figure 58, the main vibrational modes 1078 ν_7a a_1, 1144 ν_9b b_2, 1391 ν_3 b_2, 1437 ν_{19}b b_2, and 1576 ν_8b b2 are labeled. The obtained spectra from all six samples show the same patterns at each excitation wavelength. No significant peak shifts were observed among the spectra recorded at different excitation wavelengths for each sample. Peak shifts of the main modes 1078 ν_7a_1, 1144 ν_9b b_2, 1391 ν_3 b_2, 1437 ν_{19}b b_2, and 1576 ν_8b b_2 to the assigned peak position in literature protocol summarized in Table 5 (24) were observed; however, the peak shifts are in the expected range of +4/–0 wavenumbers. Ratios of non-totally symmetric b_2 modes to totally symmetric a_1 modes are strongly affected by the ZnO particle size and excitation wavelength. This ratio has a direct effect on the calculated $p_{CT}(\nu_i)$ values.

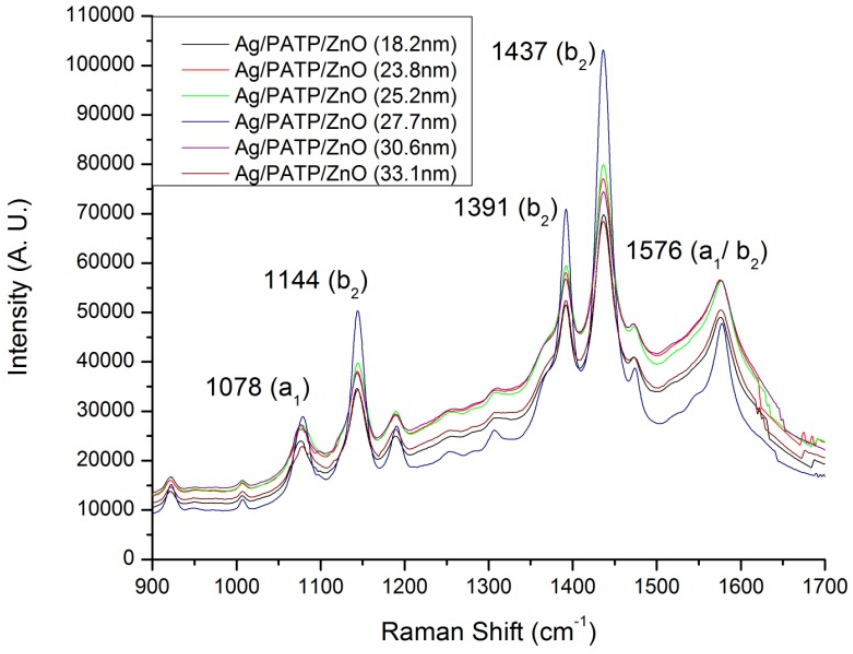

Figure 58: ZnO size-dependence study at 488 nm excitation wavelength

All six samples in the size-dependence study show strong fingerprint spectra recorded with 0.25 mW at 488 nm excitation wavelengths as depicted in Figure 58. It can be seen that the peaks of the spectrum in dark blue, which was obtained from the sample Ag/PATP/ZnO(27.7nm), show the strongest enhancement of all lines.

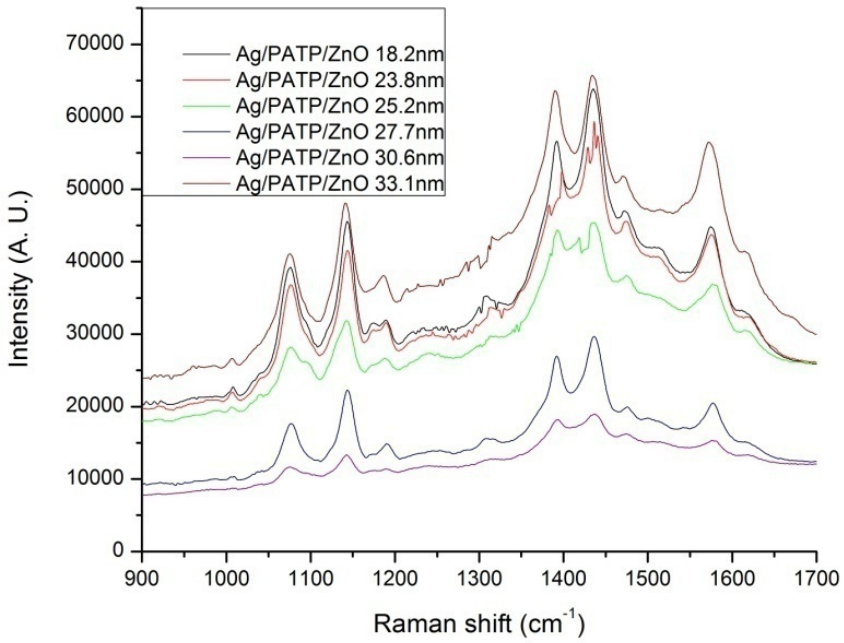

Figure 59: ZnO size-dependence study at 633 nm excitation wavelength

At 633 nm excitation wavelength, as depicted in Figure 59, it can be seen that the signal-to-noise ratio has decrease compared to the obtained spectra at 488 nm. The peaks 1078 ν_7a a_1 and 1144 ν_9b b_2 are still very detailed. The obtained spectra were recorded at 0.2 mW.

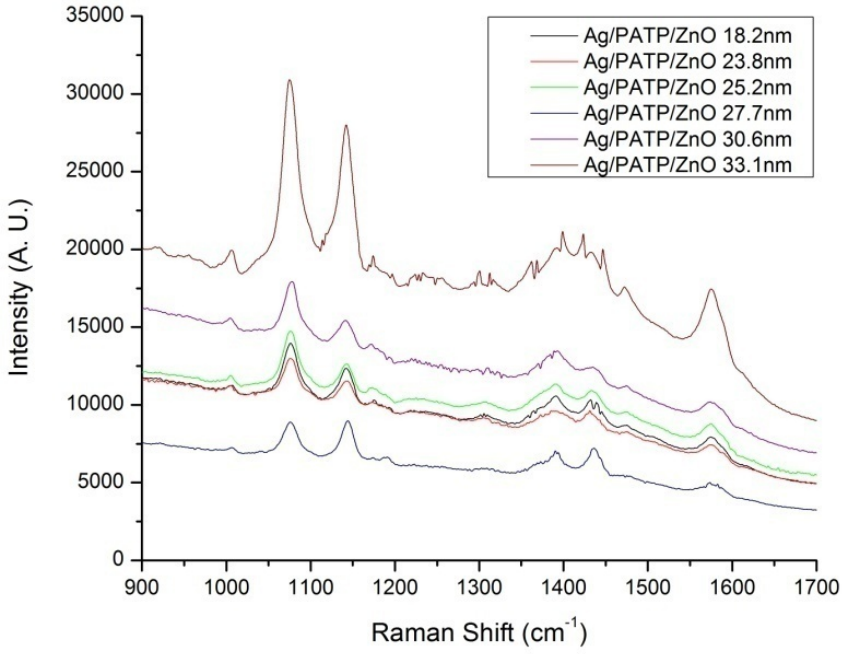

Figure 60: ZnO size-dependence study at 785 nm excitation wavelength

The spectra of the size-dependence study recorded with 1.0 mW at 785 nm excitation wavelength are depicted in Figure 59. The spectra show that the peaks at 1391 $\nu_3\, b_2$ and 1437 $\nu_{19}b\, b_2$ can hardly be used for $p_{CT}(\nu_i)$ calculations. However, as shown in the multiple-run study, if the laser scanning time is increased the peaks $\nu_3\ b_2$ and $\nu_{19}b\ b_2$ will develop to more sophisticated peaks, giving higher $p_{CT}(\nu_i)$ values.

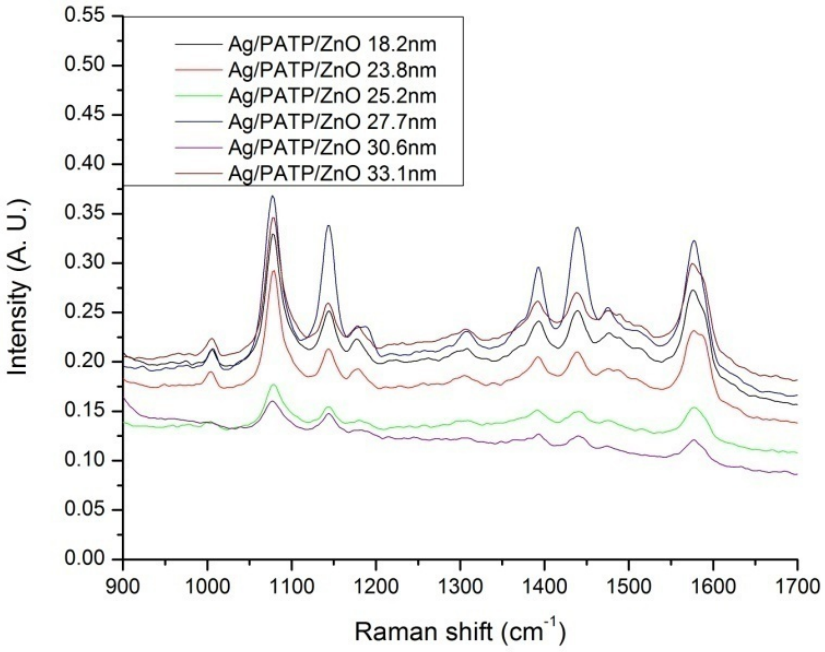

Figure 61: ZnO size-dependence study at 1064 nm excitation wavelength

All spectra recorded with 4.0 mW at 1064 nm excitation wavelength show low intensities. In each spectrum, the b_2 lines are strongly reduced, giving low $p_{CT}(\nu_i)$ values. The sample Ag/PATP/ZnO(27.7nm) peaks out in the ZnO size-dependence study. As depicted in Figure 61, Ag/PATP/ZnO(27.7nm) gives much higher relative enhancements of the b_2 lines ν_9b, ν_3, and $\nu_{19}b$ with respect to the a_1 line $\nu_7a\ a_1$ than any other sample. Different from the $p_{CT}(\nu_i)$ values obtained at the excitation wavelengths 488 nm, 633 nm, and 785 nm, in which the area in arbitrary units below each peak was used for calculations, at excitation wavelength 1064 nm the peak heights in arbitrary units were used.

Figure 63 shows the size-dependence study of the Ag/PATP/ZnO samples as a function of ZnO nanoparticle size in nm at 488 nm excitation wavelength. This figure depicts ZnO nanoparticle sizes from 18.2 nm to 33.1 nm on the x-axis and the calculated $p_{CT}(\nu_i)$ values of b_2 lines on the y-axis. It was observed that ZnO sizes with 27.7 nm give the highest $p_{CT}(\nu_i)$ values for all three b_2 lines ($\nu_9b\, b_2$, $\nu_3\, b_2$, and $\nu_{19}b\, b_2$). Although the 25.2 nm and 23.8 nm samples show decreasing $p_{CT}(\nu_i)$ values, sample 18.2 nm again shows an increase of $p_{CT}(\nu_i)$ values.

Since all obtained $p_{CT}(\nu_i)$ values are well above 0.5, the spectra are ruled by CT. Table 13 shows the detailed data to Figure 61. Table 14, Table 15, Table 16, and Table 17 show the data obtained in the peak analysis of baseline-corrected spectra at the excitation wavelengths

488 nm, 633 nm, 785 nm, and 1064 nm in the ZnO size-dependence study. The tables show the calculated areas below baseline-corrected peaks, the peak centers, the peak ratios $b_{(i)}/a_1$, and the $p_{CT}(\nu_i)$ values for each ZnO particle size.

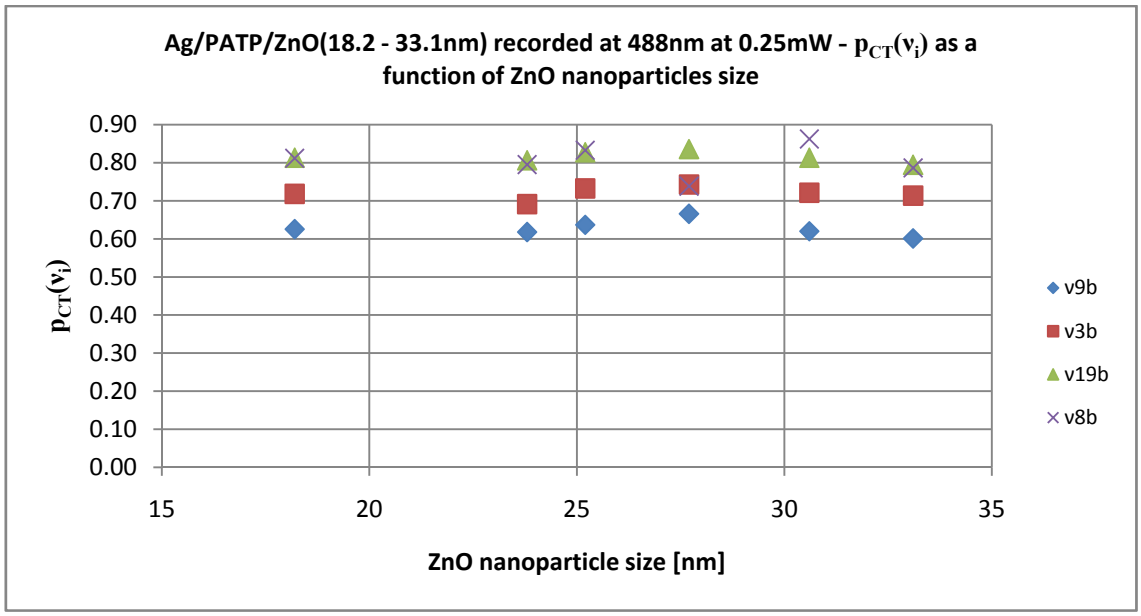

Figure 62: Ag/PATP/ZnO at 488 nm, $p_{CT}(\nu_i)$ values as a function of ZnO nanoparticle size

ZnO nanoparticle size [nm]	ν_9b	ν_3	ν_{19}b	ν_8b
18.2	0.63	0.72	0.81	0.81
23.8	0.62	0.69	0.81	0.80
25.2	0.64	0.73	0.83	0.83
27.7	0.67	0.74	0.84	0.74
30.6	0.62	0.72	0.81	0.86
33.1	0.60	0.71	0.79	0.79

Table 13: $p_{CT}(\nu_i)$ values of the ZnO size-dependent study of Ag/PATP/ZnO ZnO at 488 nm depicted in Figure 57

ZnO nanoparticle diameter [nm]	PATP Mode	Area (below peak) [A. U]	Peak center [cm^{-1}]	Ratio [R] = $b_{(i)}/a_1$	$p_{CT}(\nu_i)$ = [R / (R+1)]
33.1	ν_7a	396849	1078	1.00	-
33.1	ν_9b	597921	1143	1.51	0.60
33.1	ν_3	988509	1388	2.49	0.71
33.1	$\nu_{19}b$	1532350	1438	3.86	0.79
33.1	ν_8b	1463120	1573	3.69	0.79
30.6	ν_7a	231008	1077	1.00	-
30.6	ν_9b	377220	1143	1.63	0.62
30.6	ν_3	597658	1389	2.59	0.72
30.6	$\nu_{19}b$	1003830	1438	4.35	0.81
30.6	ν_8b	1448050	1577	6.27	0.86
27.7	ν_7a	372421	1078	1.00	-
27.7	ν_9b	742159	1144	1.99	0.67
27.7	ν_3	1076250	1391	2.89	0.74
27.7	$\nu_{19}b$	1895400	1437	5.09	0.84
27.7	ν_8b	1051570	1576	2.82	0.74
25.2	ν_7a	276003	1078	1.00	-
25.2	ν_9b	484347	1144	1.75	0.64
25.2	ν_3	756050	1390	2.74	0.73
25.2	$\nu_{19}b$	1320340	1437	4.78	0.83
25.2	ν_8b	1374700	1575	4.98	0.83
23.8	ν_7a	318038	1078	1.00	-
23.8	ν_9b	514311	1143	1.62	0.62
23.8	ν_3	712416	1389	2.24	0.69
23.8	$\nu_{19}b$	1321980	1437	4.16	0.81
23.8	ν_8b	1235660	1574	3.89	0.80
18.2	ν_7a	249908	1076	1.00	-
18.2	ν_9b	417376	1143	1.67	0.63
18.2	ν_3	637344	1388	2.55	0.72
18.2	$\nu_{19}b$	1085210	1438	4.34	0.81
18.2	ν_8b	1077630	1575	4.31	0.81

Table 14: Excitation wavelengths 488 nm; $p_{CT}(vi)$ values in the sample Ag/PATP/ZnO at six different ZnO sizes

ZnO nanoparticle diameter [nm]	PATP Mode	Area (below peak) [A. U]	Peak center [cm^{-1}]	Ratio [R] = $b_{(i)}/a_1$	$p_{CT}(\nu_i)$ = [R / (R+1)]
33.1	$\nu_7 a$	97130	1078	1.00	-
33.1	$\nu_9 b$	95790	1142	0.99	0.50
33.1	ν_3	52069	1389	0.54	0.35
33.1	$\nu_{19} b$	62786	1436	0.65	0.39
33.1	$\nu_8 b$	67750	1578	0.70	0.41
30.6	$\nu_7 a$	66550	1079	1.00	-
30.6	$\nu_9 b$	71895	1141	1.08	0.52
30.6	ν_3	37827	1390	0.57	0.36
30.6	$\nu_{19} b$	58664	1436	0.88	0.47
30.6	$\nu_8 b$	39245	1577	0.59	0.37
27.7	$\nu_7 a$	164558	1077	1.00	-
27.7	$\nu_9 b$	222853	1142	1.35	0.58
27.7	ν_3	116320	1390	0.70	0.41
27.7	$\nu_{19} b$	197451	1436	1.19	0.55
27.7	$\nu_8 b$	100292	1577	0.60	0.38
25.2	$\nu_7 a$	154887	1080	1.00	-
25.2	$\nu_9 b$	145529	1141	0.94	0.48
25.2	ν_3	97074	1389	0.63	0.39
25.2	$\nu_{19} b$	108211	1436	0.70	0.41
25.2	$\nu_8 b$	117627	1577	0.76	0.43
23.8	$\nu_7 a$	388094	1079	1.00	-
23.8	$\nu_9 b$	368988	1143	0.95	0.49
23.8	ν_3	130644	1389	0.34	0.25
23.8	$\nu_{19} b$	239119	1437	0.62	0.38
23.8	$\nu_8 b$	238158	1576	0.61	0.38
18.2	$\nu_7 a$	409533	1077	1.00	-
18.2	$\nu_9 b$	458290	1142	1.12	0.53
18.2	ν_3	204102	1390	0.50	0.33
18.2	$\nu_{19} b$	357591	1436	0.87	0.47
18.2	$\nu_8 b$	216308	1575	0.53	0.35

Table 15: Excitation wavelengths 633 nm; $p_{CT}(vi)$ values in the sample Ag/PATP/ZnO at six different ZnO sizes

ZnO nanoparticle diameter [nm]	PATP Mode	Area (below peak) [A. U]	Peak center [cm^{-1}]	Ratio [R] = $b_{(i)}/a_1$	$p_{CT}(\nu_i)$ = [R / (R+1)]
33.1	ν_7a	352529	1077	1.00	-
33.1	ν_9b	275812	1140	0.78	0.44
33.1	ν_3, $\nu_{19}b$	238873	1409	-	-
33.1	ν_8b	143393	1577	0.41	0.29
30.6	ν_7a	55958	1076	1.00	-
30.6	ν_9b	53744	1143	0.96	0.49
30.6	ν_3	25713	1387	0.46	0.31
30.6	$\nu_{19}b$	27053	1437	0.48	0.33
30.6	ν_8b	24041	1578	0.43	0.30
27.7	ν_7a	51747	1076	1.00	-
27.7	ν_9b	50113	1143	0.97	0.49
27.7	ν_3	24108	1386	0.47	0.32
27.7	$\nu_{19}b$	26219	1437	0.51	0.34
27.7	ν_8b	18904	1579	0.37	0.27
25.2	ν_7a	101618	1077	1.00	-
25.2	ν_9b	75469	1143	0.74	0.43
25.2	ν_3	39061	1383	0.38	0.28
25.2	$\nu_{19}b$	18027	1436	0.18	0.15
25.2	ν_8b	44652	1577	0.44	0.31
23.8	ν_7a	72472	1077	1.00	-
23.8	ν_9b	42984	1142	0.59	0.37
23.8	ν_3	20661	1386	0.29	0.22
23.8	$\nu_{19}b$	13749	1435	0.19	0.16
23.8	ν_8b	26177	1578	0.36	0.27
18.2	ν_7a	155551	1077	1.00	-
18.2	ν_9b	104410	1142	0.67	0.40
18.2	ν_3	64346	1577	0.41	0.29
18.2	$\nu_{19}b$	41215	1385	0.26	0.21
18.2	ν_8b	26101	1440	0.17	0.14

Table 16: Excitation wavelengths 785 nm; $p_{CT}(\nu i)$ values in the sample Ag/PATP/ZnO at six different ZnO sizes

ZnO nanoparticle diameter [nm]	PATP Mode	peak height [A.U]	Peak center [cm^{-1}]	Ratio [R] = $b_{(i)}/a_1$	$p_{CT}(\nu_i)$ = [R / (R+1)]
33.1	ν_7a	0.136	1077	1.00	-
33.1	ν_9b	0.047	1143	0.35	0.26
33.1	ν_3	0.038	1392	0.28	0.22
33.1	$\nu_{19}b$	0.046	1438	0.34	0.25
33.1	ν_8b	0.088	1577	0.64	0.39
30.6	ν_7a	0.042	1079	1.00	-
30.6	ν_9b	0.018	1144	0.44	0.30
30.6	ν_3	0.010	1388	0.23	0.19
30.6	$\nu_{19}b$	0.010	1439	0.24	0.20
30.6	ν_8b	0.029	1579	0.70	0.41
27.7	ν_7a	0.135	1077	1.00	-
27.7	ν_9b	0.108	1145	0.80	0.44
27.7	ν_3	0.061	1394	0.45	0.31
27.7	$\nu_{19}b$	0.090	1440	0.67	0.40
27.7	ν_8b	0.095	1577	0.70	0.41
25.2	ν_7a	0.048	1077	1.00	-
25.2	ν_9b	0.023	1143	0.49	0.33
25.2	ν_3	0.014	1392	0.30	0.23
25.2	$\nu_{19}b$	0.014	1438	0.29	0.22
25.2	ν_8b	0.033	1577	0.70	0.41
23.8	ν_7a	0.111	1079	1.00	-
23.8	ν_9b	0.036	1143	0.33	0.25
23.8	ν_3	0.027	1394	0.24	0.19
23.8	$\nu_{19}b$	0.032	1438	0.28	0.22
23.8	ν_8b	0.064	1577	0.58	0.37
18.2	ν_7a	0.133	1077	1.00	-
18.2	ν_9b	0.054	1145	0.41	0.29
18.2	ν_3	0.040	1394	0.30	0.23
18.2	$\nu_{19}b$	0.051	1440	0.38	0.28
18.2	ν_8b	0.084	1577	0.63	0.39

Table 17: Excitation wavelengths 1064 nm; $p_{CT}(vi)$ values in the sample Ag/PATP/ZnO at six different ZnO sizes

5. Discussion

5.1. Discussion: Wavelength-Dependence Study

Figure 63 shows the wavelength-dependence comparison of $p_{CT}(\nu_9 b)$ values of the samples Ag/PATP, Ag/PATP/ZnO(27.7nm), and (27.7nm)ZnO/PATP/Ag. Both sample structures Ag/PATP/ZnO(27.7nm) and (27.7nm)ZnO/PATP/Ag show significant increase of $p_{CT}(\nu_9 b)$ values at all recorded wavelengths compared to the Ag/PATP sample. In addition, Ag/PATP shows no strong resonance in the observed excitation-wavelength range. The highest value in Ag/PATP was obtained at 496.5 nm, giving 0.42. As shown in Figure 37, the b_2 lines in the Ag/PATP sample are not observed at 1064 nm excitation wavelengths. Hence it is most likely that the $p_{CT}(\nu_9 b)$ values of Ag/PATP decrease from 514.5 nm to 1064 nm until zero. At Ag/PATP/ZnO, a wavelength-dependent resonance of $p_{CT}(\nu_9 b)$ values was observed toward 514.5 nm, giving 0.66. The values decrease at wavelengths below 514.5 nm to 488.0 nm. It is observed that the $p_{CT}(\nu_9 b)$ value at 476.5 nm is almost the same value as at 488.0 nm, giving 0.61. The $p_{CT}(\nu_9 b)$ values decrease toward the low-energy wavelength in the red at 676.4 nm, compared to the value obtained at 514.5 nm. The sample (27.7nm)ZnO/PATP/Ag shows an enhancement pattern very different from that of the Ag/PATP and Ag/PATP/ZnO(27.7nm) samples. The lowest value was obtained at 676.4 nm in the red, giving 0.45. The $p_{CT}(\nu_9 b)$ values increase toward shorter wavelengths at the observed range. The sample (27.7nm)ZnO/PATP/Ag shows indication for resonance toward 476.5 nm and below. Table 18 shows the $p_{CT}(\nu_9 b)$ values for Figure 63.

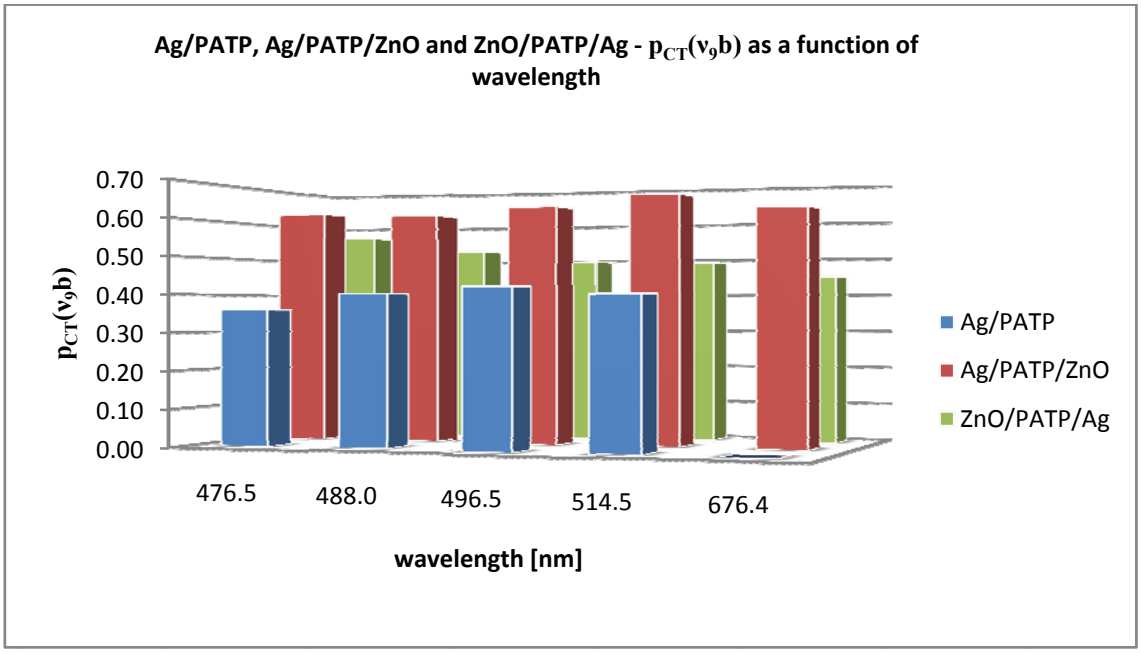

Figure 63: Wavelength-dependence study, degree of $p_{CT}(\nu_9 b)$ as a function of wavelength of the investigated samples Ag/PATP, Ag/PATP/ZnO, and ZnO/PATP/Ag

Wavelength [nm]	Ag/PATP	Ag/PATP/ZnO	ZnO/PATP/Ag
476.5	0.36	0.62	0.56
488.0	0.40	0.61	0.53
496.5	0.42	0.63	0.49
514.5	0.40	0.66	0.49
676.4	-	0.62	0.45

Table 18: $p_{CT}(\nu_9 b)$ values of the samples Ag/PATP, Ag/PATP/ZnO, and ZnO/PATP/Ag at excitation wavelengths from 476.5 nm to 676.4 nm for Figure 63

Figure 64 shows the wavelength-dependence comparison of $p_{CT}(\nu_3)$ values of the samples Ag/PATP, Ag/PATP/ZnO(27.7nm), and (27.7nm)ZnO/PATP/Ag. The comparison is not as accurate as for the $p_{CT}(\nu_9 b)$ values, since baseline corrections and scanning times have a significant influence on the $p_{CT}(\nu_3)$ values (see Figure 57). Therefore, it is not possible to compare the $p_{CT}(\nu_3)$ values with the $p_{CT}(\nu_9 b)$ values directly. The sample structure Ag/PATP/ZnO(27.7nm) shows significant increase of $p_{CT}(\nu_3)$ values at all recorded wavelengths compared to the Ag/PATP sample. The highest value in Ag/PATP was obtained at 488.0 nm, giving 0.46. As shown in Figure 37, the b_2 lines in the Ag/PATP sample are not observed at 1064 nm excitation wavelengths. Hence it is most likely that the $p_{CT}(\nu_3)$ values of Ag/PATP decrease from 488.0 nm to 1064 nm until zero. At Ag/PATP/ZnO(27.7nm), a wavelength-dependent resonance of $p_{CT}(\nu_3)$ values was observed toward 514.5 nm, giving 0.55. The values decrease at wavelengths below 514.5 nm to 488.0 nm. It is observed that the $p_{CT}(\nu_3)$ value at 476.5 nm is lower than the one at 488.0 nm, giving 0.53. The $p_{CT}(\nu_3)$ values decrease toward the red at 676.4 nm, compared to the value obtained at 514.5 nm. The sample (27.7nm)ZnO/PATP/Ag shows an enhancement pattern very different from that of the Ag/PATP and Ag/PATP/ZnO(27.7nm) samples. The lowest value was obtained at 676.4 nm in the red, giving 0.33. The $p_{CT}(\nu_3)$ values increase toward shorter wavelengths at the observed range. The sample (27.7nm)ZnO/PATP/Ag shows an indication of resonance toward 476.5 nm and below. Table 19 shows the $p_{CT}(\nu_3)$ values for Figure 64.

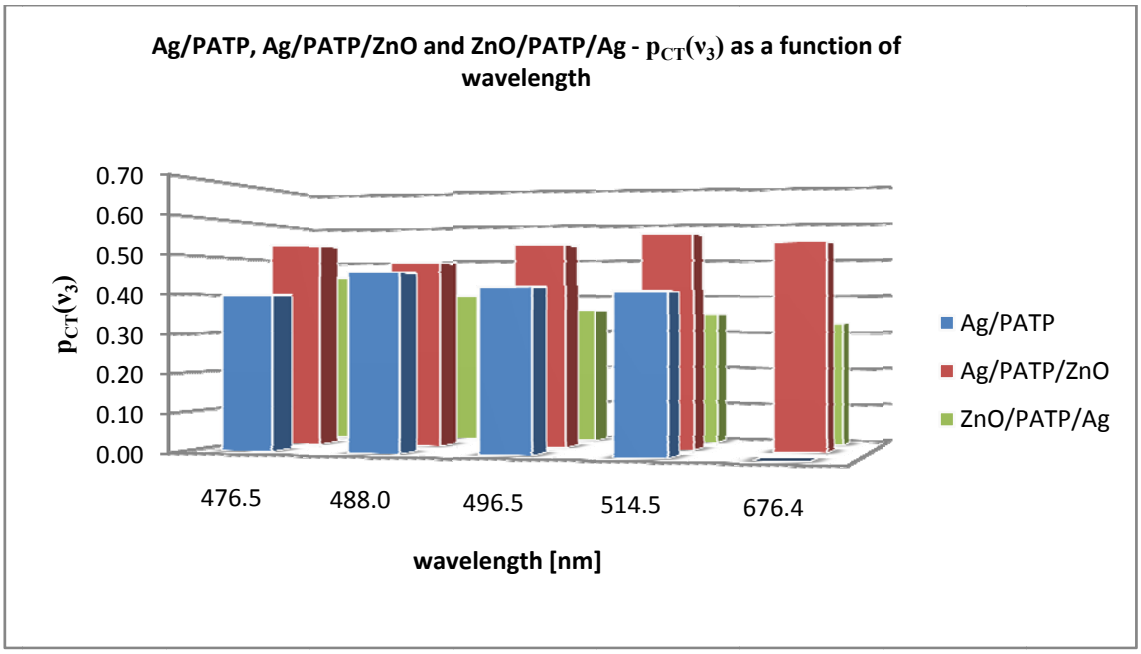

Figure 64: Wavelength-dependence study, degree of $p_{CT}(\nu_3)$ as a function of wavelength of the investigated samples Ag/PATP, Ag/PATP/ZnO, and ZnO/PATP/Ag

Wavelength [nm]	Ag/PATP	Ag/PATP/ZnO	ZnO/PATP/Ag
476.5	0.40	0.53	0.45
488.0	0.46	0.49	0.40
496.5	0.42	0.53	0.36
514.5	0.40	0.55	0.35
676.4	-	0.53	0.33

Table 19: pCT(ν_3) values of the samples Ag/PATP, Ag/PATP/ZnO, and ZnO/PATP/Ag at excitation wavelengths from 476.5 nm to 676.4 nm for Figure 64

Both sample structures Ag/PATP/ZnO(27.7nm) and (27.7nm)ZnO/PATP/Ag show significant increase in $p_{CT}(\nu_9b)$ enhancement compared to the Ag/PATP sample. In addition, the wavelength-dependence resonance in the sample Ag/PATP/ZnO(27.7nm) has shifted from 496.5 nm (488.0 nm for $p_{CT}(\nu_3)$ values) obtained in Ag/PATP to 514.5 nm. The resonance shift is due to adsorption of the PATP molecule on the ZnO nanoparticles, since only ZnO has altered the Ag/PATP sample. Therefore, the PATP molecules behave differently in SERS. This is also responsible for the observed peak shifts. At present, the adsorption process of PATP on ZnO is not well understood. However, the peak positions still indicate the same vibrational modes as observed in the SERS spectrum of Ag/PATP. The $p_{CT}(\nu_9b)$ values in the sample Ag/PATP are obtained through the attribution of CT from Ag to the molecules. The $p_{CT}(\nu_9b)$ enhancements in the sample Ag/PATP/ZnO(27.7nm) and (27.7nm)ZnO/PATP/Ag are obtained through the attribution of CT from Ag to the molecules and an additional charge-transfer process from ZnO. (2). The $p_{CT}(\nu_3)$ values show similar patterns as the obtained $p_{CT}(\nu_9b)$ values. Since baseline correction at these values is not as trustworthy as that at $p_{CT}(\nu_9b)$, the values

and comparisons serve as additional verification of the observed $p_{CT}(\nu_9 b)$ wavelength-dependence resonance in the samples Ag/PATP/ZnO(27.7nm) and (27.7nm)ZnO/PATP/Ag.

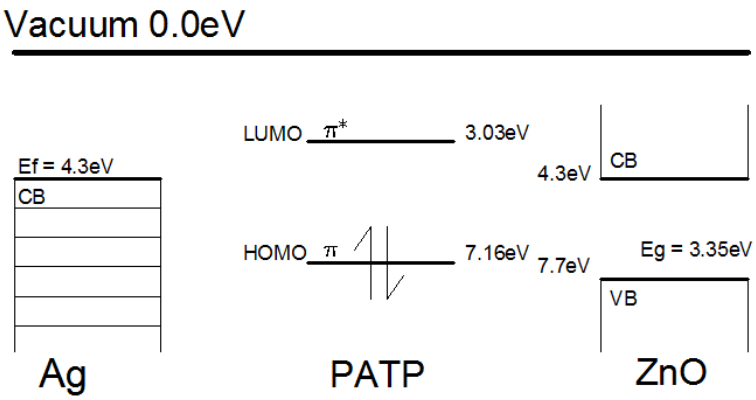

Figure 65: Energy-level diagram of Ag, PATP, and ZnO measured from the vacuum

The energy-level diagram in Figure 65 shows the energy levels for Ag, PATP, and ZnO measured from the vacuum. If a monochromatic excitation beam at 514.5 nm excites electrons from the conduction band of Ag by 2.4 eV to a higher level than the LUMO-level of the PATP molecule, CT from Ag to the π*-orbital of the PATP molecule is most likely. This lowers the Fermi level of Ag. The electrons can relax further from the π*-orbital of the PATP molecule to the conduction band of the ZnO nanoparticles at 4.3eV below the vacuum level, increasing the Fermi level at ZnO. The charge-transfer transition occurs until the Fermi levels at Ag and ZnO are at equilibrium, meaning that the rates of CT in either direction (or all charge-transfer rates) are equal. At this point the SERS signal is stabilized.(2 p. 5) At relaxed states, charge-transfer transitions from the valence band of ZnO at 7.7eV to the conduction band of ZnO, the LUMO of PATP at 3.03eV, or the Fermi level of Ag at 4.3eV are not probable at an excitation wavelength of 514.5 nm (2.4eV), since hardly any SERS signal was observed in ZnO/PATP (see Figure 47). Few scientific publications refer to excitation-wavelength-dependence resonance zones in SERS samples. Therefore, a solid conclusion on the physical and chemical processes is difficult to reach, especially on the samples Ag/PATP/ZnO and ZnO/PATP/Ag. However, the degree of charge transfer ($p_{CT}(\nu_9 b)$) has increased in the samples Ag/PATP/ZnO and ZnO/PATP/Ag compared to the sample Ag/PATP. Therefore, it is most likely that ZnO increases the CT transition rates in the assemblies, since it was experimentally observed in the excitation-wavelength dependence study.

5.2. Discussion: ZnO Size-Dependence Study

Figure 66 shows the size-dependence study of the sample Ag/PATP/ZnO with ZnO nanoparticle sizes from 18.2 nm to 33.1 nm on the z-axis, excitation wavelengths from 488.0 nm to 1064 nm on the x-axis, and $p_{CT}(\nu_9 b)$ values on the y-axis. All $p_{CT}(\nu_9 b)$ values decrease with increasing wavelength. Therefore, at 1064 nm the lowest $p_{CT}(\nu_9 b)$ values are reached. At each wavelength the investigated Ag/PATP/ZnO sample with ZnO nanoparticle size of 27.7 nm gives the highest $p_{CT}(\nu_9 b)$ value, and therefore indicates a size-dependent resonance region. The $p_{CT}(\nu_9 b)$ values decrease toward larger ZnO nanoparticle sizes up to 33.1 nm, and toward smaller ZnO nanoparticle sizes down to 23.8 nm. At the sample 23.8 nm throughout all wavelengths the lowest $p_{CT}(\nu_9 b)$ values are observed. Sample 18.2 nm shows significantly higher $p_{CT}(\nu_9 b)$ values compared to the adjacent sample with 23.8 nm-sized ZnO nanoparticles. Therefore, it is possible to find further resonances at smaller ZnO particle sizes than 18.2 nm. Table 20 shows the $p_{CT}(\nu_9 b)$ values of the ZnO size-dependence study that are depicted in Figure 66.

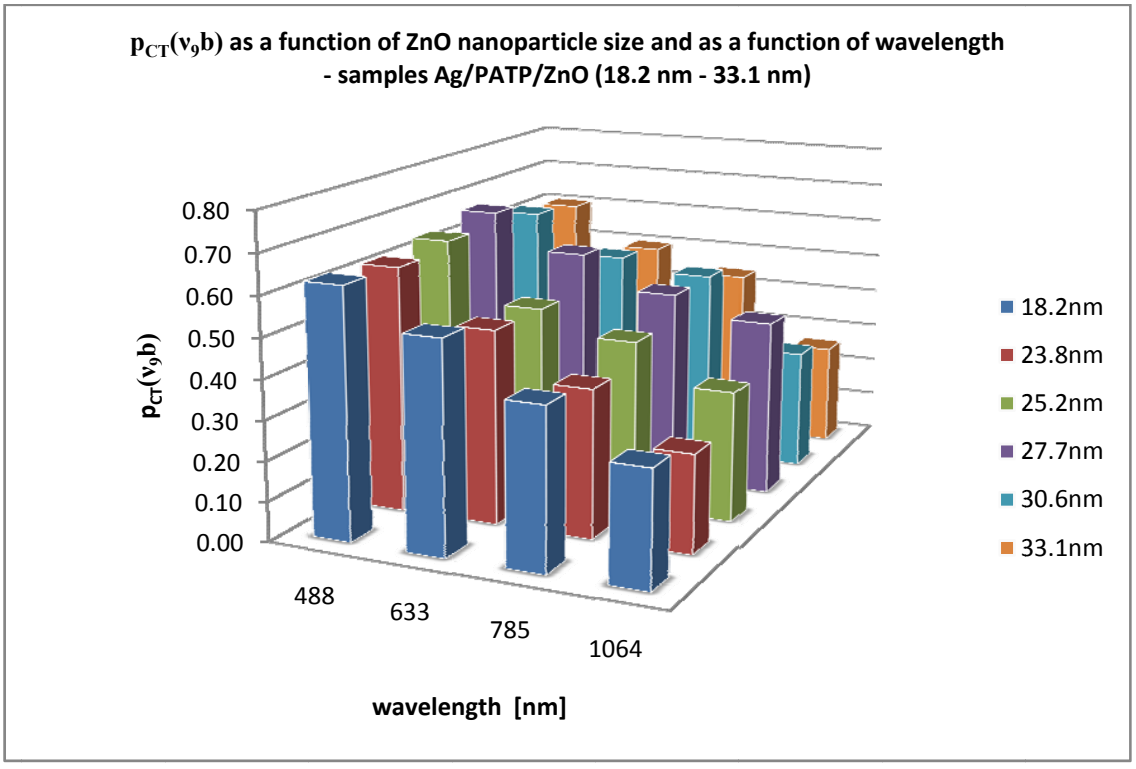

Figure 66: Size-dependence study of $p_{CT}(\nu_9 b)$ values as a function of excitation wavelength and ZnO nanoparticle size

Wavelength [nm]	18.2 nm	23.8 nm	25.2 nm	27.7 nm	30.6 nm	33.1 nm
488	0.63	0.62	0.64	0.67	0.62	0.60
633	0.53	0.49	0.48	0.58	0.52	0.50
785	0.40	0.37	0.43	0.49	0.49	0.44
1064	0.29	0.25	0.33	0.44	0.30	0.26

Table 20: $p_{CT}(\nu_i)$ values of the ZnO size-dependence study of the samples Ag/PATP/ZnO(18.2 to 33.1 nm) at 488.0 nm to 1064 nm excitation wavelength as depicted in Figure 66

Figure 67 shows the size-dependence study of the sample Ag/PATP/ZnO with ZnO nanoparticle sizes from 18.2 nm to 33.1 nm on the z-axis, excitation wavelengths from 488 nm to 1064 nm on the x-axis, and $p_{CT}(\nu_3)$ values on the y-axis. The general pattern of these size-dependent $p_{CT}(\nu_3)$ values resembles that of the size-dependent $p_{CT}(\nu_9 b)$ values shown in Figure 66. All $p_{CT}(\nu_3)$ values decrease with increasing wavelength. Comparison of the $p_{CT}(\nu_3)$ values obtained at 488 nm and at 633 nm show a step change in $p_{CT}(\nu_3)$ values not observed in $p_{CT}(\nu_9 b)$ values in Figure 66. At the sample 27.7 nm, a $p_{CT}(\nu_3)$ value decrease of 55% is observed. The other sizes show similar strong $p_{CT}(\nu_3)$ value decreases between 46% and 53%. At 1064 nm the lowest $p_{CT}(\nu_3)$ values are reached. At each wavelength the investigated Ag/PATP/ZnO sample with the ZnO nanoparticle size of 27.7 nm gives the highest $p_{CT}(\nu_3)$ value, and therefore indicates a size-dependent resonance region. The $p_{CT}(\nu_3)$ values decrease toward larger ZnO nanoparticle sizes up to 33.1 nm, and toward smaller ZnO nanoparticle sizes down to 23.8 nm. At 785 nm, no value for $p_{CT}(\nu_3)$ can be calculated precisely, since neither the ν_3 line nor its adjacent $\nu_{19} b$ line is developed (see multiple-run study in Figure 57). In the sample 23.8 nm, it can be observed that the $p_{CT}(\nu_9 b)$ values stay almost constant from 633 nm with $p_{CT}(\nu_3)$= 0.25 to 1064 nm $p_{CT}(\nu_3)$ = 0.19. Sample 23.8 nm gives throughout all wavelengths the lowest $p_{CT}(\nu_3)$ values compared to the other sizes. Sample 18.2 nm shows significantly higher $p_{CT}(\nu_3)$ values compared to the adjacent sample with 23.8-nm-sized ZnO nanoparticles. Therefore, it is possible to find further resonances at smaller particle sizes than 18.2 nm.

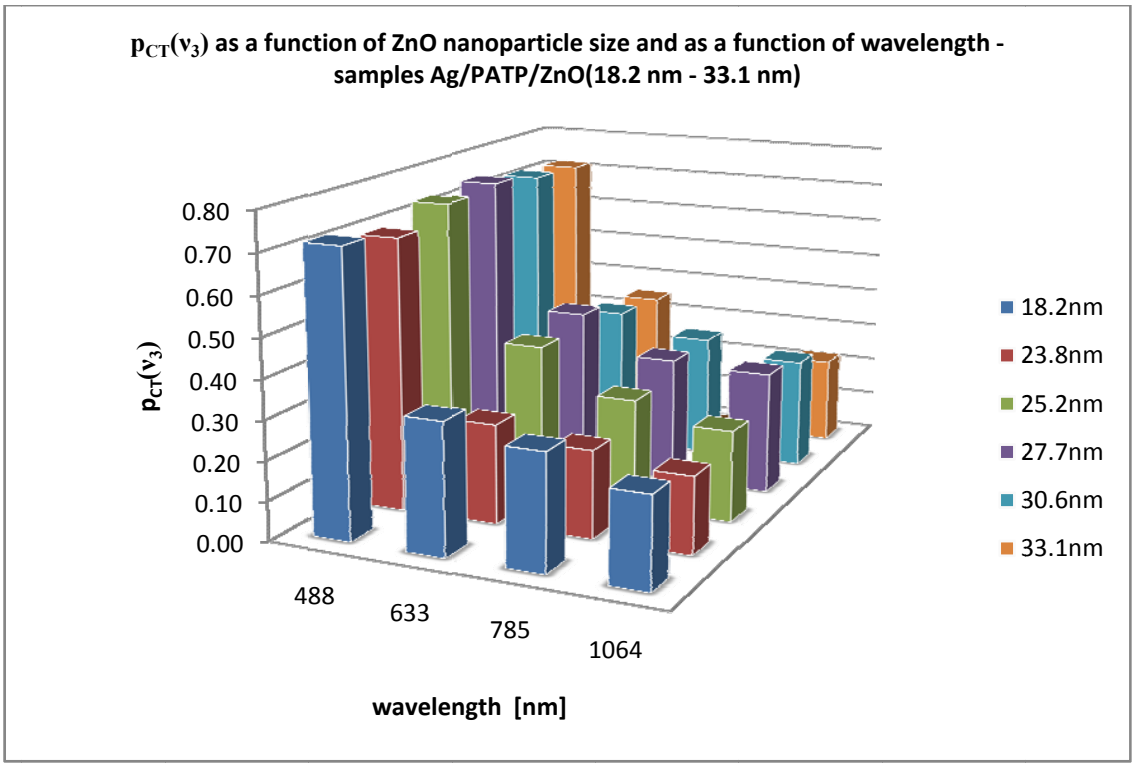

Figure 67: Size-dependence study of $p_{CT}(\nu_3)$ values as a function of excitation wavelength and ZnO nanoparticle size

Wavelength [nm]	18.2 nm	23.8 nm	25.2 nm	27.7 nm	30.6 nm	33.1 nm
488	0.72	0.69	0.73	0.74	0.72	0.71
633	0.33	0.25	0.39	0.41	0.36	0.35
785	0.29	0.22	0.28	0.32	0.31	0.00
1064	0.23	0.19	0.23	0.31	0.28	0.22

Table 21: $p_{CT}(\nu_3)$ values of the ZnO size-dependence study of the samples Ag/PATP/ZnO(18.2 nm to 33.1 nm) at 488 nm to 1064 nm excitation wavelength as depicted in Figure 67

In the samples Ag/PATP/ZnO(18.2 nm to 33.1 nm) with varying ZnO nanoparticle size, a size-dependent resonance of $p_{CT}(\nu_9b)$ and $p_{CT}(\nu_3)$ values was found at 27.7 nm.

The size-dependence study matched the observations of Prof. Zhao, who observed a ZnO size-dependent resonance at 27.7 nm in the sample 4-MPy adsorbed on ZnO nanoparticles (see Figure 43). The resonance was observed at all applied excitation wavelengths at 488 nm, 633 nm, 785 nm, and 1064 nm. The decrease of $p_{CT}(\nu_9b)$ and $p_{CT}(\nu_3)$ values with increasing excitation wavelengths indicates that the charge-transfer contribution decreases toward 1064 nm excitation wavelength. The multiple-run study has shown that the $p_{CT}(\nu_9b)$ values are more reliable than the $p_{CT}(\nu_3)$ values (see Figure 57), since the applied SERS scanning time at low laser power has a strong influence on the $p_{CT}(\nu_3)$ values but not on the $p_{CT}(\nu_9b)$ values. Therefore, the step change of $p_{CT}(\nu_3)$ values observed from 488.0 nm to 633 nm (see Figure 67) could be explained by the scanning time of the laser (shorter wavelengths

are more energy intense), or it could indicate that the charge-transfer peak in an intensity-versus-excitation wavelength plot in the SERS spectrum for the line ν_3 has a more narrow width than does that for the line ν_9b. More detailed investigations are needed to make a detailed conclusion. Compared with the sample structure Ag/PATP, which gives no enhancement of b_2 lines at 1064 nm and therefore a $p_{CT}(\nu_9 b)$ and $p_{CT}(\nu_3)$ value of zero (see Figure 37)(28), the investigated sample Ag/PATP/ZnO(18.2 nm to 33.1 nm) still shows enhancements of b_2 lines at 1064 nm and therefore positive $p_{CT}(\nu_9 b)$ and $p_{CT}(\nu_3)$ values. As a result, it can be concluded that ZnO nanoparticles are responsible for the observed increase in $p_{CT}(\nu_9 b)$ and $p_{CT}(\nu_3)$ values at 1064 nm. A recent scientific publication shows that in the thin-film-sandwich structure Ag/PATP/ZnO(nanorods) no b_2 line enhancement was observed at 1064 nm (see Figure 48). Unlike in the samples investigated in this work, a thin film structure with ZnO nanorods with diameters varying from 0.5 to 2µm was used. It has been argued that the electronegative-charged thiol group is responsible for hindering electronic transfers from Ag through PATP to ZnO at 1064 nm. However, this bachelor work shows that it is possible to obtain a SERS signal at 1064 nm in the sample Ag/PATP/ZnO(18.2 nm to 33.1 nm). Therefore, the smaller ZnO particles and the sample preparation procedure could have increased the charge-transfer contribution. Since the nanoparticle sizes used in the size-dependence study are well above the excitation Bohr radius, no quantum confinement occurs. Thus, it is most likely that the ZnO nanoparticle sizes have an influence on how the PATP molecules are adsorbed on their surfaces and that this influences the observed SERS signal and calculated $p_{CT}(\nu_i)$ values.

6. Conclusion and Recommendation

6.1. Conclusion

The results presented in this work lead to a better understanding of how ZnO nanoparticles influence SERS spectra. ZnO nanoparticles were added to the system Ag/PATP to form the additional sample structures Ag/PATP/ZnO and ZnO/PATP/Ag. The wavelength-dependence study compared $p_{CT}(\nu_9 b)$ values of the sample structures Ag/PATP, Ag/PATP/ZnO, and ZnO/PATP/Ag with one another. The size-dependence study compared $p_{CT}(\nu_9 b)$ values of the sample structure Ag/PATP/ZnO(18.2 nm to 33.1 nm) with one another.

Based on the experiments presented in Chapter 4, the following results can be reached:

- The obtained spectra of the samples Ag/PATP/ZnO(27.7nm) and (27.7nm)ZnO/PATP/Ag show in general more sophisticated SERS patterns than those of the sample Ag/PATP;
- the $p_{CT}(\nu_i)$ value comparison at different wavelengths of the samples Ag/PATP/ZnO, ZnO/PATP/Ag, and Ag/PATP shows that ZnO nanoparticles increase the $p_{CT}(\nu_9 b)$ values;
- the highest $p_{CT}(\nu_9 b)$ value in each sample was obtained for:
  - Ag/PATP at 496.5 nm with 0.42 (resonance)
  - Ag/PATP/ZnO at 514.5 nm with 0.66 (resonance)
  - ZnO/PATP/Ag at 476.5 nm with 0.56 (resonance toward 476.5 nm);
- ZnO nanoparticles increase charge-transfer contribution in SERS. In the sample structure Ag/PATP/ZnO(18.2 nm to 33.1 nm) at 1064 nm excitation wavelength, charge-transfer was still observed. This was not observed in publications in Ag/PATP or in Ag/PATP/ZnO (0.2 µm – 2 µm);
- the size-dependence study of ZnO nanoparticles in the system Ag/PATP/ZnO proves a resonance at the 27.7-nm sample at four different excitation wavelengths;
- the Ag/PATP/ZnO system with 18.2 nm probably indicates a further resonance with ZnO nanoparticle sizes below 18.2 nm;
- in the size-dependence study, the decrease of charge-transfer contribution at excitation wavelengths from 488.0 nm to 1064 nm was observed.

The conducted studies prove that ZnO nanoparticles enhance the SERS signal of PATP, that excitation-wavelength dependent resonance in the Ag/PATP/ZnO and ZnO/PATP/Ag structures are different from resonance in the Ag/PATP structure, and that the observed signals in the Ag/PATP/ZnO system are ZnO nanoparticle size dependent.

6.2. Recommendation

It is recommended to conduct the wavelength-dependence study in the samples Ag/PATP, Ag/PATP/ZnO, and ZnO/PATP/ZnO at wavelengths below 476.5 nm since the studies presented in this work indicate a wavelength-dependent resonance in the sample ZnO/PATP/Ag below 476.5 nm. Since the sample structures Ag/PATP/ZnO and ZnO/PATP/Ag lead to more sophisticated SERS spectra showing the vibrational modes of PATP compared to the sample structure Ag/PATP, other sandwich-structure studies with a variety of organic molecules are suggested, in order to find out whether ZnO affects their SERS spectra positively as well. In addition, it is recommended to investigate ZnO nanoparticle sizes below 18.2 nm, including ZnO quantum dots where quantum confinement occurs. Since quantum confinement changes the properties of semiconductor materials, it is expected that ZnO quantum dots could lead to further size-dependent resonance with even higher $p_{CT}(\nu_9 b)$ value enhancements and more sophisticated SERS spectra.

Bibliography

1. *A Unified Approach to Surface-Enhanced Raman Spectroscopy.* **Lombardi, John R. and Birke, Ronald L.** s.l. : Phys. Chem. C., 2008, Vol. 112. 5606-5617.

2. *Nanoparticle Metal-Semiconductor Charge Transfer in ZnO/PATP/Ag Assemblies by Surface-Enhanced Raman Spectroscopy.* **Zhihua Sun, Chunxu Wang, Jingxiu Yang, Bing Zhao, John R. Lombardi.** Changchun : Phys. Chem. C, 2008, Vol. 112 No. 15.

3. *ZnO nanoparticle size-dependent excitation of surface Raman signal from adsorbed molecules: Observation of a charge-transfer resonance.* **Zhihua Sun and Bing Zhao, John R. Lombardi.** Changchun : Appl. Phys. Lett., 2007, Vol. 91. 221106.

4. **Chennupati Jagadish, Stephen J. Pearton.** *Zinc Oxide Bulk, Thin Films and Nanostructures.* s.l. : Elsevier Ltd., 2006. ISBN: 0080447228.

5. *Molecular Symmetry.* **Willok, David J.** Chichester : John Wiley & Sons, Ltd., 2009. ISBN: 978-0-470-85347-4.

6. **Smith, Ewen and Dent, Geoffrey.** *Modern Raman Spectroscopy - A Practical Approach.* Hoboken : John Wiley & Sons, Inc., 2005. ISBN: 0-471-49668-5.

7. *Microsoft Encarta.* s.l. : Microsoft, 2009. Laser.

8. **Zettilli, Nouredine.** *Quantum Mechanics Concepts and Applications.* Second Edition. Chichester : John Wiley & Sons Ltd., 2009. ISBN: 978-0-470-02678-6.

9. **Frank l. Pedrotti, S.J. Leno S. Pedroti.** *Intruduction to Optics.* Second Edition. Upper Saddle River : Prentice Hall, Inc., 1987. ISBN: 0-13-501545-6.

10. *Magnetism From Fundamentals to Nanoscale Dynamics.* **J. Stöhr, H.C. Siegmann.** Berlin : Springer-Verlag Berlin Heidelberg New York, 2006. ISBN-10 3-540-30282-4.

11. *Microsoft Encarta.* s.l. : Microsoft, 2009. Light.

12. **Saslow, Wayne M.** *Electricity, Magnetism, and Light.* s.l. : Elsevier, 2002. ISBN: 978-0-12-61 9455.

13. **Stover, John C.** *Optical Scattering: Measurement and Analysis.* New York : McGraw-Hill, 1990. ISBN: 0-07-061814-3.

14. **Silvast, William T.** *Laser Fundamentals.* Second Edition. Cambridge : Cambridge University Press, 2004. ISBN: 0-521-83345-0.

15. **Denk, Michael K.** http://131.104.156.23/Lectures/CHEM_207/CHEM_207_Intro.htm. *University of Guelph.* [Online] 2005. [Cited: 05 01, 2009.] Chem 2070.

16. *Colorado State University, National Small Scale Chemistry Center.* [Online] [Cited: 04 08, 2009.] Fundamentals of Spectroscopy. http://www.smallscalechemistry.colostate.edu/.

17. **Schmid, E. D., et al., [ed.].** *Proceedings of the Sixth International Conference o Raman Spectroscopy.* s.l. : Heyden & Son Ltd., 1978. ISBN: 0-85501-201-3.

18. **Lombardi, Roland L. Birke and John R.** Surface Enhanced Raman Scattering. [book auth.] Robert James Gale. *Spectrochemistry Theory and Practise.* New York : Plenum Press, New York, 1988.

19. **McCreery, Richard L.** *Raman Spectroscopy for Chemical Analysis.* Hoboken : John Wiley & Sons, Inc., 2000. ISBN: 0-471-25287-5.

20. *Surface-enhanced Raman scattering for identification of organic pigments and dyes in works of art and cultural heritage.* **Chen, Kui, Leona, Marco and Vo-Domh, Tuan.** s.l. : Sensor Review, 2007, Vol. 27 Number 2. 109-120.

21. *A Unified View of Surface-Enhanced Raman Scattering.* **Lombardi, John R. and Birke, Ronald L.** New York : Acc. of chem. research, 2009. DOI: 10.1021/ar800249y.

22. *Raman microscopy in archaelogical science.* **Smith, Gregory D. and Clark, Robin J.H.** s.l. : J. Archeol. Sc., 2004, Vol. 31. 1137-1160.

23. **Lewis, Ian R. and Edwards, Howell G. M.** *Handbook of Raman Spectroscopy.* New York - Basel : Marcel Dekker, Inc., 2001. ISBN: 0-8247-0557-2.

24. *Charge Transfer Resonance Raman Process in Surface-Enhanced Raman Scattering from p-Aminothiophenol Adsorbed on Silver: Herzberg-Teller Contribution.* **Masatoshi Osawa, Naoki Matsuda, Katsumasa Yoshii, and Isamu Uchida.** s.l. : Phys. Chem. C., 1994, Vol. 98. 12702-12707.

25. *Adsorption and Surface-Enhanced Raman of Dyes on Silver and Gold Sols.* **Lee, P. C. and Meisel.** s.l. : Phys. Chem., 1982, Vol. 86. 3391-3395.

26. **L. Q. Jing, Z. L. Xu, J. Shang, X. J Sun, W. M. Cai, and H. C. Guo.** 356, s.l. : Mater. Sci Eng, 2002, Vol. A 332.

27. *See EPPS document No. E-APPLAB-91-041748 for XRD pattern of the ZnO NPs calcined at different temperatures.*

28. *Determination of the Degree of Charge-Transfer Contributions to Surface-Enhanced Raman Spectroscopy.* **Cat Chenal, Ronald L. Birke, and John R. Lombardi.** s.l. : Chem. Phys. C., 2008. DOI: 10.1002/cphc.200800221.

Figures

Tables

Abbreviations

Symbol	Description	Unit
h	Plank's constant, h = 4.14x10^-15 eVs	eVs
c	Speed of light, c = 3.0x10^8 m/s	m/s
ν	Frequency of light	1/s
λ	Wavelength	nm
λ_L	Wavelength Laser	nm
λ_{Raman}	Wavelength Raman	nm
ω	Wavenumber	cm^{-1}
$\Delta\omega_{Raman}$	Raman shift from reference wavenumber	cm^{-1}
p	Momentum of a photon	Kg*m/s
W	Work function	eV
E	Energy	eV
E_f	Fermi level (chemical potential)	eV
A.U.	Arbitrary Unit	
CB	Conduction band	
VB	Valance band	
HOMO	Highest occupied molecular orbital (filled with electrons)	
LUMO	Lowest unoccupied molecular orbital (empty orbital)	
IR	Infrared	
NIR	Near Infrared	
RR	Resonance Raman	
SERS	Surface-Enhanced Raman Spectroscopy	
SNR	Signal to noise ratio	
CCD	Charged-coupled device	
PMT	Photomultiplier tube	
PATP	p-aminothiophenol (C_6H_7NS)	
4-MPY	4-mercaptopyridine (C_5H_5NS)	
TEM	Transmission Electron Microscopy	